Thermal Stratification and Turbulent Wind Loading on Floating Wind Turbines

Rieska Mawarni Putri

Thesis submitted in fulfilment of the requirements for the degree of PHILOSOPHIAE DOCTOR (PhD)

Faculty of Science and Technology
Department of Mechanical and Structural Engineering and Materials Science

2023

University of Stavanger
N-4036 Stavanger
Norway

ISBN: 978-82-8439-180-9
ISSN: 1890-1387
PhD Thesis UiS No. 713

Year: 2023
Title: Thermal Stratification and Turbulent Wind Loading on Floating Wind Turbines
Author: Rieska Mawarni Putri

Preface

This thesis is submitted in partial fulfillment of the requirements for the degree of Doctor of Philosophy (PhD) at the University of Stavanger, Norway. This study has been carried out at the Faculty of Science and Technology, Department of Mechanical and Structural Engineering and Material Science, and was funded by the Norwegian Ministry of Education and Research.

Acknowledgements

First and foremost, I would like to thank Allah swt. for giving me the strength from the beginning and throughout the completion of this dissertation. This PhD journey would not be possible without the help of the Almighty.

Secondly, to all my supervisors: Prof. Charlotte Obhrai, Prof. Jasna Jakobsen, and Dr Etienne Cheynet, I thank you for the valuable knowledge, guidance, discussions, and support until the completion of this dissertation. Prof. Charlotte Obhrai, whom I thank for giving me the opportunity to pursue this degree and for having trust in me. Prof. Jasna Jakobsen, whom I thank for her incredible insights and last-minute responses, no matter how tight the deadlines were. Dr Etienne Cheynet, whom I thank for his constant moral encouragement, technical support, and invaluable practical knowledge.

I would also like to thank Dr Lene Eliassen, who helped me to set up the turbulent wind input for the numerical simulation during my early PhD period. Also, to Prof. Kurt Hansen for kindly providing the Vindeby wind records. To Prof. Joachim Reuder and Dr Stephan Kral for the discussion on the wind-wave interaction, as well as to Prof. Muk Chen Ong for his support during my PhD study.

To my parents and my little brother. Your endless prayers and support have helped me endure this journey. Thank you very much. I dedicate this dissertation to my mother, father, and brother.

My PhD colleagues, especially Sen Qu and Trond-Ola Hågbo. Thank you for your constant moral support and the sweet memories we made during our PhD journeys.

Last but not least, I would like to thank my colleagues at Subsea 7. I was able to join 7Sail, which has made my days windy yet less gloomy as I struggled to complete this dissertation. The Wednesday Regattas and the

Saturday long Regatta were great fun!

My restless PhD journey has taught me valuable aspects of technical writing, presentation, and time management that I will not get anywhere else. Doing a PhD is like sailing at sea. You can never predict exactly what the weather will be like, regardless of what the forecast suggests. The journey is worth every struggle and fear I have encountered. It is truly my privilege to experience a PhD journey.

اَلحَمدُلِلّٰهِ رَبِّ العَالَمِين

Rieska Mawarni Putri
Stavanger, June 2023

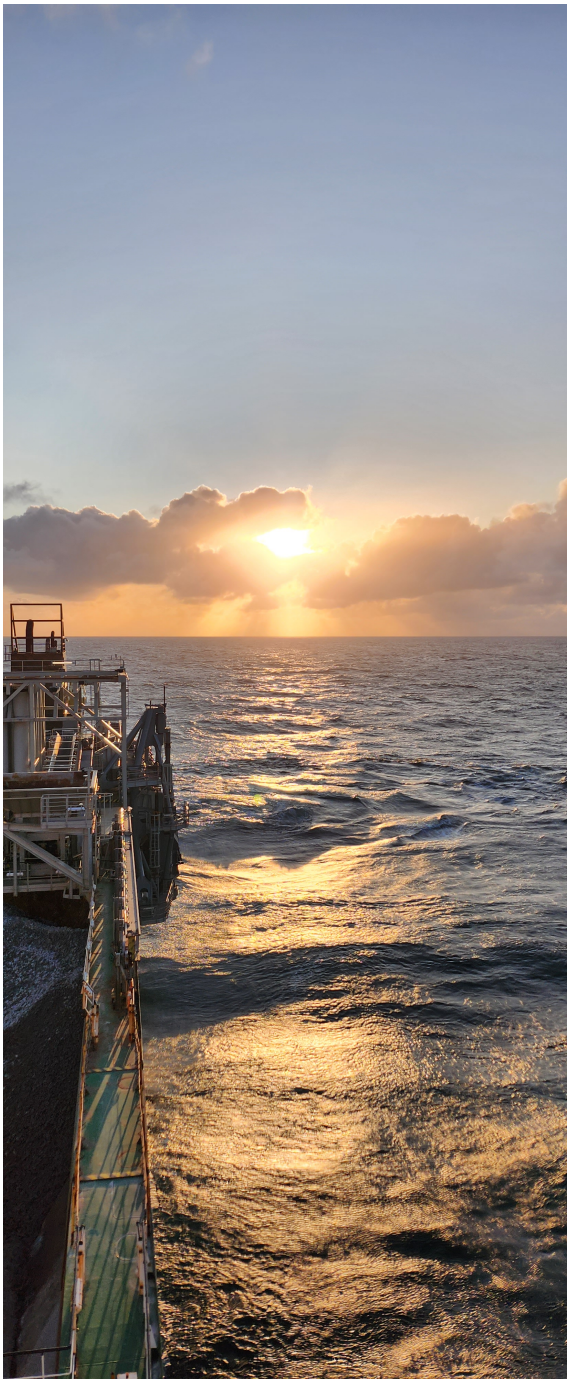

Offshore, the northern Norwegian Sea with $\overline{u}_{10} = 22\,\text{kn}$ and $H_S = 2.9\,\text{m}$. Sunrise on 10$^{\text{th}}$ September 2023, photo by Rieska Mawarni Putri.

Abstract

Offshore wind is a promising clean energy alternative to fossil fuels. The wind resource at sea is considerably stronger than on land, and the offshore wind turbines (OWTs) tend to be larger. Currently, more than 160 commercial offshore wind farms (OWFs) are in operation worldwide, of which 2% are floating wind farms (FWFs). Bottom-fixed OWTs are mainly installed close to shore and in shallow water, where operation, maintenance and substructure costs are lower than for floating solutions. However, some countries have deep water close to the coast, which makes the development of floating offshore wind turbines (FOWTs) an attractive alternative (e.g. in Japan, Norway, and the west coast of the USA). The floating offshore wind industry is expected to continue to reduce costs, making it competitive with bottom-fixed developments in the near future.

The atmospheric inflow to wind turbines includes mesoscale and microscale processes. For a FOWT, the floater introduces additional degrees of freedom compared to a bottom-fixed foundation, thus extending the dynamic response of FOWTs to a wider frequency interval. The natural frequencies of the floaters are in the range of the microturbulence frequencies influenced by the thermal stratification of the atmosphere (atmospheric stability). The design standards for wind turbines do not usually take atmospheric stability into account. However, atmospheric stability should be considered in the design of state-of-the-art FOWTs to improve estimates of the wind loads, structural response and power production.

This thesis investigates the impact of atmospheric stability on the FOWT response and fatigue loads through numerical simulations. The two study cases include the 5 MW OC3-Hywind spar wind turbine (WT) and the 5 MW OC4 DeepCwind semi-submersible WT. The wind inflow is generated using different turbulence spectral models: Davenport-Kaimal, Uniform Shear, Pointed-Blunt, and Højstrup Spectral Model with Daven-

port co-coherence. The variable atmospheric stability is simulated using the Pointed-Blunt Model and the Højstrup Spectral Model with Davenport co-coherence. The effects of single-point and two-point spectra on the two WTs are assessed separately and then jointly. A single wave loading scenario with a fixed significant wave height and peak period is adopted.

In both study cases, the simulated fatigue damage associated with the tower top twisting and the side-side bending moment is found to increase in an unstable atmosphere compared to a near-neutral atmosphere, as is the yaw and sway of the floaters. In a near-neutral atmosphere, the difference in the spatial turbulence characteristics (co-coherence) in the two spectral models (Uniform Shear Model and the Davenport-Kaimal Model) is also seen to affect the response of the OC3-Hywind and the OC4 DeepCwind. For example, the tower side-side bending moment is found to be greater by up to 27% in a less coherent turbulent flow. This emphasises the need to base the design of FOWT on lateral co-coherence models derived from offshore field measurements at separations relevant to FOWTs, which are currently scarce.

The simulated response of the OC3-Hywind to atmospheric stability using the Pointed-Blunt Model is compared to the observed response from the full-scale measurements of a 6 MW spar WT at Hywind Scotland. The simulated floater pitch and yaw are found to be consistent with the measured responses. This highlights the importance of incorporating atmospheric stability into the design of FOWTs.

In addition, analyses of wind measurements at a coastal site, Vindeby, are carried out with a focus on turbulence characteristics. These characteristics are then compared with measurements from an offshore platform, FINO1, from which the Pointed-Blunt model is derived. The spectral turbulence characteristics observed at Vindeby ($\leq$ 45 m above sea level (asl)) show a reasonable agreement with the characteristics observed at FINO1 ($\leq$ 81.5 m asl).

This thesis recommends the inclusion of atmospheric stability in the design of state-of-the-art FOWTs, to obtain representative wind loading. Future wind measurements to include heights above 100 m asl, and measurements to obtain information on lateral co-coherence are encouraged to provide relevant design data. Lateral co-coherence, which is representative of offshore sites with relevant separation distances for modern FOWTs, has been partially addressed in the COTUR (COherence of TURbulence

with lidars) project. However, lateral co-coherence in the MABL remains a topic for further study.

Keywords: Floating wind turbine, Atmospheric stability, Turbulence model, Spectral turbulence characteristics, Co-coherence, Floater response, Fatigue load

List of abbreviations and symbols

List of abbreviations

2D	two-dimensional
ABL	Atmospheric Boundary Layer
asl	above sea level
BEM	Blade Element Momentum
bsl	below sea level
CAPEX	Capital Expenditure
COTUR	COherence of TURbulence with lidars
DEL	Damage Equivalent Load
DOF	Degree of Freedom
EU	European Union
FEA	Finite Element Analysis
FOWT	Floating Offshore Wind Turbine
FWF	Floating Wind Farm
GW	Gigawatt
IEC	International Electrotechnical Committee
LCOE	Levelised Cost of Electricity
MABL	Marine Atmospheric Boundary Layer
MTG	Mann Turbulence Generator
MW	Megawatt

NREL	National Renewable Energy Laboratory
OC3	Offshore Code Comparison Collaboration
OC4	Offshore Code Comparison Collaboration Continuation
OPEX	Operating Expense
OWF	Offshore Wind Farm
OWT	Offshore Wind Turbine
SMW	South Mast West
SWL	Sea Water Level
SIMA	Simulation Workbench for Marine Application
SIMO	Simulation of Marine Operations
TI	Turbulence Intensity
TW h	Terrawatt-hour
WT	Wind Turbine

List of symbols

a	Induction factor (in BEM) [-]
a_1^i,a_2^i,a_3	Coefficients derived from measurements in the Pointed-Blunt Model, $i = u, v, w$ [-]
a'	Tangential induction factor (in BEM) [-]
b_1^i,b_2^i	Coefficients derived from measurements in the Pointed-Blunt Model, $i = u, v, w$ [-]
B	Number of blades [-]
c	Exponential decay coefficient [-]
c	Local airfoil length (in BEM) [m]
c_b^a	Exponential decay coefficient for velocity component $a = u, v, w$ and separation $b = y$ (lateral), $b = z$ (vertical) [-]
c_1,c_1^i,c_2^i	Coefficients derived from measurements in the Pointed-Blunt Model, $i = u, v, w$ [-]
C_d	Airfoil drag coefficient [-]
C_l	Airfoil lift coefficient [-]
$\mathrm{d}r$	Radial increment of the blade [m]
$\mathrm{d}F_t$	Local tangential force on an aerofoil [$\mathrm{N\,m^{-1}}$]
$\mathrm{d}Q$	Local torque on an aerofoil [N]
$\mathrm{d}T$	Local thrust force on an aerofoil [$\mathrm{N\,m^{-1}}$]
D_{rot}	Rotor diameter [m]
f	Frequency [Hz]
F_t	Tangential force [N]
g	Acceleration of gravity [$\mathrm{m\,s^{-2}}$]
h	Depth of boundary layer [m]
H_S	Significant wave height [m]
k	Wave number [$\mathrm{m^{-1}}$]

L	Obukhov length [m]
L_i	Integral lengthscale used in the Kaimal Spectra (IEC, 2005), where $i = u$, v, or w [m]
L_M	Eddy lengthscale used in the uniform shear model [m]
n	Reduced frequency (non-dimensional frequency) [-]
n_i	Reduced frequency (non-dimensional frequency) [-]
r	Radial position of the local airfoil [m]
S_u	Velocity spectrum of along-wind component [$\mathrm{m^2\,s^{-1}}$]
S_v	Velocity spectrum of lateral wind component [$\mathrm{m^2\,s^{-1}}$]
S_w	Velocity spectrum of vertical wind component [$\mathrm{m^2\,s^{-1}}$]
T	Thrust force [N]
T_p	Wave peak period [s]
u	Along-wind component [$\mathrm{m\,s^{-1}}$]
$\overline{u}$	Mean wind speed [$\mathrm{m\,s^{-1}}$]
$\overline{u}_{hub}$	Mean wind speed at hub height [$\mathrm{m\,s^{-1}}$]
$\overline{u}_{z1z2}$	Average wind speed at heights z_1 and z_2 [$\mathrm{m\,s^{-1}}$]
u'	Fluctuating along-wind component [$\mathrm{m\,s^{-1}}$]
u_*	Friction velocity [$\mathrm{m\,s^{-1}}$]
v	Lateral wind component [$\mathrm{m\,s^{-1}}$]
v'	Fluctuating lateral wind component [$\mathrm{m\,s^{-1}}$]
V	Incoming wind speed reduced by an induction factor [$\mathrm{m\,s^{-1}}$]
V_{rel}	Relative wind speed [$\mathrm{m\,s^{-1}}$]
w	Vertical wind component [$\mathrm{m\,s^{-1}}$]
w'	Fluctuating vertical wind component [$\mathrm{m\,s^{-1}}$]
z	Height (above a surface or mean sea level) [m]
z_0	Surface roughness (or roughness length) [m]
z_{hub}	Hub height above ground or sea surface [m]

z_i	Inversion height [m]

List of greek symbols

α	Empirical constant for logarithmic wind profile [-]
α	Angle of attack (in BEM) [deg]
α_c	Charnock constant ≈ 0.015 [-]
$\alpha\varepsilon^{2/3}$	Energy dissipation of turbulence used in the uniform shear model [$m^{4/3}\ s^{-2}$]
Δs	Separation distance, either in lateral or vertical direction [m]
Δy	Lateral separation distance [m]
Δz	Vertical separation distance [m]
ε	Dissipation rate of turbulent kinetic energy [$m^2\,s^{-3}$]
$\gamma_{Davenport}$	Davenport co-coherence for vertical separation distance [-]
$\gamma_{Davenport2}$	Davenport co-coherence for lateral and vertical separation distances [-]
γ_{IEC}	IEC-Davenport co-coherence [-]
γ_u	Co-coherence of the along-wind component [-]
γ_v	Co-coherence of the lateral component [-]
γ_w	Co-coherence of the vertical component [-]
Γ	Eddy lifetime/isotropic parameter in the uniform shear model [-]
κ	von Kármán constant ≈ 0.4 [-]
ω	Rotational speed [rpm]
ϕ	Local inflow angle (in BEM) [deg]
ϕ_ε	Normalised turbulent kinetic energy dissipation rate [-]
ϕ_m	Non-dimensional wind shear [-]

Ψ_M	Logarithmic wind speed profile correction to include atmospheric stability [-]
ρ	Air density [$\mathrm{kg\,m^{-3}}$]
σ_i	Standard deviation of velocity component $i = u$, v, or w [$\mathrm{m\,s^{-1}}$]
θ	Potential temperature [K]
$\overline{\theta}$	Mean potential temperature [K]
ζ	Non-dimensional stability parameter [-]

List of papers

This thesis is a compilation thesis which includes five manuscripts:

1. Putri, R. M., Obhrai, C., & Knight, J. M. (2019) *Offshore wind turbine loads and motions in unstable atmospheric conditions*, Journal of Physics: Conference Series **1356(1)** 012016. doi:10.1088/1742-6596/1356/1/012016

2. Putri, R. M., Obhrai, C., Jakobsen, J. B., & Ong, M. C., (2020) *Numerical analysis of the effect of offshore turbulent wind inflow on the response of a spar wind turbine*, Energies **13(10)** 2506. doi:10.3390/en13102506

3. Putri, R. M., Obhrai, C., & Jakobsen, J. B. (2020) *Response sensitivity of a semisubmersible floating offshore wind turbine to different wind spectral models*, Journal of Physics: Conference Series **1618(2)** 022012. doi:10.1088/1742-6596/1618/2/022012

4. Putri, R. M., Cheynet, E., Obhrai, C., & Jakobsen, J. B., (2022) *Turbulence in a coastal environment: the case of Vindeby*, Wind Energy Science **7(4)** 1693–1710. doi:10.5194/wes-7-1693-2022

5. Putri, R. M. & Obhrai, C. (2022) *Wind-induced response of an offshore wind turbine under non-neutral conditions: A comparison with Hywind Scotland*, Journal of Physics: Conference Series **2362** 012031. doi:10.1088/1742-6596/2362/1/012031

Contents

Part I

Chapter 1

Introduction

1.1 Background

In 2015, 196 countries signed the Paris Agreement to achieve net-zero emissions by 2050 (United Nations, 2015). Most countries have come up with a strategy to replace fossil fuels with low-carbon energy sources, including wind. According to IRENA (2021), wind energy production was the second highest amongst the renewable energy sources during the year 2020, with the average annual growth of wind energy between 2018 and 2020 being around 10% (IEA, 2020). In 2021, the annual growth rate increased by 17% compared to 2020, which corresponds to a power generation of 1870 TW h, the largest compared to other power production methods (IEA, 2022). Nonetheless, this figure is insufficient to meet the net-zero carbon emission target, as the power generation is expected to be 7900 TW h by 2030 (IEA, 2022).

From 2001 to 2021, the cumulative installed wind energy capacity, both onshore and offshore, increased from 24 GW to 837 GW (Jaganmohan, 2022). As of 2021, only about 7% of the installed capacity came from offshore wind farms (OWFs) (IEA, 2022). Despite this small share, offshore wind is a promising source of clean energy as it has a higher capacity factor than onshore wind (Fleming, 2019). In addition, offshore wind has the advantage of having less visual and noise impact than onshore wind (Brunel, 2021).

According to European Comission (2022), the European Union (EU) aims to achieve new installed offshore wind capacity of about 60 GW by 2030 and 300 GW by 2050. In 2021, the newly commissioned OWFs

in the EU reached only 1 GW (Europe, 2022). The Norwegian government is aiming for an installed offshore wind capacity of 30 GW by 2040 (regjeringen.no, 2022). This ambitious target implies that an annual installed capacity of at least 1.8 GW is required from 2023 to 2040.

Presently, offshore wind has a greater levelised cost of electricity (LCOE) than onshore wind due to the higher capital expenditure (CAPEX), operating expenditure (OPEX), and maintenance costs (EIA, 2022). A significant improvement in the design of offshore wind turbines (OWTs) is needed to reduce the LCOE of offshore wind. In particular, the improvement requires a reduction in the uncertainties of the environmental loading, especially the dynamic wind loads, a requirement that has motivated the present study. Improved modelling of the dynamic wind loads relies on a better knowledge of the atmospheric flow physics for different thermal stratifications and, in general, in various terrains (Veers et al., 2019).

This thesis investigates the response sensitivity of floating offshore wind turbines (FOWTs) to wind thermal stratification. The dynamic behaviour of the FOWTs is studied numerically, using an established aero-hydro-servo-elastic analysis tool. Wind conditions representative of different atmospheric stability are simulated based on the state-of-the-art turbulence spectra. This thesis also includes a comparison of the numerically simulated sensitivity trends of FOWTs with those observed in the field. The topic has been of great interest to both academia and industry in the context of the aforementioned offshore wind development plans.

1.2 Motivation and research questions

Figure 1.1 shows the growth in wind turbine size from 1991 to 2016. During this period, the rotor diameter of OWTs has increased nearly fivefold. As the offshore wind sector matures in technology, it is expected that even larger wind turbines will be deployed to extract more wind energy further offshore. Water depth is the main aspect that determines the choice of foundation for an OWT. For example, the Burbo Bank Extension project with 8 MW turbines was installed on fixed monopile foundations in water depths between 5 m to 35 m (DONG Energy, 2013).

In September 2020, GE Renewable Energy announced that 190 of their largest wind turbine (Haliade-X) with a rated capacity of 13 MW and a rotor diameter of 220 m will be deployed at the Dogger Bank Wind

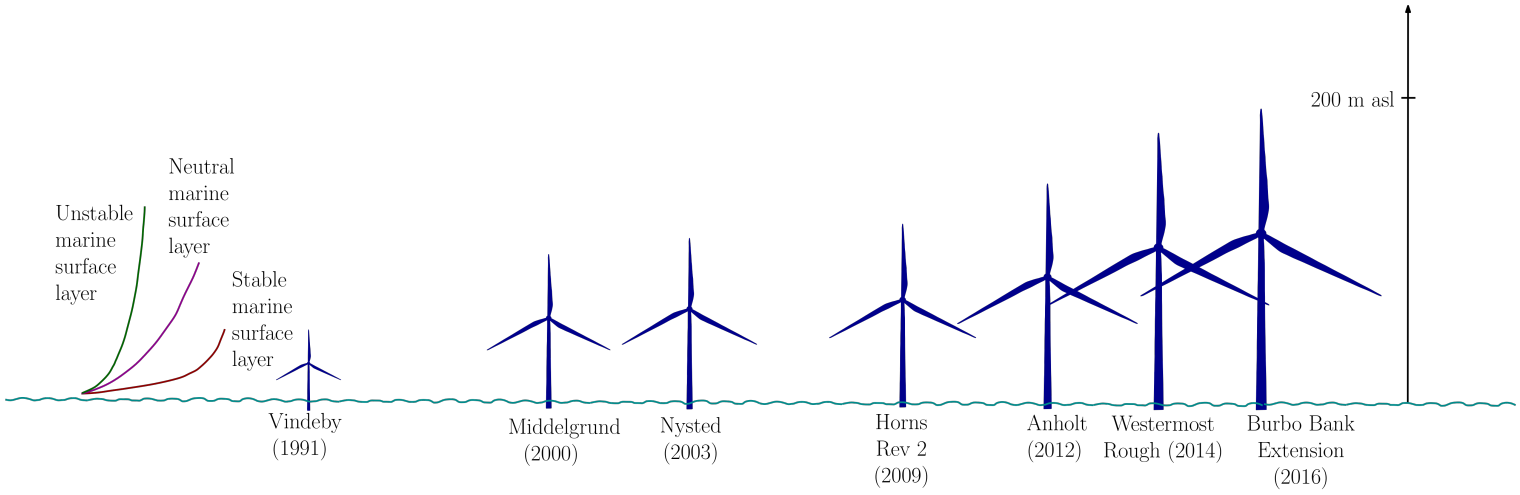

Figure 1.1: Evolution of wind turbine size from 1991 to 2016, compared to the marine surface layer height for different atmospheric stabilities. The marine surface layer height increases from stable to neutral to unstable atmospheres. The 8 MW Burbo Bank Extension OWT extends to above the marine surface layer. Future OWTs will be even larger.

Farm (Phase A, B, and C) (GE Renewable Energy, 2020). The Haliade-X turbine reaches a height of up to 260 m above the surface, higher than the Burbo Bank Extension wind turbine (WT) as illustrated in fig. 1.1. At Dogger Bank Phase A, B, and C, the Haliade-X turbine will be paired with a monopile foundation due to the relatively shallow water of ≈30 m in the area (GE Renewable Energy, 2020). Yet, the Dogger Bank Offshore Development Zone stretches about 8660 km^2 with water depths ranging from 18 m to 63 m, allowing the Haliade-X turbine to also be installed on a floater.

While the floater motions and structural load responses of a large rotor floating offshore wind turbine (FOWT) due to wave loading have been investigated in the literature (e.g. by Paulsen et al. (2013); Li and Bachynski (2021)), the effect of wind loading has been addressed in a limited number of studies, namely by Bachynski and Eliassen (2019); Doubrawa et al. (2019); Nybø et al. (2020). Moreover, the met-ocean conditions for FOWT design are not yet fully understood and have been highlighted as one of the grand challenges in wind energy by Veers et al. (2019). Refined modelling of met-ocean conditions for FOWT design is therefore essential for the future development of state-of-the-art FOWTs.

At offshore sites, the structure of the turbulence varies with the thermal stratification of the atmosphere, more commonly known as atmospheric stability (Businger et al., 1971). Atmospheric stability also affects the surface layer height as illustrated in fig. 1.1.

Since the 1970s, surface layer turbulence has been conveniently parameterised by a set of basic variables, such as the height above ground, the surface roughness length, the friction velocity and the Obukhov length (Kaimal et al., 1972). Hereinafter, this parameterisation will be referred to as surface-layer scaling.

Standards and codes that are developed for WT designs rely largely on surface-layer scaling, either directly or indirectly. However, in the marine atmospheric boundary layer (MABL), the marine surface layer is often shallower than the height of a WT. Hence, the turbulence models used to compute wind loading on WTs are expected to become less reliable with increasing WT size, as sketched in fig. 1.1. In the International Electrotechnical Committee (IEC) 61400-1 standard (IEC, 2005), the information on wind inflow condition is characterised using the hub height of the WT as a reference. This standard recommends two different turbulence models,

where the thermal stratification of the atmosphere is generally disregarded for structural design (IEC, 2005). This is unlikely to be the case in the MABL for the range of wind speeds encountered by WTs.

This thesis aims to develop a framework to assess the dynamic response of a FOWT under variable atmospheric stability conditions. The main questions addressed are: (i) how can the thermal stratification of the atmosphere be accounted for in the design of a FOWT, and (ii) how are the structural loads and motions of a FOWT affected by non-neutral wind conditions? The following specific sub-questions are derived from the main research questions:

- Sub-question 1: Why do the two turbulence models from IEC (2005) lead to different FOWT responses?
- Sub-question 2: How does the thermal stratification of the atmosphere affect the motions of a FOWT?
- Sub-question 3: How do the simulated responses of FOWT under non-neutral stability conditions compare with relevant full-scale response measurements?
- Sub-question 4: How do the wind turbulence characteristics at a coastal site (Vindeby Wind Farm, 3 km from the coast at 4 m water depth) compare with the characteristics measured far offshore (FINO1 Platform, 40 km from the coast at 30 m water depth)?

The commonly used approach to estimate wind loading on slender structures (typically bridges and towers) is following the Davenport Wind Loading Chain (Davenport, 1961a), which consists of five main aspects: wind climate, influence of terrains, aerodynamic effects, dynamic effects (including WT control system and waves), as well as design criteria (Isyumov, 2012). The aforementioned sub-questions can be related to the chain as shown in fig. 1.2. In this thesis, the Davenport Wind Loading Chain is applied to the design of a FOWT.

1.3 Thesis structure

This thesis compiles five papers published between 2019 and 2022. The first part covers the literature review, the methodology, the research sum-

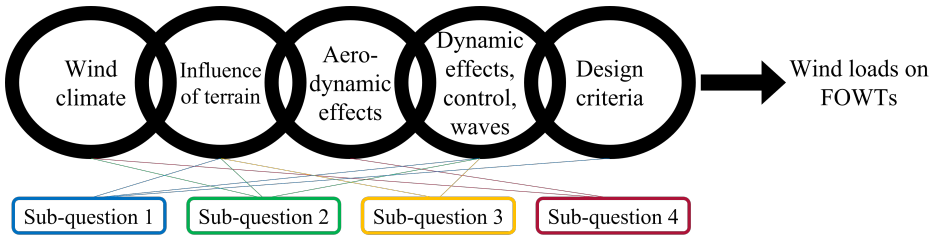

Figure 1.2: Davenport wind loading chain for a FOWT.

mary and recommendations for future work. Chapter 2 summarises the fundamental knowledge related to the marine surface layer and the aero-hydro-servo-elastic tool used to numerically simulate the floater motions and the structural loads of FOWTs. Chapter 3 summarises the findings in relation to the main research questions and the sub-questions from the papers. Lastly, chapter 4 concludes the thesis and recommends some future studies/work.

The second part of this thesis contains the five published peer-reviewed papers which address the research questions outlined in section 1.2, where fig. 1.3 outlines the relationship between the papers and the research questions.

Sub-question 1 discusses the comparison of structural loads and floater motions of a FOWT from numerical simulations using the Davenport-Kaimal Model as well as the Uniform Shear Model in IEC (2005). Sub-question 1 is addressed in Paper 2 (Putri et al., 2020a) and Paper 3 (Putri et al., 2020b).

Sub-question 2 discusses the structural loads and floater motions of a FOWT by considering non-neutral atmospheres in the numerical simulations, using the turbulence model in Cheynet et al. (2018). Sub-question 2 is addressed in Paper 2 (Putri et al., 2020a), Paper 3 (Putri et al., 2020b) and partly in Paper 1 (Putri et al., 2019).

Sub-question 3 discusses the comparison of the floater motions of a numerically simulated spar FOWT under the influence of variable atmospheric thermal stratification with the full-scale response measurements. Sub-question 3 is addressed in Paper 5 (Putri and Obhrai, 2022).

Finally, Sub-question 4 addresses the wind turbulence characteristics at a coastal site, near the Vindeby offshore wind farm. The turbulence characteristics are compared with those at a location farther offshore, the

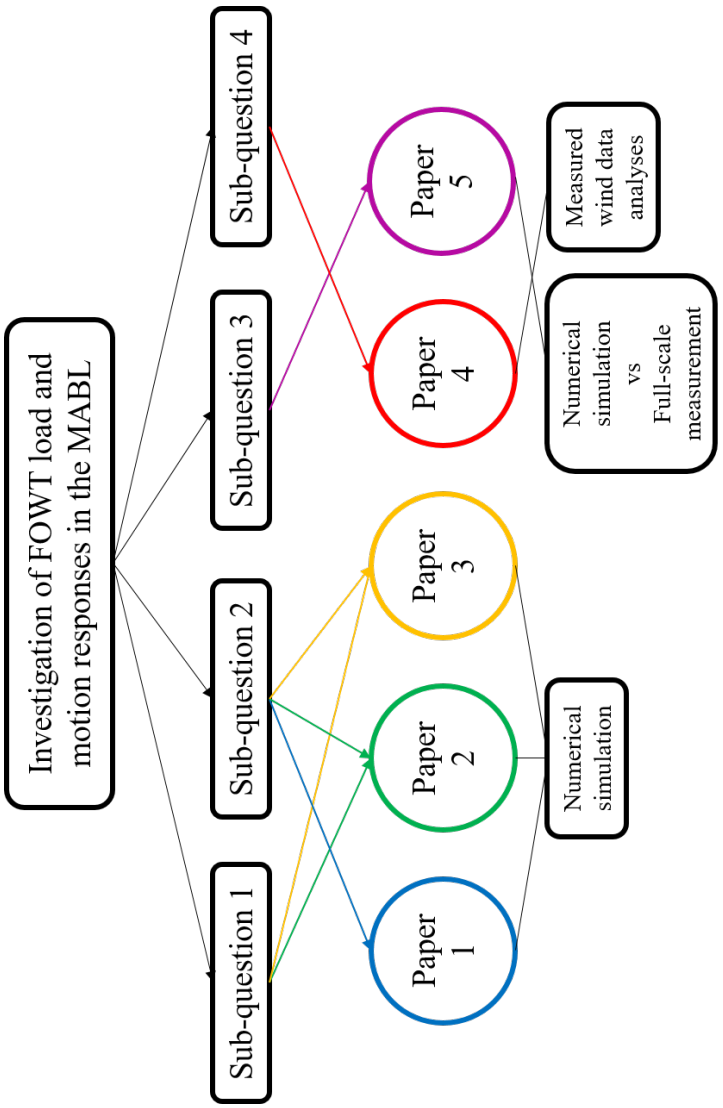

Figure 1.3: Diagram showing the link between the papers and the research questions.

FINO1 Platform. Sub-question 4 is answered in Paper 4 (Putri et al., 2022).

1.4 Study limitations

The present thesis focuses on the effect of different MABL thermal stratifications on the structural loads and floater motions of FOWTs for free wind conditions only. The influence of atmospheric stability on the development of the WT wake is not covered.

The turbulence models considered in this thesis are based on surface-layer scaling, which may not be applicable to the design of large FOWTs as visualised in fig. 1.1. The work presented in this thesis stays within the framework of Gaussian, horizontally homogeneous, and stationary micro-turbulence. Non-stationary turbulence may represent a substantial fraction of offshore wind conditions (Cheynet et al., 2018; Putri et al., 2022).

The selection of coherence values to capture the spatial correlation of turbulent winds in this thesis is limited by the availability of relevant observations, especially for non-neutral atmospheric stability. The present thesis is also limited by the lack of wind measurements at heights above the surface layer and the detailed full-scale data from FOWTs, which makes it difficult to validate the results of the presented numerical models.

As wave loading is not the main focus of this study, the numerical simulations were performed using only the irregular linear wave theory. For simplicity, fully-developed sea states without swell were used in the simulations. The use of non-linear wave theory for aeroelastic simulations would better capture the wave spectra at frequencies lower than 0.04 Hz (Xu et al., 2019), which coincide with the natural frequencies of the floater. Furthermore, the influence of the wind-wave interactions is not addressed in the numerical simulations but is discussed briefly in Paper 4 (Putri et al., 2022).

Lastly, the FOWT structural loads and floater motions were calculated using a simplified model of a mooring system in the time-domain numerical simulations. Equivalent cross-sectional properties of the multi-segment mooring lines are used in the numerical simulation model. Additionally, the hydrodynamic damping (viscous effect) of the mooring lines due to their movement in the water and the interaction of the mooring lines with the seabed soil are not modelled. The linear mooring model is valid for small floater displacements and thus limits the magnitude of the simulated

motions (Jonkman et al., 2009; Hall et al., 2014; Robertson et al., 2014).

Chapter 2

Background and methods

This chapter gives an overview of the MABL and its characteristics, different turbulent wind models for both neutral and non-neutral atmospheric stabilities, the aero-hydro-servo-elastic tool for numerical simulations of the FOWTs, as well as the spar and the semi-submersible wind turbine models used in the study.

2.1 The marine atmospheric boundary layer

The atmospheric boundary layer (ABL) is the lowest part of the Earth's atmosphere that is directly influenced by the surface. The surface refers to either the ground or the sea surface. The ABL extends from the Earth's surface up to its depth, h, which typically ranges from $\approx 1-3$ km on land (Stull, 1988; Garratt, 1994; Kaimal and Finnigan, 1994). Above the sea surface, h is in the order of 10^2m to 10^3m metres (Zeng et al., 2004; Ho et al., 2015).

Natural three-dimensional wind can be described in a Cartesian coordinate system where the mean wind direction follows the x-axis. With one axis aligned with the mean wind direction, the along-wind component (u), lateral wind component (v), and vertical wind component (w) correspond consecutively to the x, y, and z axes of the right-hand rule coordinate system. Each wind component can be decomposed into a mean value (with

an overbar sign) and a fluctuating value (with a prime sign), such that

$$u = \overline{u} + u' \tag{2.1}$$

$$v = v' \tag{2.2}$$

$$w = w' \tag{2.3}$$

where $\overline{u}$ is the mean wind speed. The fluctuating components are assumed to be stationary, ergodic, Gaussian random processes, and horizontally homogeneous in space. The ratio of the along-wind component fluctuation to its mean value can be measured by the so-called turbulence intensity,

$$TI = \frac{\sigma_u}{\overline{u}} \tag{2.4}$$

where σ_u is the standard deviation of the along-wind component.

Based on eqs. (2.1) to (2.3), a reference velocity u_* associated with the wind stress acting on the surface known as the friction velocity, could be computed as (Stull, 1988),

$$u_* = \sqrt[4]{\overline{u'w'}^2 + \overline{v'w'}^2}. \tag{2.5}$$

Friction velocity is an important parameter for the surface layer and is strongly influenced by the presence of the ground. The surface layer stretches from the surface roughness z_0 up to about 10% of the ABL depth (Tennekes et al., 1972; Holton, 1973). The roughness length z_0 depends on the topography (Wieringa, 1992). The surface layer in the MABL is usually shallower than above the ground due to the significantly smaller value of z_0.

The roughness length in the MABL depends on the wave conditions, which in turn are dependent on the wind speed. Based on the data from fully-developed seas with no swell, Charnock (1955) described the roughness length over a sea surface in an empirical form,

$$z_0 = \frac{\alpha_c u_*^2}{g} \tag{2.6}$$

where g is the acceleration of gravity and α_c is the Charnock constant ≈ 0.015 which varies with sea condition (Wu, 1980). For developing sea

states or mixed sea with swell, Smedman et al. (2003) proposed a refined formulation to calculate the roughness length.

2.2 Non-dimensional parameters in the surface layer

The Obukhov length L has the dimension of a distance and quantifies the ratio of the mechanically generated turbulence to buoyancy-generated turbulence. The atmosphere is stable when negative buoyancy inhibits turbulence ($L > 0$), while it is unstable ($L < 0$) when positive buoyancy amplifies turbulence. In the near-neutral atmospheres ($|L| > 10000$ m), the mechanically generated turbulence dominates over buoyancy.

Atmospheric stability on land varies diurnally, depending on the solar irradiance (Stull, 1988). The heat capacity of the ground is considerably lower than that of the ocean, thus the atmosphere above land is often stable at night and unstable during the day. Sea temperature varies seasonally due to its higher heat capacity, so atmospheric stability above the ocean varies seasonally. In particular, the atmosphere is often stable in summer, when the sea surface temperature is lower than the air temperature. It is unstable in winter, when the sea temperature is often higher than the air temperature.

The atmospheric stability is described using the non-dimensional stability parameter ζ defined as

$$\zeta = \frac{z}{L} = -\frac{(g/\overline{\theta})(\overline{w'\theta'})_0}{u_*^3/\kappa z} \tag{2.7}$$

where z is the height above the surface, L is the Obukhov length (Monin and Obukhov, 1954), $\overline{\theta}$ is the mean virtual potential temperature, $\overline{w'\theta'}_0$ is the vertical flux of virtual potential temperature, and $\kappa \approx 0.4$ is the von Kármán constant (Högström, 1988).

Monin and Obukhov (1954) proposed that the characteristics of turbulence in the surface layer can be approximated to follow a universal behaviour when normalised by scaling parameters. One of the two main scaling parameters is the friction velocity u_* (eq. (2.5)).

If normalised by u_*, the mean wind shear and the dissipation of turbulent kinetic energy in the surface layer follow the non-dimensional functions

below, respectively (Kaimal and Finnigan, 1994),

$$\phi_m(\zeta) = (\kappa z/u_*)(\partial \overline{u}/\partial z) \tag{2.8}$$

$$\phi_\varepsilon(\zeta) = \kappa z \varepsilon / u_*^3 \tag{2.9}$$

where ε is the rate of turbulent kinetic energy dissipation. For near-neutral atmospheres,

$$\varepsilon = u_*^2 \left(\frac{u_*}{\kappa z} \right). \tag{2.10}$$

Equations (2.8) and (2.9) have previously been fitted to measurement data from different sites for -2$\leq \zeta \leq$1 by, among others, Kaimal et al. (1972); Högström (1988); Businger (1988), leading to some discrepancies in the resulting empirical formulations. These discrepancies were attributed to flow distortion by the wind sensors for $\zeta < 0$ (Högström, 1988). In the following, the empirical formulae from the Kansas measurement are used as a reference (Kaimal and Finnigan, 1994),

$$\phi_m \approx \begin{cases} (1+16|\zeta|)^{-1/4}, & -2 \leq \zeta < 0 \\ 1+5\zeta, & 0 \leq \zeta \leq 1 \end{cases} \tag{2.11}$$

$$\phi_\varepsilon \approx \begin{cases} \left(1+0.5|\zeta|^{2/3}\right)^{3/2}, & -2 \leq \zeta < 0 \\ 1+5\zeta, & 0 \leq \zeta \leq 1. \end{cases} \tag{2.12}$$

By integrating eq. (2.8) over the height z, the logarithmic mean wind speed profile $\overline{u}(z)$ for the surface layer can be derived. For a near-neutral atmosphere, this wind speed profile is

$$\overline{u}(z) = \frac{u_*}{\kappa} \ln \left(\frac{z}{z_0} \right). \tag{2.13}$$

Under stable conditions, the vertical temperature gradient is positive, such that the mean wind speed profile becomes,

$$\overline{u}(z) = \frac{u_*}{\kappa} \left[\ln \left(\frac{z}{z_0} \right) + \Psi_M \left(\frac{z}{L} \right) \right] \tag{2.14}$$

$$\Psi_M \left(\frac{z}{L} \right) = \alpha \frac{z}{L} \tag{2.15}$$

where α is an empirical constant and taken as $\alpha \approx 5$ (Businger et al., 1971). For unstable conditions, the vertical temperature gradient is negative, hence the mean wind speed profile becomes

$$\overline{u}(z) = \frac{u_*}{\kappa}\left[\ln\left(\frac{z}{z_0}\right) - \Psi_M\left(\frac{z}{L}\right)\right]. \tag{2.16}$$

Following Högström (1988), Ψ_M for an unstable atmosphere could be expressed as

$$\Psi_M\left(\frac{z}{L}\right) = 2\ln\left(\frac{1+x_M^{-1}}{2}\right) - \ln\left(\frac{1+x_M^{-2}}{2}\right) + 2\tan^{-1}\left(x_M^{-1}\right) - \frac{\pi}{2} \tag{2.17}$$

and x_M is defined as

$$x_M = \left(1 - 19.3\frac{z}{L}\right)^{1/4}. \tag{2.18}$$

2.3 Turbulence models for near-neutral atmosphere

The knowledge of the mean wind speed and the integral turbulence characteristics alone is insufficient for the design of OWTs. Information on the spectral structure of the turbulence is also needed. For near-neutral atmospheres, spectral turbulence models such as the Davenport-Kaimal Model (Thresher et al., 1981; IEC, 2005), the Uniform Shear Model (Mann, 1994), and the Pointed-Blunt Model (Cheynet, 2018) are used in this thesis. Henceforward, a turbulence model is referred to as a combination of one-point and two-point spectra. This includes the real part of the normalised two-point spectra, the so-called co-coherence. The term "coherence model" will then refer to a co-coherence model, throughout this thesis.

2.3.1 The Davenport-Kaimal Spectral Model

The Davenport-Kaimal Model (Thresher et al., 1981) combines the one-point Kaimal Spectral Model (Kaimal and Finnigan, 1994) and the Davenport Coherence Model (Davenport, 1961b). The Kaimal Spectral Model was derived based on 15 hours of data in a flat, homogeneous onshore site (Kaimal et al., 1972) at heights up to 32 m (Haugen et al., 1971). The

Kaimal Spectral Model uses surface-layer scaling to normalise the velocity spectra, i.e. the friction velocity as the scaling velocity and z as the scaling length.

Following Kaimal and Finnigan (1994), the non-dimensional one-point wind velocity spectra S_u, S_v, and S_w are respectively,

$$\frac{fS_u(f)}{u_*^2} = \frac{102n}{(1+33n)^{5/3}} \tag{2.19}$$

$$\frac{fS_v(f)}{u_*^2} = \frac{17n}{(1+9.5n)^{5/3}} \tag{2.20}$$

$$\frac{fS_w(f)}{u_*^2} = \frac{2.1n}{\left(1+5.3n^{5/3}\right)}. \tag{2.21}$$

where n is a reduced frequency

$$n = \frac{fz}{\overline{u}}. \tag{2.22}$$

The averaging period for $\overline{u}$ within the stationary assumption is typically 10 min according to IEC (2005). However, the temporal range could vary up to 60 min depending on the atmospheric stability and whether it is offshore or onshore (Dobson, 1981; Kaimal and Finnigan, 1994).

Annex B of IEC (2005) provides the spectra shown in eqs. (2.19) to (2.21) which uses a different formulation to Kaimal and Finnigan (1994), such that

$$\frac{fS_i(f)}{\sigma_i^2} = \frac{\dfrac{4fL_i}{\overline{u}_{hub}}}{\left(1+\dfrac{6fL_i}{\overline{u}_{hub}}\right)^{5/3}} \tag{2.23}$$

where $i = u, v, w$, S_i is the velocity spectrum for each component i, σ_i is the standard deviation of the velocity component i, L_i is the integral length scale for the velocity component i (m), and $\overline{u}_{hub}$ is the mean wind speed at hub height. As shown in eq. (2.23), the same spectral function is formulated for the three velocity components, where σ_i and L_i are respectively the standard deviation and the turbulence length scale of the velocity component $i = u, v, w$. The length-scale parameter L_i is given so $L_u > L_v > L_w$.

Davenport (1961b) defined that the normalised two-point auto-power spectral densities at two different heights for the along-wind component u can be approximated by an exponential decay,

$$\gamma_{Davenport}(\Delta z, f) = \exp\left(-c\frac{f\Delta z}{\overline{u}_{z1z2}}\right) \tag{2.24}$$

where $\Delta z = |z_2 - z_1|$ is the vertical separation distance, and $c \approx 7.7$ is the exponential decay coefficient (Davenport, 1961b). $\overline{u}_{z1z2}$ is the average wind speed at z_1 ($\overline{u}_{z1}$) and z_2 ($\overline{u}_{z2}$), so that

$$\overline{u}_{z1z2} = \frac{\overline{u}_{z2} + \overline{u}_{z1}}{2}. \tag{2.25}$$

Based on eq. (2.24), IEC (2005) established an exponential coherence model that attempts to better capture the co-coherence at large separation distances,

$$\gamma_{IEC}(\Delta s, f) = \exp\left[-12\sqrt{\left(\frac{f\Delta s}{\overline{u}_{hub}}\right)^2 + \left(\frac{0.12\Delta s}{L_i}\right)^2}\right] \tag{2.26}$$

where $\overline{u}_{hub}$ is the mean speed at hub height and Δs is the separation distance, either in the lateral (Δy) or vertical direction (Δz). In IEC (2005), eq. (2.26) is only defined for the along-wind component u.

Figure 2.1 and fig. 2.2 present the co-coherence of all three velocity components for vertical separations $\Delta z = 20\,\text{m}$ and $\Delta z = 100\,\text{m}$ respectively. The Davenport co-coherences in eq. (2.24) were established using coefficients $c_z^u = 12$, $c_z^v = 10$, and $c_z^w = 3$.

The Davenport Coherence Model (eq. (2.24)) and the IEC-Davenport Coherence Model (eq. (2.26)) give similar co-coherence for the along-wind component but not for the lateral and vertical components (fig. 2.1). This is due to the use of the same decay coefficient for the along-wind component, $c = 12$.

2.3.2 Uniform Shear/Spectral Tensor Model

Mann (1994) proposed a spectral tensor model for the near-neutral atmosphere that describes the second-order structure of turbulence using only

three parameters, namely, $\alpha\varepsilon^{2/3}$, Γ, and L_M. $\alpha\varepsilon^{2/3}$ measures the energy dissipation of turbulence, L_M reflects the eddy size, and Γ quantifies the degree of anisotropy. This spectral tensor assumes isotropic turbulence as an initial state, which is distorted by a linear shear. The distortion causes the eddies to stretch and break, with the lifetime of the eddies being captured in the parameter Γ.

The uniform shear model used in the thesis is based on the model without the blocking effect of the ground. The uniform shear model which includes the blocking effect is fairly complex, hence the model without the blocking effect is deemed sufficient for most engineering uses (Mann, 1994). The analytical formulation of the uniform shear model is not provided here for brevity but is available in Mann (1994).

The uniform shear model gives negative γ_v for $n > 0.18$ as shown in fig. 2.1 and for $n > 0.16$ in fig. 2.2. For $\Delta z = 100\,\text{m}$ in fig. 2.2, as the frequency ≈ 0, the co-coherence of the along-wind component is lower than unity, as was also noted by Kristensen and Jensen (1979).

2.3.3 Pointed-Blunt Model (Neutral)

The Pointed-Blunt Model was derived using two years of measurement data from the FINO1 Platform (Cheynet et al., 2018). The measurements were carried out at heights of 41.5 m to 81.5 m above sea level (asl) (Neumann and Nolopp, 2007). The turbulence spectrum for each velocity component is composed of a "pointed" spectrum and a "blunt" spectrum. This terminology is taken from Olesen et al. (1984). The blunt model has a similar form to the spectra given in eqs. (2.19) and (2.20). The pointed model creates a spectral peak in the low-frequency range and has the same formulation as eq. (2.21).

For a neutral atmosphere, the Pointed-Blunt spectra are

$$\frac{fS_i}{u_*^2} = \frac{a_1^i n}{(1+b_1^i n)^{5/3}} + \frac{a_2^i n}{1+b_2^i n^{5/3}} \tag{2.27}$$

where a_1^i, a_2^i, b_1^i, and b_2^i are coefficients that are estimated by fitting the function to the spectral estimates in the least-square sense. This model captures the spectra in the low frequencies better than the Kaimal spectra (eqs. (2.19) to (2.21)). Secondly, the model aims to capture the flat spectral

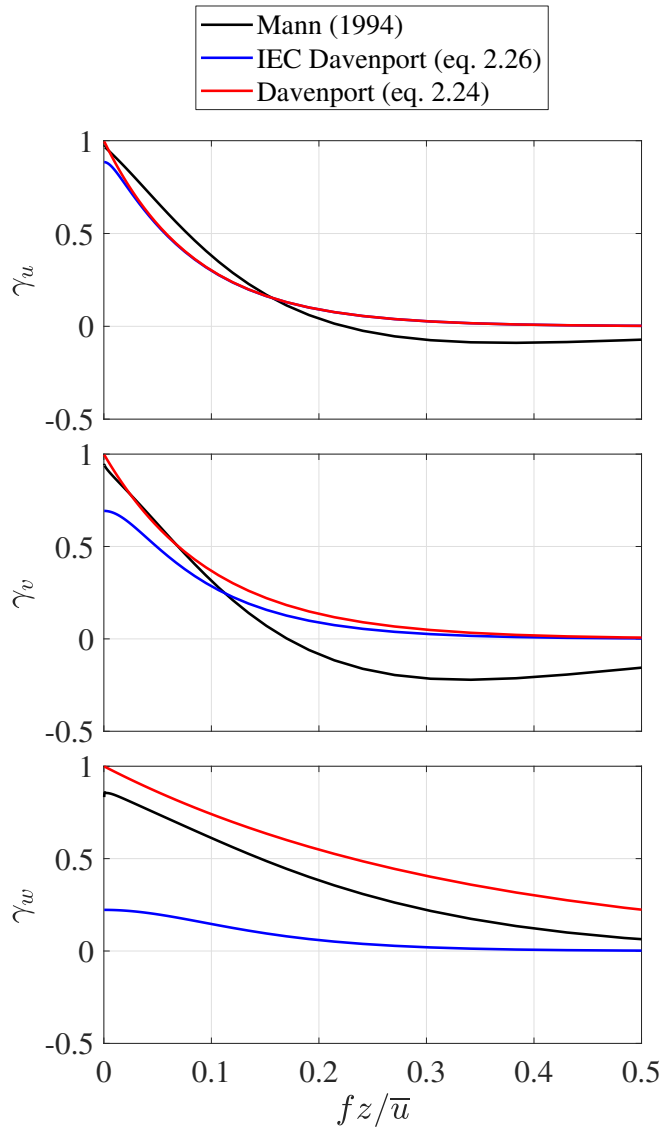

Figure 2.1: Co-coherence for vertical separation $\Delta z = 20\,\mathrm{m}$ of the three velocity components as a function of reduced frequency, eq. (2.22). $\overline{u} = 40\,\mathrm{ms}^{-1}$ and $z = 41.5\,\mathrm{m}$. γ_u is the co-coherence for u, γ_v for v, and γ_w for w.

peak due to eddy distortion for near-neutral atmospheres (Högström et al., 2002; Drobinski et al., 2004).

Figure 2.3 compares the non-dimensional near-neutral velocity spectra

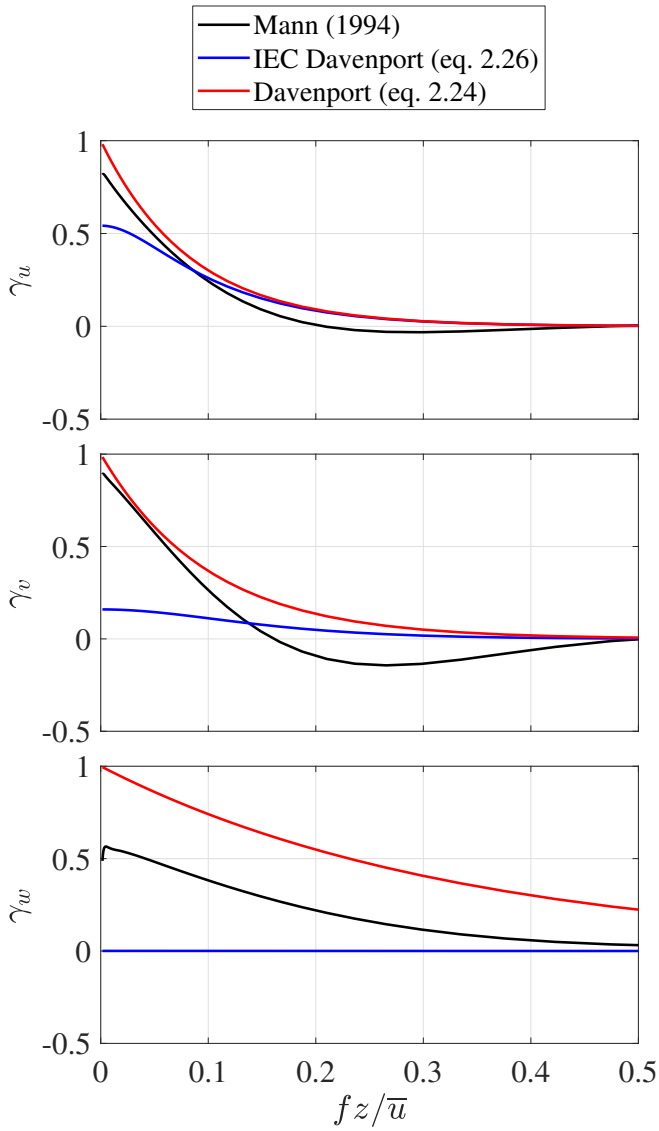

Figure 2.2: Same as fig. 2.1, but for $\Delta z = 100\,\mathrm{m}$.

using Kaimal and Finnigan (1994); Mann (1994); Cheynet et al. (2018). The flat spectral peak for the along-wind component is visible in the Pointed-Blunt Model as shown in fig. 2.3, top panel.

In the present thesis, the one-point spectra shown in eq. (2.27) are paired with the IEC exponential coherence model (eq. (2.26)) in Putri et al. (2020a,b) to simulate near-neutral atmospheric stability conditions.

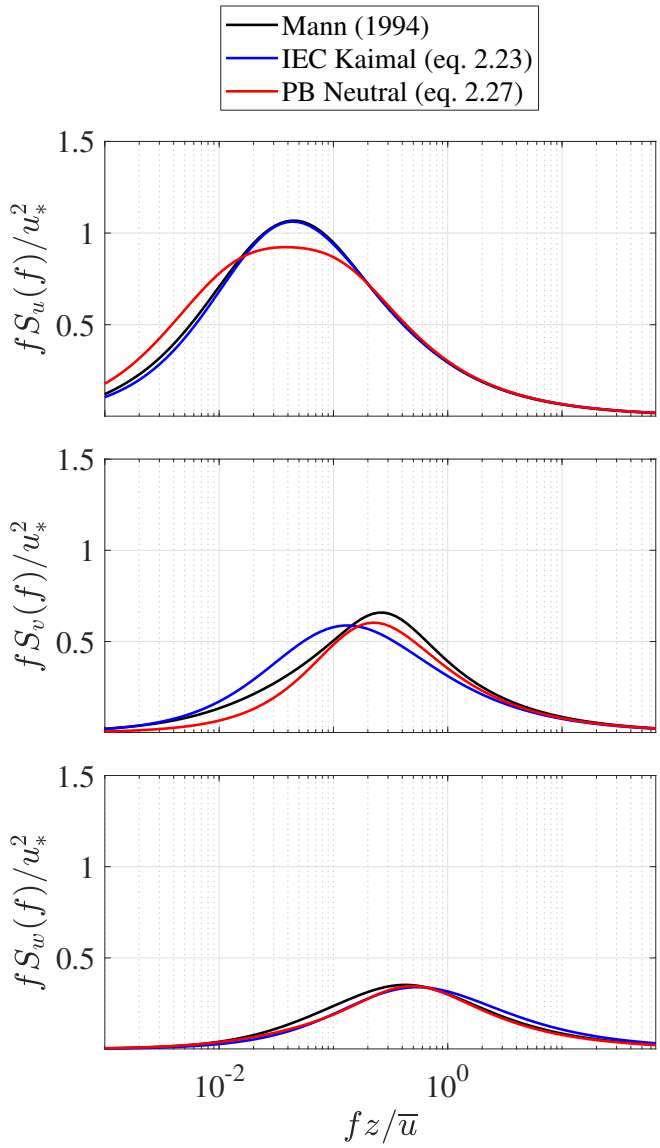

Figure 2.3: Non-dimensional velocity spectra for near-neutral condition of the three velocity components as a function of reduced frequency, eq. (2.22). $\overline{u} = 40\,\mathrm{ms}^{-1}$ and $z = 41.5\,\mathrm{m}$.

Additionally, in Putri and Obhrai (2022), eq. (2.27) is combined with the co-coherence function following Cheynet et al. (2018). The co-coherence

function from Cheynet et al. (2018) is written as

$$\gamma_i(\Delta z, f) \approx \exp\left\{-\left[\frac{\Delta z}{\overline{u}_{z1z2}}\sqrt{(c_1^i f)^2 + (c_2^i)^2}\right]\right\} \tag{2.28}$$

where $i = u, v, w$ in γ_i, and c_1^i as well as c_2^i are coefficients derived from the measured data on the FINO1 Platform.

2.4 Turbulence models for non-neutral atmosphere

This section describes the turbulence models that were developed for non-neutral conditions, namely the Højstrup Spectral Model (Højstrup, 1981) and the Pointed-Blunt Model (Cheynet et al., 2018).

2.4.1 Højstrup Spectral Model

Højstrup (1981) developed a turbulence spectral model for unstable atmospheres, consisting of a low-frequency part and a high-frequency part. The low-frequency part for u and v scales with the inversion height z_i and is a function of the atmospheric stability, while the w spectrum scales with height z. The high-frequency part for all velocity components scales with height z.

The Højstrup Spectral Model was compared with measurements at heights less than 12 m from the Risø78 experiment (Peterson et al., 1980). The spectra for all velocity components are read as,

$$\frac{fS_u(f)}{u_*^2} = \frac{0.5n_i}{\left(1+2.2n_i^{5/3}\right)}\left(\frac{z_i}{-L}\right)^{2/3} + \frac{105n}{(1+33n)^{5/3}} \tag{2.29}$$

$$\frac{fS_v(f)}{u_*^2} = \frac{0.32n_i}{\left(1+1.1n_i^{5/3}\right)}\left(\frac{z_i}{-L}\right)^{2/3} + \frac{17n}{(1+9.5n)^{5/3}} \tag{2.30}$$

$$\frac{fS_w(f)}{u_*^2} = \frac{32n}{(1+17n)^{5/3}}\left(\frac{z}{-L}\right)^{2/3} + \frac{2n}{\left(1+5.3n^{5/3}\right)} \tag{2.31}$$

where $n_i = fz_i/\overline{u}$ and L is the Obukhov length.

In Putri et al. (2019), the Højstrup Spectral Model given in eqs. (2.29) to (2.31) is combined with the Davenport Coherence Model (Davenport,

1977), which considers both lateral and vertical separations, as

$$\gamma_{Davenport2}(\Delta y, \Delta z, f) = \exp\left[-\sqrt{\left(\frac{c_y^i f \Delta y}{\overline{u}_{z1z2}}\right)^2 + \left(\frac{c_z^i f \Delta z}{\overline{u}_{z1z2}}\right)^2}\right] \quad (2.32)$$

where Δy is the separation distance in the lateral direction, c_y^i and c_z^i are respectively the exponential decay coefficients for the lateral and vertical separations, provided in table 2.1.

Table 2.1: Decay coefficients used for Equation (2.32)

Coefficient	c_y^u	c_y^v	c_y^w	c_z^u	c_z^v	c_z^w
Value	7	7	6.5	10	10	3

2.4.2 Pointed-Blunt Model (Non-neutral)

The Pointed-Blunt Model accounting for unstable atmospheric stability conditions follows the same form as eq. (2.27) where coefficients a_1^i, a_2^i, b_1^i, and b_2^i are defined in Cheynet et al. (2018). For a stable atmospheric stability condition, the turbulence spectra are,

$$\frac{fS_i}{u_*^2} \approx c_1 n^{-2/3} + \frac{a_2^i n}{1 + b_2^i n^{5/3}} + a_3 n^{-2} \quad (2.33)$$

where coefficients a_2^i, a_3, b_2^i, and c_1 are given in Cheynet et al. (2018).

Figure 2.4 compares the velocity spectra from Kaimal and Finnigan (1994) for a near-neutral condition as well as for an unstable condition ($\zeta = -0.5$) from Højstrup (1981) and Cheynet et al. (2018). The Højstrup Spectral Model shifts the spectral peak of all velocity components to lower frequencies, compared to the Kaimal Model for a near-neutral condition. This spectral peak shift is as described by Smedman-Högström and Högström (1975). The Pointed-Blunt Model gives two spectral peaks, which are noticeable for the three wind components.

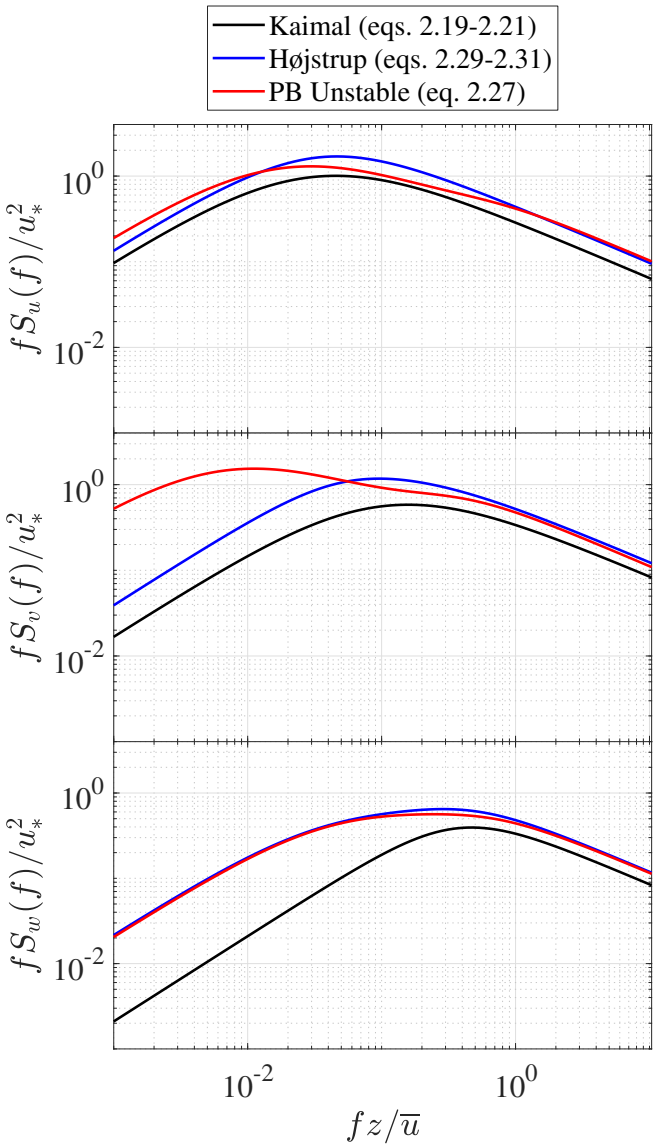

Figure 2.4: Non-dimensional velocity spectra of the three velocity components as a function of reduced frequency (eq. (2.22)), for $\zeta = -0.5$. $\overline{u} = 40\,\mathrm{ms}^{-1}$, $z = 41.5\,\mathrm{m}$, and $z_i = 700\,\mathrm{m}$.

To describe unstable atmospheric turbulence, Putri et al. (2020a,b) combined the Pointed-Blunt Spectral Model with the co-coherence formulation shown in eq. (2.26). In Putri and Obhrai (2022), the Pointed-Blunt Spectral Model is used together with the co-coherence in eq. (2.28) for both unstable

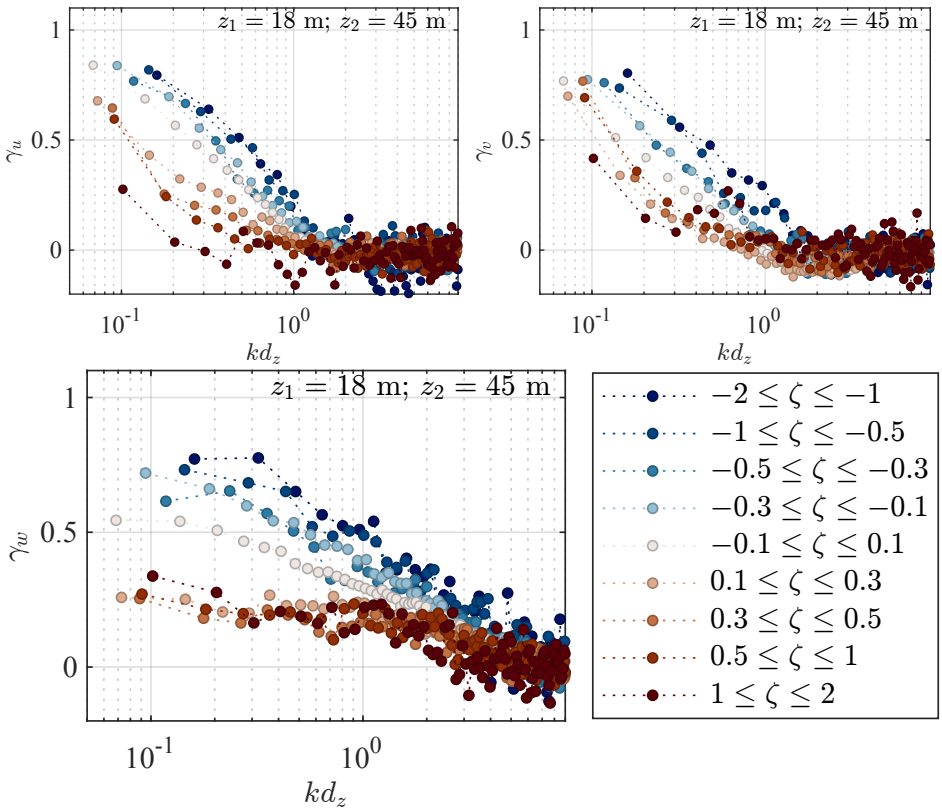

Figure 2.5: Estimated co-coherence at Vindeby for all velocity components as a function of various atmospheric stability conditions (Putri et al., 2022). $k = 2\pi f/\overline{u}_{z1z2}$ is the wave number and $d_z = \Delta z$.

and stable conditions.

Figure 2.5 shows the estimated co-coherence as a function of the atmospheric stability at Vindeby for $\Delta z = 27$ m. The range of atmospheric stability considered is $-2 \leq \zeta \leq 2$. The co-coherence decreases as the atmospheric stability changes from unstable, to near-neutral, and to stable. This is observed for all velocity components.

2.5 Influence of turbulence spectra on FOWT loads and motions

The influence of one-point and two-point spectra on the structural loads of state-of-the-art FOWTs has previously been investigated by, e.g. Bachynski and Eliassen (2019); Doubrawa et al. (2019). They compared the resulting floater displacements and the hourly damage equivalent loads (DELs) using the Uniform Shear Model and the IEC Davenport-Kaimal Model. Both models resulted in different wind loading on the FOWT, which were thought to be due to different co-coherence inputs.

The influence of the co-coherence on the structural response depends on the mode shapes. For a linear structure, this influence can be quantified using the so-called joint acceptance function (p. 81 Dyrbye and Hansen, 1997). If the mode shape has a constant sign, increasing co-coherence is likely to be associated with an increasing response. If the mode shape changes sign across the structure, a larger modal response may be obtained for a lower co-coherence, depending on the resonant frequency and the characteristics of the mode shapes (Cheynet, 2018).

Sathe et al. (2013) investigated the simulated fatigue loads of a bottom-fixed 5 MW WT using the Uniform Shear Model (Mann, 1994) considering (i) varying atmospheric stability from site-specific measurements, (ii) near-neutral stability from site-specific measurements, and (iii) IEC-specified parameters for the Uniform Shear Model (IEC, 2005). The fatigue damage was quantified in proportion to the mean wind speed and atmospheric stability distribution. The variable atmospheric stability case yielded 17% lower tower loads than when only near-neutral stability was considered. The blade loads were not affected by the atmospheric stability. The IEC case resulted in 96% higher tower base fatigue damage than the site-specific case.

2.6 Coupled aeroelastic simulation of offshore wind turbine

This section provides the basic background to aero-hydro-servo-elastic simulations, including the Blade Element Momentum (BEM) theory, the Simulation Workbench for Marine Application (SIMA) aeroelastic tool, as

well as the wind turbine models used in the thesis.

2.6.1 Blade Element Momentum theory

BEM theory states that the wind flow experienced by the blades can be described by considering a two-dimensional (2D) flow acting on a local airfoil cross-section. This is a consequence of the magnitude of the along-wind component and the tangential rotational velocity of the blade being dominant over the lateral wind component v (Hansen, 2015). Figure 2.6 illustrates the local velocities and forces on an airfoil cross-section.

According to the blade element theory (Moriarty and Hansen, 2005; Hansen, 2015), the local differential thrust force (dT), the local differential tangential force (dF_t), and the local differential torque (dQ) are respectively

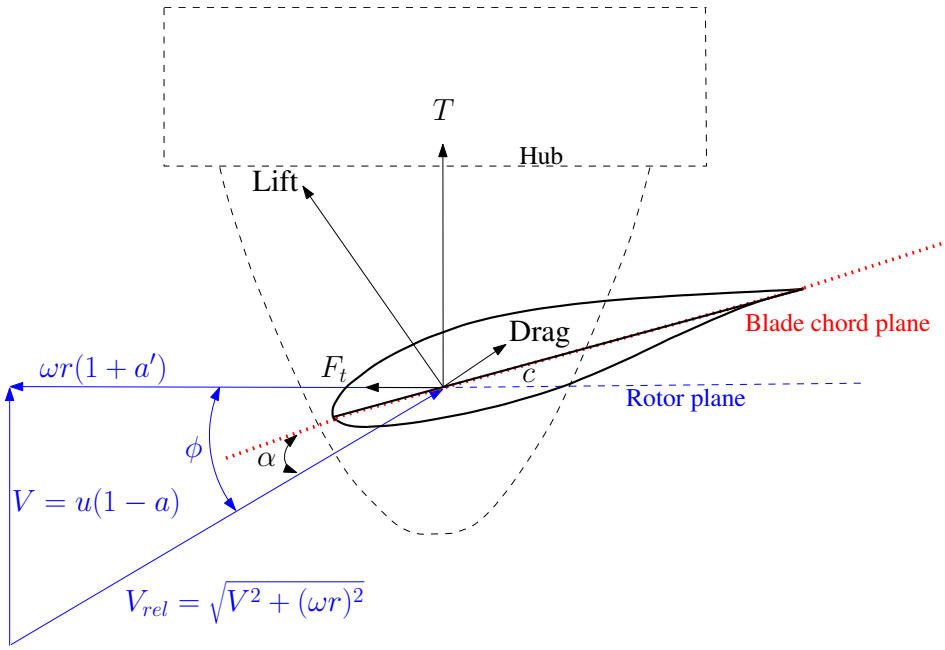

Figure 2.6: Local airfoil element definition. V is the incoming wind speed reduced by an induction factor a, ω is the rotational speed, a' is the tangential induction factor, V_{rel} is the relative wind speed, α is the angle of attack, ϕ is the local inflow angle, c is the local airfoil length, T is the thrust force, and F_t is the tangential force.

calculated as

$$\mathrm{d}T = \frac{1}{2} B\rho c V_{rel}^2 \left[C_l(\alpha)\cos\phi + C_d(\alpha)\sin\phi\right]\mathrm{d}r \tag{2.34}$$

$$\mathrm{d}F_t = \frac{1}{2} B\rho c V_{rel}^2 \left[C_l(\alpha)\sin\phi - C_d(\alpha)\cos\phi\right]\mathrm{d}r \tag{2.35}$$

$$\mathrm{d}Q = r\mathrm{d}F_t \tag{2.36}$$

where B denotes the number of blades, ρ is the density of air [$\mathrm{kg\,m^{-3}}$], c is the local airfoil length, V_{rel} is the relative wind speed, α is the angle of attack, ϕ is the local inflow angle, $\mathrm{d}r$ is the radial increment of the blade, r is the radial position of the local airfoil, C_l and C_d are respectively the lift and drag coefficients. Due to the 'tapered' nature of the blade, both C_l and C_d are not constant along the blade span. These coefficients are normally provided for a specific airfoil type as a function of α.

Substituting V_{rel} with the incoming wind speed u and the induction factors a also a' according to the momentum theory, eqs. (2.34) and (2.35) are rewritten as

$$\mathrm{d}T = 4\pi r\rho u^2 a(1-a)\mathrm{d}r \tag{2.37}$$

$$\mathrm{d}F_t = 4\pi r^2\rho u\omega a'(1-a)\mathrm{d}r \tag{2.38}$$

The classical BEM theory is established by combining eqs. (2.34) to (2.38) to compute induction factors a as well as a'. A more advanced BEM theory may include additional corrections such as Prandtl's tip-loss correction (Glauert, 1935), Glauert's tip correction (Glauert, 1926), hub-loss correction (Moriarty and Hansen, 2005), skewed-wake correction or dynamic inflow (Pitt and Peters, 1981; Snel and Schepers, 1995), and tower blockage correction (Bak et al., 2001).

This thesis adopts an aerodynamic model on the rotor blades which does not take into account the unsteady aerodynamic effects. Nonetheless, a dynamic inflow model is incorporated, which has been shown (e.g. by Papi et al. (2023)) to be important in accurately modelling the aerodynamics of FOWTs.

Turbulence fluctuations of the wind velocity across a WT rotor could affect the overall wind loading. As sketched in fig. 2.6, the along-wind component would alter the angle of attack, which would then affect the forces. Since turbulence is a three-dimensional process, variations in the

wind load are expected along the blade span and among the three blades.

2.6.2 Aero-hydro-servo-elastic tool

All numerical simulations of the FOWT were performed using the Simulation Workbench for Marine Application (SIMA) (SINTEF, 2022). The tool couples the large-body floater analysis in Simulation of Marine Operations (SIMO) and the finite element analysis (FEA) in RIFLEX. The SIMO module calculates the motions of rigid bodies, including the floater and the nacelle/hub. RIFLEX computes the deflections and forces of flexible structures including the tower, blades, and mooring lines. The aerodynamic loads are calculated using RIFLEX-Coupled Wind Turbine, where the classical BEM theory including Prandtl's tip-loss correction and dynamic inflow is applied.

A coupled SIMO-RIFLEX analysis requires environmental inputs such as wind, waves, and currents. In this thesis, the currents loads have been disregarded and the same wave condition has been applied for all turbulent wind load cases, due to the emphasis on the varying turbulent wind input conditions. The wind input is provided as a multi-point time series over the rotor-swept area.

The wave time series were generated using the JONSWAP spectrum (Hasselmann et al., 1980) by defining the values of the significant wave height (H_S) and the corresponding wave peak period (T_p). The turbulent wind time series were generated using three different tools for each turbulent model: TurbSim (Jonkman, 2016) for the Davenport-Kaimal Model, Mann Turbulence Generator (MTG) (Larsen and Hansen, 2019) for the Uniform Shear Model, and windSimFast (Cheynet, 2020) for the Pointed-Blunt Model, the Højstrup Spectral Model, and the Davenport-Kaimal Model in Putri et al. (2019).

The wind turbine controller used in this thesis comprises two basic systems that operate independently. Firstly, a generator-torque controller which is activated when $\overline{u}_{hub}$ is below the rated speed, to optimise the power generation. Secondly, a collective blade-pitch controller is activated when $\overline{u}_{hub}$ is above the rated speed, to maintain constant torque and to minimise the load on the rotor.

Table 2.2: OC3-Hywind key parameters.

Parameter	Value
Rotor configuration	3-bladed, upwind
D_{rot}	126 m
z_{hub}	90 m asl
Cut-in, rated, cut-out speed	3 m s^{-1}, 11.4 m s^{-1} and 25 m s^{-1}
Cut-in, rated rotor speed	6.9 rpm, 12.1 rpm
Water depth	320 m
H_{draft}	120 m below sea level (bsl)
H_{trans}	12 m bsl
H_{fb}	10 m asl
H_{flead}	70 m bsl
Mooring	3 catenary lines
Mooring radius to anchor from platform centreline	853.87 m
D_1, D_2	6.5 m, 9.4 m

2.6.3 OC3-Hywind Spar Wind Turbine

The OC3-Hywind Spar Wind Turbine is part of the Offshore Code Comparison Collaboration (OC3) project. The OC3-Hywind project adopts the spar floater from the Hywind demo wind turbine developed by Equinor and pairs it with the 5 MW reference wind turbine established by the National Renewable Energy Laboratory (NREL) (Jonkman, 2010).

The OC3-Hywind is illustrated in fig. 2.7 and its main properties are provided in table 2.2. The OC3-Hywind spar floater has been modified from its original properties to adapt the NREL 5-MW baseline turbine (Jonkman, 2010).

The wind turbine deployed in OC3-Hywind has the same structural and aerodynamic properties of the hub, nacelle and rotor as the NREL 5-MW baseline turbine. The tower and the control system properties have been adjusted to fit the spar floater characteristics (Jonkman, 2010). The complete aerodynamic properties of the rotor can be found in Jonkman et al. (2009).

Currently, the FOWTs installed in Norway are based on a spar floater. One of the main reasons for this is that the turbines can be erected directly

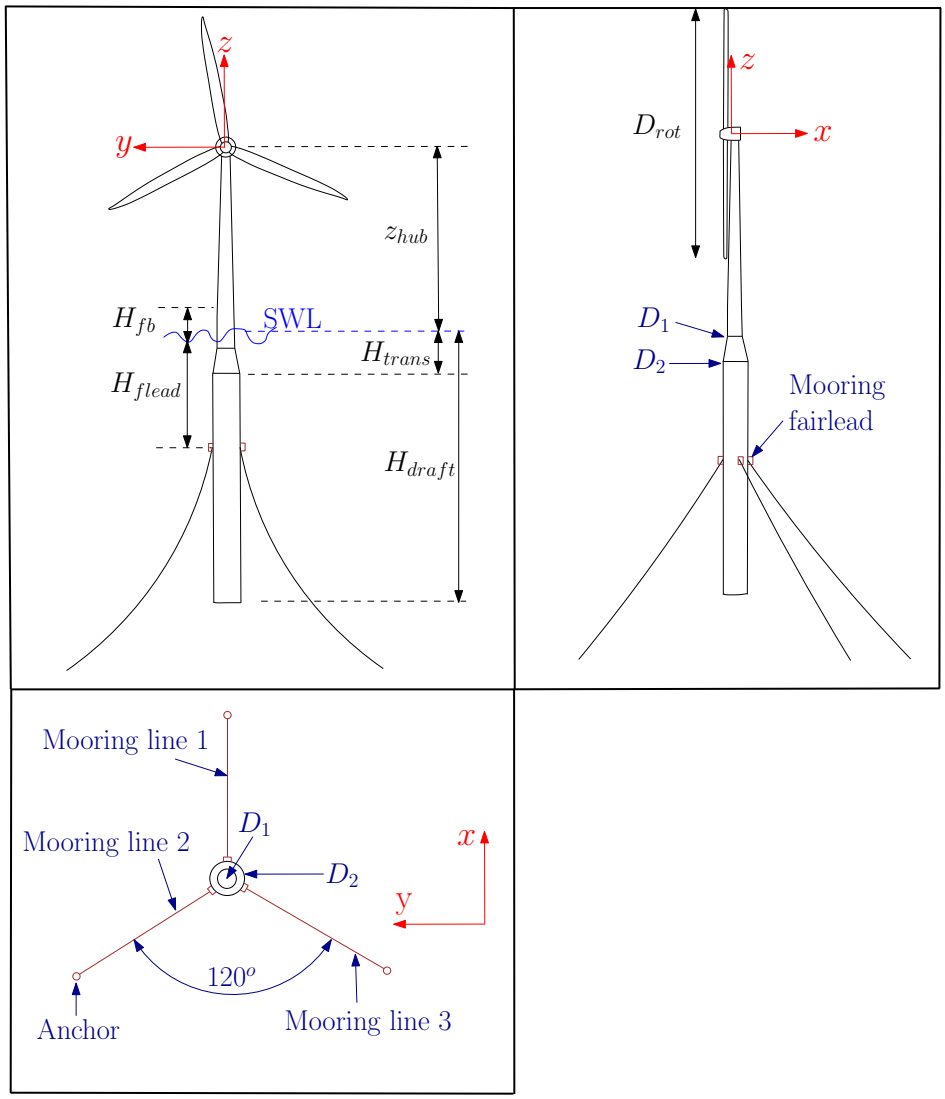

Figure 2.7: OC3 Hywind Wind Turbine sketch. Upper left panel shows the front view, upper right panel shows the side view, and bottom left panel shows the plan view of the turbine. Definitions are provided in table 2.2. SWL is the sea water level.

in deep-water Norwegian harbours. The spar turbine is therefore the main focus of this thesis.

Table 2.3: OC4-DeepCwind key parameters.

Parameter	Value
Rotor configuration	3-bladed, upwind
D_{rot}	126 m
z_{hub}	90 m asl
Cut-in, rated, cut-out speed	3 m s^{-1}, 11.4 m s^{-1} and 25 m s^{-1}
Cut-in, rated rotor speed	6.9 rpm, 12.1 rpm
Water depth	320 m
H_{draft}	20 m bsl
H_{ucol}, D_2	26 m, 12 m
H_{bcol}, D_3	6 m, 24 m
S_{col}	50 m
H_{fb}	10 m asl
H_{flead}	14 m bsl
D_1, D_{pon}	6.5 m, 1.6 m
Mooring	3 catenary lines
Mooring radius to anchor from platform centreline	837.6 m
Angle between adjacent mooring line	120°

2.6.4 OC4 DeepCwind Semi-submersible Wind Turbine

The OC4 DeepCwind Semi-submersible Wind Turbine is a part of the Offshore Code Comparison Collaboration Continuation (OC4) project. The DeepCwind was originally developed as a means to validate various aeroelastic tools (Robertson et al., 2014).

Figure 2.8 visualises the DeepCwind and table 2.3 presents its key parameters. Its semi-submersible floater is based on a prototype tested in a wave basin in the USA (Robertson et al., 2014). The prototype has been scaled up 50 times to become the DeepCwind model.

The DeepCwind floater consists of a main column and three offset columns. Each offset column is divided into an upper column and a base column (see fig. 2.8). These columns are connected by 12 pontoon members and three cross braces. DeepCwind has the NREL 5-MW baseline turbine with some modifications to the tower and control system properties to accommodate the floater's properties (Robertson et al., 2014).

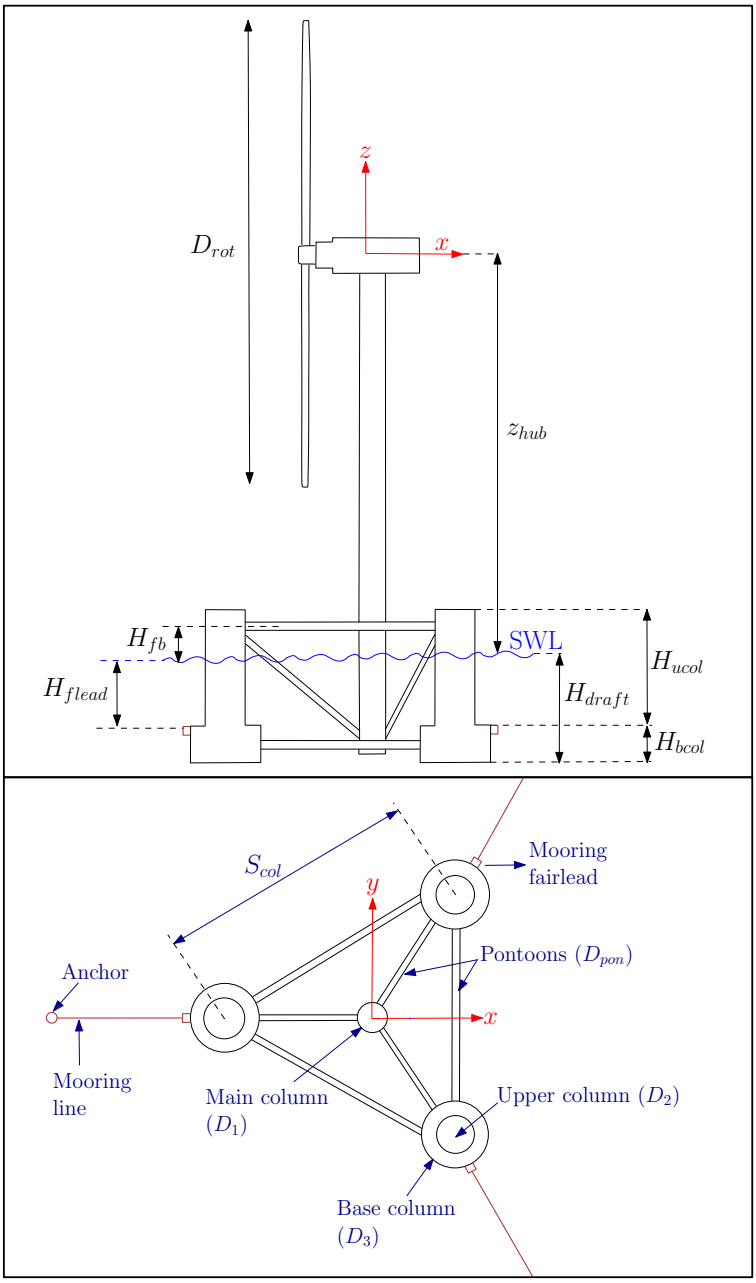

Figure 2.8: OC4 DeepCwind Wind Turbine sketch. Upper panel shows the side view and bottom panel shows the plan view of the turbine. Definitions are provided in table 2.3. SWL is the sea water level.

Chapter 3

Summary of papers

This chapter summarises the main findings from five papers included in the second part of the thesis. The five papers together cover how the thermal stratification of the atmosphere can be included in the design of FOWTs and the impact of non-neutral stratification on the loads and motions of a FOWT.

3.1 Paper 1 - Offshore wind turbine loads and motions in unstable atmospheric conditions

Paper 1 investigates the influence of an unstable atmosphere on the OC3-Hywind's structural loads and floater motions. The wind turbine design guideline, IEC 61400-1(IEC, 2005), recommends turbulent models that were originally derived for near-neutral stratification. However, non-neutral conditions are common above the ocean (Krogsæter and Reuder, 2015; Cheynet et al., 2018).

The unstable wind conditions are simulated using the Højstrup Spectral Model (Højstrup, 1981) (see section 2.4.1 in this thesis) paired with the Davenport Coherence Model (Davenport, 1977) (eq. (2.32)). The Davenport-Kaimal Model (Thresher et al., 1981) (section 2.3.1 in this thesis) is also used for comparison of the OC3-Hywind's responses under a near-neutral atmosphere. The simulated TI decreases as the absolute value of the Obukhov length increases and z_i decreases.

The tower top torsional moment, the tower base side-side bending moment, and the blade root flap-wise bending moment of the OC3-Hywind turbine are studied using DEL. These bending moments are the most

sensitive stress-resultants to atmospheric stability. The simulated DELs are 65%, 37%, and 24% higher in a very unstable atmosphere than in a neutral atmosphere, respectively for the tower top torsional moment, the tower base side-side bending moment, and the blade root flap-wise bending moment. The magnitude of the TI governs the magnitude of the tower top torsional moment DEL and the tower base side-side bending moment DEL. However, the blade root flap-wise bending moment does not show a clear dependency on atmospheric stability. The mooring line tension is also studied with respect to DEL, with the result that no clear dependence of the mooring line tension on atmospheric stability was found.

The floater's roll, sway, and yaw exhibit the greatest sensitivity to variation in atmospheric stability. The magnitude of the three floater's motions increases with the TI. It is therefore necessary to consider unstable thermal stratification when predicting the wind-induced response of the floater and bending moment DELs of state-of-the-art FOWTs.

3.2 Paper 2 - Numerical analysis of the effect of offshore turbulent wind inflow on the response of a spar wind turbine

Paper 1 considers a single co-coherence to obtain the floater motions and stress resultants of the OC3-Hywind. Paper 2 examines the effect of a one-point autospectrum and a two-point autospectrum on the structural loads and floater motions of the OC3-Hywind.

The OC3-Hywind's floater motions and fatigue loads induced by turbulent wind based on IEC (2005): the Uniform Shear Model (section 2.3.2 in this thesis) and the IEC Davenport-Kaimal Model (eqs. (2.23) and (2.26)) are compared. Additionally, the Pointed-Blunt Spectral Model (eq. (2.27)) is used to simulate near-neutral and unstable turbulent wind fields. For all stability conditions, eq. (2.27) is combined with the IEC-Davenport Coherence Model (eq. (2.26)).

The Uniform Shear Model and the IEC Davenport-Kaimal Model give different co-coherence levels depending on the separation distance and frequency. For the same variance of all velocity components, the two models give different magnitudes of floater motion and fatigue loads. The largest sensitivity to the wind co-coherence is experienced in terms of the

tower top torsional moment and the tower base side-side bending moment. The bending moments simulated using the Uniform Shear model are 27% and 20% higher than those simulated using the IEC Davenport-Kaimal model. Sway, roll and yaw of the floater show the greatest sensitivity to the co-coherence, which captures the spatial variability of turbulence.

The greatest sensitivity to atmospheric stability is noted for the tower top torsional moment and the tower base side-side bending moment when simulating turbulence using the Pointed-Blunt Spectral Model. Comparing an unstable condition ($\zeta = -1.63$) and a near-neutral condition ($\zeta \approx 0$), the tower top torsional moment and the tower base side-side bending moment vary by 27% each. Similar to the simulated results when using the Højstrup Spectral Model in Paper 1, strongly unstable atmospheres induce the largest TI, and the TI decreases as the stability changes to near-neutral, where the magnitude of the DELs follows.

Both one-point and two-point autospectra introduce uncertainty in the simulated fatigue loads and floater motions of the OC3-Hywind. Paper 2 concludes by recommending the use of site-specific wind measurements that account for non-neutral atmospheres for the design of a spar FOWT, where available.

3.3 Paper 3 - Response sensitivity of a semisubmersible floating offshore wind turbine to different wind spectral models

Paper 3 studies the influence of different inflow conditions on the responses of a semi-submersible FOWT, the OC4 DeepCwind. The wind fields are generated by considering the same load cases as Paper 2: the Uniform Shear Model (section 2.3.2 in this thesis), the IEC Davenport-Kaimal Model (eqs. (2.23) and (2.26)), and the Pointed-Blunt Spectral Model (eq. (2.27)) for a near-neutral atmosphere. Unstable atmospheres are simulated using the Pointed-Blunt Spectral Model. The IEC-Davenport Coherence Model (eq. (2.26)) is joined with the Pointed-Blunt Spectral Model for all atmospheric stratifications.

The floater yaw and the yaw twisting moment are shown to be the most sensitive to wind inflow conditions, while the floater sway and the tower base side-side bending moment are the second most sensitive. This was

also observed for the spar wind turbine OC3-Hywind in Paper 2. This may be due to several factors, particularly the use of the same turbine, (NREL 5 MW offshore baseline) and hence the same blade-pitch control system.

The sensitivity to atmospheric stability is also evident in the displacement response of the floater and the structural fatigue loads. The tower torsional moment and the tower side-side bending moment DELs are 28% higher in unstable atmospheres than in neutral atmospheres. Paper 3 recommends the inclusion of proper modelling of wind spectral density and co-coherence when simulating the fatigue loads and floater motions of a semi-submersible FOWT.

3.4 Paper 4 - Turbulence in a coastal environment: the case of Vindeby

Paper 4 analyses turbulence spectral characteristics from wind records at the Vindeby offshore wind farm, from a mast called South Mast West (SMW). This paper aims to identify similarities between the turbulence characteristics at Vindeby and those at the FINO1 platform in the North Sea. The dataset analysed includes the measurements at 6 m, 18 m and 45 m asl.

Despite their proximity to the sea surface, the sonic anemometers are mostly located above the wave boundary layer. Measurements at 18 m asl follow the surface-layer scaling. Furthermore, the power spectral density of the along wind velocity component at 18 m and 45 m asl is consistent with the empirical spectral models estimated at 41 m on FINO1.

The estimated vertical co-coherence of the along-wind component for near-neutral atmospheres could be described by the same 3-parameter exponential decay function as used on FINO1. An exception is the co-coherence of the lateral wind component due to the closer distance to the sea surface. The co-coherence estimates of the three turbulent components are lowest for stable thermal stratification and highest for unstable stability conditions.

Paper 4 concludes that the Vindeby dataset could be considered representative for the design of OWTs despite being recorded below the height of the state-of-the-art OWTs. This is due to the consistency of turbulence characteristics between Vindeby and FINO1. Paper 4 also suggests that

future wind measurements at offshore sites should include heights up to 250 m asl to capture turbulence information where the surface-layer scaling may no longer be relevant.

3.5 Paper 5 - Wind-induced response of an offshore wind turbine under non-neutral conditions: A comparison with Hywind Scotland

Paper 5 compares the wind-induced responses of a spar FOWT (5 MW OC3-Hywind) from numerical simulations with measurements from a 6 MW spar FOWT at the Hywind Scotland wind farm. Different stability conditions were considered and the response components of interest were pitch and yaw. The numerical simulations use turbulence spectra in eqs. (2.27) and (2.33) combined with the co-coherence function in eq. (2.28) to simulate the wind fields.

The simulated and measured platform pitch and yaw displacement responses are consistent. The floater pitch increases with the mean wind speed up to the rated speed and decreases when the wind speed is greater than the rated speed due to the blade-pitch control system. As the atmospheric stability moves from moderately stable ($0.3 \leq \zeta < 0.5$) to moderately unstable ($-0.5 \leq \zeta < -0.5$), the platform pitch and yaw displacements increase in both simulations and observations.

The discrepancy in the Hywind Scotland responses between stable and unstable conditions is greater than the simulated responses. This may be partly due to the different platform sizes, as well as the different methods used to classify the atmospheric thermal stratification. The effect of atmospheric stability on lateral co-coherence is not fully understood due to a lack of full-scale observations. It is assumed that the vertical and lateral co-coherences are the same, which is a limitation of this study. This may also contribute to the observed deviation. Paper 5 concludes that the use of appropriate turbulence modelling in aeroelastic simulations of OWTs could reasonably predict the platform degree of freedom (DOF) responses of a spar FOWT.

Chapter 4

Conclusions and future works

4.1 Conclusions

The five papers summarised in this thesis altogether provide a framework for considering the atmospheric stability in the design of floating offshore wind turbines (FOWTs) and its consequences on the floater motions and fatigue loads of a 5 MW spar FOWT (OC3-Hywind) and a 5 MW semi-submersible FOWT (OC4 DeepCwind). The influence of atmospheric stability on the loading of the two FOWTs is assessed using the one-point and two-point turbulence autospectra from several turbulence models.

Paper 1 and Paper 2 conclude that the OC3-Hywind floater degrees of freedom (DOFs) and fatigue loads are sensitive to the thermal stratification of the atmosphere. Specifically, the fatigue damage could be 65% greater for very unstable atmospheres than for neutral atmospheres. Paper 3 concludes that the DeepCwind floater's DOFs and structural bending moments are also responsive to atmospheric stability. Paper 5 shows that the simulated OC3-Hywind displacement responses compare reasonably well with the measured full-scale data of the Hywind Scotland spar turbine. However, there is still considerable uncertainty about the appropriate parameters to simulate co-coherence for lateral separations at distances and heights relevant to modern FOWTs.

Paper 4 shows that the spectral characteristics of the turbulence at a coastal site (Vindeby) are consistent with those at an offshore site (FINO1 platform). This consistent behaviour is very encouraging for the development of turbulence models for the design of state-of-the-art FOWTs.

This thesis recommends the use of turbulence information, where avail-

able, taking into account atmospheric stability for the design of FOWTs. Especially, the knowledge of the co-coherence for both lateral and vertical separations. Paper 4 shows that non-neutral atmospheres could occur quite frequently at an offshore site, particularly at the operational speeds of FOWTs. Hence, integrating the knowledge of atmospheric stability into a FOWT design, e.g. by accurately predicting fatigue loads, could help optimise the capital expenditure (CAPEX) and operating expense (OPEX) of the FOWT.

4.2 Future works and recommendations

To improve the modelling of wind loading on state-of-the-art FOWT fatigue loads and DOF responses, several recommendations are made for future studies.

The first is to perform aeroelastic simulations using the latest wind turbine designs with rotor diameters up to 220 m. These larger turbines are becoming increasingly common for commercial use. Secondly, to carry out wind measurements at heights above 100 m. This data could provide essential information for turbulence modelling in aeroelastic simulations, particularly the knowledge of the co-coherence for lateral and vertical separations. Thirdly, the inclusion of wake effects in aeroelastic simulations by taking into account atmospheric stability would be valuable to better understand the interactions between turbines within a wind farm. Finally, the use of non-linear load-displacement mooring models would provide a more accurate simulation of the dynamic behaviour of FOWTs.

Part II

Paper 1
Offshore wind turbine loads and motions in unstable atmospheric conditions

*Rieska Mawarni Putri[1], Charlotte Obhrai[1], and Julie-Ann Marie Knight[1]
[1]Department of Mechanical and Structural Engineering and Materials Science, University of Stavanger, Norway

IOP Conf. Series: Journal of Physics: Conf. Series **1356** (2019) 012016 doi:10.1088/1742-6596/1356/1/012016

Offshore Wind Turbine Loads and Motions in Unstable Atmospheric Conditions

R M Putri[1], **C Obhrai**[1] **and J M Knight**[1]

[1]Department of Mechanical and Structural Engineering and Material Science, University of Stavanger, Norway

Abstract. Even though it is widely known that unstable atmospheric stability conditions can lead to higher turbulence, the use of proper turbulent wind models considering unstable conditions are not often used in the simulation of loads and motions of offshore wind turbines. For this reason, the Højstrup model, which was specifically developed for unstable conditions, is used to simulate a spar-buoy offshore wind turbine (OWT) and investigate the importance of unstable conditions in the design of floating offshore wind turbines. It is found that fatigue damage of a spar-buoy OWT is strongly influenced by unstable conditions, where very unstable condition gives 65% higher fatigue damage than neutral conditions for the tower top torsion, followed by 37% higher for tower base side-side bending and 24% higher for blade root flap-wise mode.

1. Introduction

The fast development of offshore wind turbines in the recent years has brought offshore wind into deeper waters with the help of floating platform concepts. Floating platform concepts can be divided in three different groups based on how the platform gains stability: buoyancy, station-keeping system, and gravity-based. The buoyancy group relies on the water plane area to gain its stability, such as a barge type floater. Tensioned-leg platform falls into the station-keeping system group where it depends on its tendons both to gain stability and as a station-keeping system. The gravity-based group relies on its weight to gain stability where spar-floater is included in this group since the platform is ballasted to obtain sufficient weight. While the knowledge of floating platforms is available from the oil and gas experience, the use of large rotor turbines on floating platforms has become a challenge due to uncertainties in turbulent wind models which may cause excessive platform motions. Depending on the floater type, a specific degree of freedom (DOF) could be more prominent than other DOFs. Excessive motions can also lead to severe fatigue damage on floating offshore wind turbine (FOWT) components which need to be thoroughly assessed in the design of FOWTs.

One of the reasons for the pronounced platform motions is the excitation from low frequency turbulent wind that is within the range of floating platforms natural frequencies (< 0.05 Hz for typical platform translation DOFs). When considering turbulent wind, the influence of air temperature –known as atmospheric stability– cannot be ignored except for the case of extreme winds [1]. Atmospheric stability is associated with vertical movement of air parcels depending on air's temperature. When the air parcels' temperature is colder than the surrounding air, then they sink resulting in stable conditions. The opposite creates unstable conditions where air parcels are warmer than the surrounding air and they rise creating buoyant-generated turbulence. By including the effect of atmospheric stability, a more accurate fatigue load and platform motion estimation can be achieved for the design of FOWTs. In the current available OWT design standard (IEC 61400 [2]) two turbulent wind models are recommended by assuming only neutral atmospheric conditions: the Kaimal model with a given exponential coherence model and the Mann uniform shear turbulence model [3]. Meanwhile, analysis of offshore wind

measurement data has shown that unstable atmospheric conditions are most prevalent offshore, notably during winter time composing approximately 48.6% occurrence in a year [4].

This study aims to investigate the influence of unstable atmospheric conditions on the OC3-Hywind turbine [5] loads and motions with the use of the Højstrup 1981 [6] wind model. These results were compared with the Kaimal model [7] which represents neutral atmospheric conditions. MATLAB codes [8] were used to generate turbulent wind fields based on the Højstrup spectral model combined with the Davenport Coherence function [9], as well as the Kaimal spectral model combined with the Davenport Coherence function as input to coupled SIMO-RIFLEX [10] simulations of the OC3-Hywind.

2. Theoretical background

Højstrup spectral model is one of the turbulent wind models designed to simulate unstable atmospheric conditions. The model was developed based on measurements taken in Kansas in 1968 and Minnesota in 1973, and showed a good agreement with data from the RISØ 1978 experiment [6]. This model is an extension of the Kaimal spectral model and comprises two semi-empirical spectra [6]:

$$S(n) = S_L(n) + S_M(n) \tag{1}$$

where $S_M(n)$ is the Kaimal spectra and $S_L(n)$ characterises the low-frequency part of the spectra [6]. The low frequency part of the spectra may be important when considering the loads and motions of large FOWTs as their natural frequencies tend to lie within the low frequency range.

Kaimal spectra are derived based on the Kansas measurements with the approach of collapsing all spectra into universal curves in the inertial subrange, and the spectral behaviour at lower frequencies are observed as a function of the stability parameter z/L (where z is height above surface and L is Obukhov length) [7]. Inertial subrange spectral behaviour converges to a -2/3 line at the high frequency end, while at low frequencies, the spectra depend on z/L [7]. The empirical spectral formulas for neutral lapse rate as proposed by Kaimal for u, v, and w wind components are [7]:

$$\frac{nS_u(n)}{u_*^2} = \frac{105\,f}{(1+33\,f)^{5/3}} \tag{2}$$

$$\frac{nS_v(n)}{u_*^2} = \frac{17\,f}{(1+9.5\,f)^{5/3}} \tag{3}$$

$$\frac{nS_w(n)}{u_*^2} = \frac{2\,f}{1+5.3\,f^{5/3}} \tag{4}$$

where u_* is the friction velocity, f is the dimensionless frequency (nz/U), U is the mean horizontal wind velocity and n is frequency. The above spectra represent $S_M(n)$ component in the Højstrup model and the addition of low frequency part $S_L(n)$ will complete the Højstrup spectral equations. The Højstrup model can then be written as [6]:

$$\frac{nS_u(n)}{u_*^2} = \frac{0.5\,f_i}{1+2.2\,f_i^{5/3}}\left(\frac{z_i}{-L}\right)^{2/3} + \frac{105\,f}{(1+33\,f)^{5/3}} \tag{5}$$

$$\frac{nS_v(n)}{u_*^2} = \frac{0.32\,f_i}{1+1.1\,f_i^{5/3}}\left(\frac{z_i}{-L}\right)^{2/3} + \frac{17\,f}{(1+9.5\,f)^{5/3}} \tag{6}$$

$$\frac{nS_w(n)}{u_*^2} = \frac{32\,f}{(1+17\,f)^{5/3}}\left(\frac{z}{-L}\right)^{2/3} + \frac{2\,f}{1+5.3\,f^{5/3}} \tag{7}$$

where $f_i = nz_i/U$ and z_i is the lowest inversion height. S_w in Equation (7) is expressed in terms of f and not f_i since the velocity fluctuations of the w-component is limited by the presence of the solid surface, hence it does not scale with z_i and f_i [6]. When parameter L approaches infinity, then Equation (5) to (7) are reduced to the Kaimal spectra in (2) to (4), describing neutral atmospheric conditions. In this study, the u_* value is approximated with u_{*0} according to Højstrup [11] and formulated as:

$$u_* = u_{*0}\left(1 - \frac{z}{z_i}\right) \tag{8}$$

As can be seen from (5) to (7), parameters affecting the Højstrup model include z, z_i, L, and u_*. Since height (z) is a physical measure and not a representative of meteorological condition, we will neglect the presence of z. Instead, we refer to a stability parameter z/L which indirectly represents parameter L. The lowest inversion height z_i represents the height of the boundary layer, which is influenced by atmospheric stability conditions. From stable to unstable conditions, z_i increases as shown in [4], where they found from measurements at an offshore site (FINO1) that z_i varies from approximately 700 m for unstable, 431 m for neutral, and drops to 104 m for stable conditions. Likewise, Obukhov length L represents the effect of shear friction to buoyancy ratio towards the vertical air movement and characterises the turbulence in the surface layer [12]. The sign of L depends on the temperature gradient. In the case of stable conditions, the temperature gradient is positive and results in positive L. The opposite is true for unstable conditions where the temperature gradient is negative.

Table 1. Parametric study of the Højstrup model

z_i (m)	L (m)	TI_u (%) at z = 90 m	TI_u (%) at z = 167.5 m
		1.02	1.00
		3.05	3.01
		6.10	6.01
1000	-100	**8.13**	**8.02**
		12.20	12.02
		18.30	18.03
		24.40	24.05
300		5.56	5.46
500		6.30	6.19
700		6.80	6.69
900	-100	7.73	7.61
1000		**8.13**	**8.02**
1500		8.85	8.73
2000		9.35	9.23
	-1500	6.69	6.50
	-1000	6.78	6.58
	-700	6.89	6.68
1000	-400	7.12	6.91
	-100	**8.13**	**8.02**
	-50	9.01	8.97
	∞	6.36	6.15

To understand the effect of each parameter in the Højstrup model, a parametric study was conducted with z_i = 1000 m, and L = -100 m used as a benchmark. A reference mean wind speed U = 11.4 ms^{-1} was set at the height z = 90 m (these values were selected as they represent the rated wind speed and hub height of wind turbine used in this study). Table 1 summarises the parametric study and the simulated results of the u wind component turbulence intensity (TI). It can be seen from Table 1 that variations in z_i and L resulted in TI_u in the range of 5% to 9% and 6% to 9% respectively.

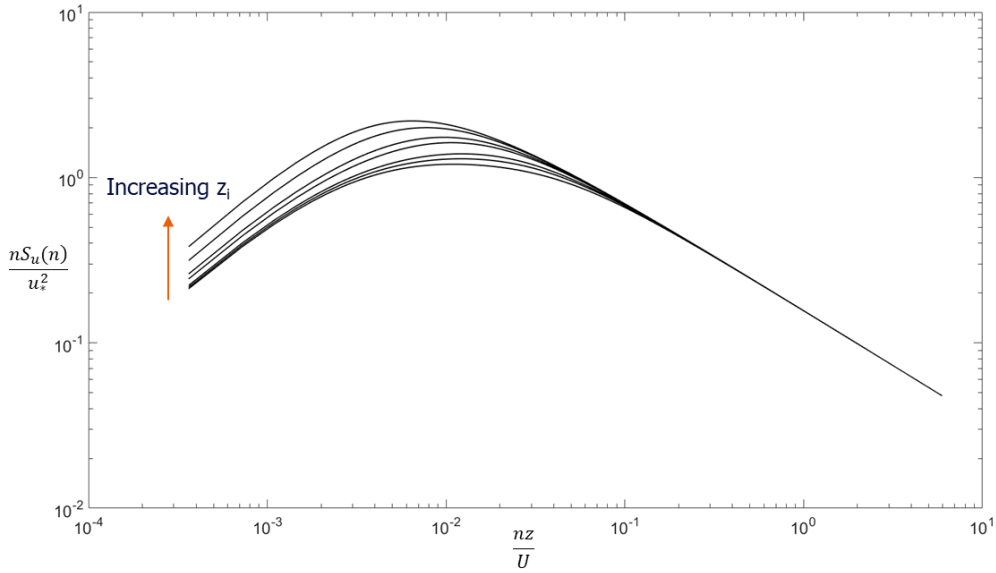

Figure 1. Spectra of u-component at z = 90 m for various z_i.

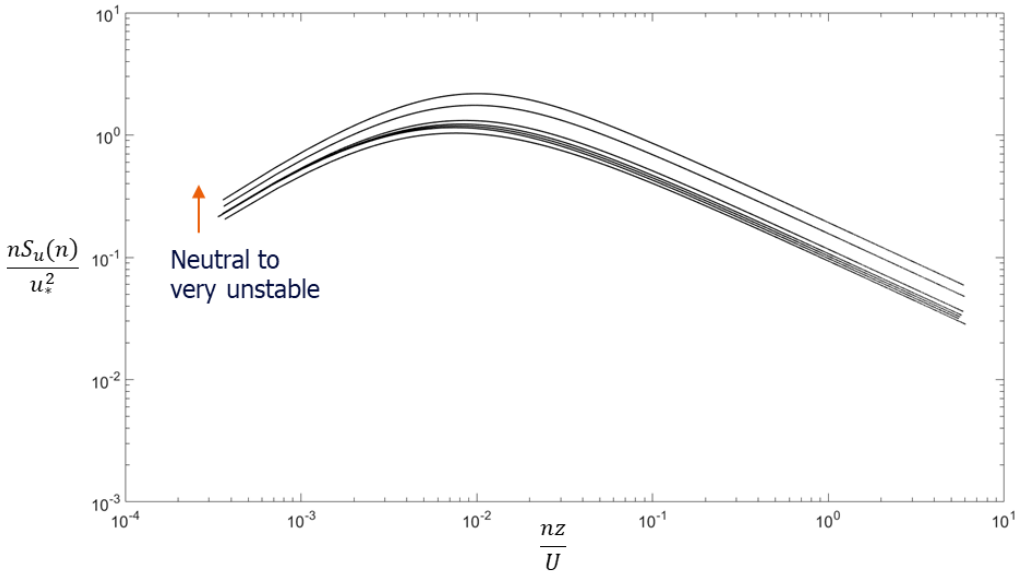

Figure 2. Spectra of u-component at z = 90 m for various L.

We observed that both inversion height z_i and Obukhov length L play an important role in the energy content of the Højstrup model. The increase in z_i on the Højstrup model resulted in increasing energy for u-wind components as presented in Figure 1, especially at low frequencies f (<0.05 Hz). At f>0.1Hz the influence of z_i diminishes and all converge to -2/3 line. This behaviour was also observed for v and w-components. The influence of z_i on the Højstrup model implies that higher z_i results in more energy only at lower frequencies.

Figure 2 shows the target spectra of the u-component comparing various L values at z = 90 m. As the stability goes from neutral to very unstable (from $L = \infty$ to L = -50 m), the u-spectra shifts up, indicating higher energy content as the atmospheric conditions becomes unstable. Unlike z_i, where its influence on the spectral content diminishes at higher frequencies, the higher energy content with variation in L was observed for all reduced frequencies.

3. Methodology

The simulations for this study were based on the spar-buoy type FOWT from Phase IV of the Offshore Code Comparison Collaboration (OC3) project [5]. This phase uses the 5 MW standard wind turbine of the National Renewable Energy Laboratory (NREL) with some changes in the support and control system, in conjunction with the spar-buoy concept 'Hywind' developed by Equinor [5]. The OC3-Hywind properties are summarised in Table 2.

Table 2. OC3-Hywind specifications.

Parameter	
Rotor configuration	3 bladed
Rotor diameter	126 m
Hub height	90 m (above sea level)
Cut-in, rated, cut-out wind speed	3, 11.4, 25 ms^{-1}
Cut-in, rated rotor speed	6.9 rpm, 12.1 rpm
Water depth	320 m
Draft	120 m
Mooring line	3 lines, 120^o apart from each other

3.1. Turbulent wind field simulations

Turbulent wind fields are required for structural simulations input and thus were generated prior to the simulations. The turbulent wind field is represented as a turbulence box with the size of 32768 x 32 x 32 nodes, respectively for along wind, cross wind, and vertical wind direction. A MATLAB model developed by Cheynet [8] was used to simulate the turbulent wind field. The number of nodes in the along wind direction represents the number of steps in the wind simulation. The Højstrup spectra S_u, S_v, and S_w were determined at each turbulence box node and Davenport coherence was used to compute the coherence at each frequency step. Similarly, the Kaimal spectra S_u, S_v, and S_w were determined at each turbulence box node along with Davenport coherence for coherence computation at each frequency step. The decay coefficients used in the Davenport coherence are given in Table 3 and were used for all load cases. According to the study by Cheynet et. al [13] who studied measured offshore wind data from the FINO 1 platform, these decay coefficients vary with stability conditions such that the co-coherence increases with progressively more unstable conditions. Therefore, the use of constant decay coefficients for different load cases given in Table 4 is an approximation, and thus is a limitation in this present study.

A random phase was then applied to the spectra at each node and each frequency step and finally Inverse Fast Fourier Transform (IFFT) was used to get the fluctuating wind speeds. The corrected

logarithmic wind profile from the DNV standards [14] was selected to represent the mean wind profile in our simulations. Accounting for the influence of atmospheric stability conditions, the mean wind velocity at a particular height is defined as [14]:

$$U(z) = \frac{u_*}{\kappa}\left[\ln\left(\frac{z}{z_0}\right) - \psi\right] \tag{9}$$

where κ is a constant (0.4) and ψ depends on the value of L, where for unstable conditions $L < 0$ [14]:

$$\psi = 2\ln(1+x) + \ln(1+x^2) - 2\,\mathrm{atan}(x) \tag{10}$$

in which $x = (1 - 19.3z/L)^{1/4}$. For neutral conditions ($L = \infty$), $\psi = 0$ and this was used for Kaimal model.

Six different random seeds were used for each load case to allow for the simulations to closely resemble the stochastic nature of wind and to reduce uncertainty in the simulations. The sampling frequency used in the simulations was approximately 9.1 s, corresponding to 3600 s simulations with the aforementioned time steps. A value of surface roughness of z_0 of 0.00014 m, was used based on measurements from [15] at the Høvsøre site, and u_{*0} of 0.4 ms^{-1} were used and kept constant in the simulations. The mean wind profile is computed by setting reference wind speed at the hub height U_{hub}. By utilising Eq. 9, the wind speed at height z relative to the hub height z_{hub} is calculated as:

$$U(z) = \frac{\left[\ln\left(\frac{z}{z_0}\right) - \psi\right]}{\left[\ln\left(\frac{z_{hub}}{z_0}\right) - \psi_{hub}\right]} U_{hub} \tag{11}$$

The load cases performed in this study are given in Table 4. Each load case was run for three different mean wind speeds: 8, 11.4, and 15 ms^{-1}, corresponding to below rated, rated, and above rated wind speed respectively.

Table 3. Decay coefficient used for Davenport Coherence Model.

Coefficient	C_u^y	C_v^y	C_w^y	C_u^z	C_v^z	C_w^z
Value	7	7	6.5	10	10	3

Table 4. Load cases.

Spectral model	z_i (m)	L (m)	Stability condition
Højstrup	700	-50	Very unstable
		-90	Unstable
		-180	Slightly unstable
	1000	-50	Very unstable
		-90	Unstable
		-180	Slightly unstable
Kaimal	700	∞	Neutral
	1000	∞	Neutral

3.2. Coupled SIMO-RIFLEX

SIMO-RIFLEX is a coupled simulation tool available in the Simulation Workbench for Marine Application (SIMA), which was developed by MARINTEK. SIMO is able to model flexible multibody systems and perform non-linear time domain simulation of surface vessels subjected to combined wind, wave, and current forces [16]. RIFLEX is a tool especially designed for analysis of slender marine structures with a finite element method that is able to handle unlimited displacements and rotations [10].

Within RIFLEX, there is an extension to include aerodynamic forces on elastic structural members (i.e. blades) using Blade Element Momentum (BEM) theory and control systems for blade pitch and electrical torque [10]. The coupled tools were necessary since the OC3-Hywind is a multibody surface vessel with slender elements.

The generated turbulent wind fields are stored in binary format and used as an input to the coupled SIMO-RIFLEX simulations. In addition to the wind loads described in subsection 3.1, wave loads were also included in our simulations. For all load cases given in Table 4, JONSWAP irregular waves with a peak parameter γ = 3.3, significant wave height H_S = 6 m, and peak period T_p = 12 s were defined. The SIMO-RIFLEX simulations used a 3600 s duration for each load case and each seed, with 0.02 s time step.

4. Results and discussion

In order to understand the simulation results better, results are presented under three different subsections: the simulated wind field characteristics, the fatigue loads of OC3-Hywind components, as well as the motion responses.

4.1. Simulated turbulent wind field

From section 2 we note that theoretically in the Højstrup model, parameters L and z_i affect both spectral energy and TI in a way that when the atmosphere becomes progressively more unstable, spectral energy and TI are increasing. A theoretical comparison between the Højstrup and Kaimal model shows that the Kaimal model has lower spectral energy (Figure 2) and TI (Table 1) than Højstrup model. This implies that neutral conditions produce lower levels of turbulence than unstable conditions. Figure 3 presents the TI from the turbulence box at height z = 92.5 m, and compares all load cases at different wind speeds. The turbulence box follows a sampling frequency of 9.1 Hz for a 1-hour average. The TI shown in Figure 3 are averaged from the six seeds for each case.

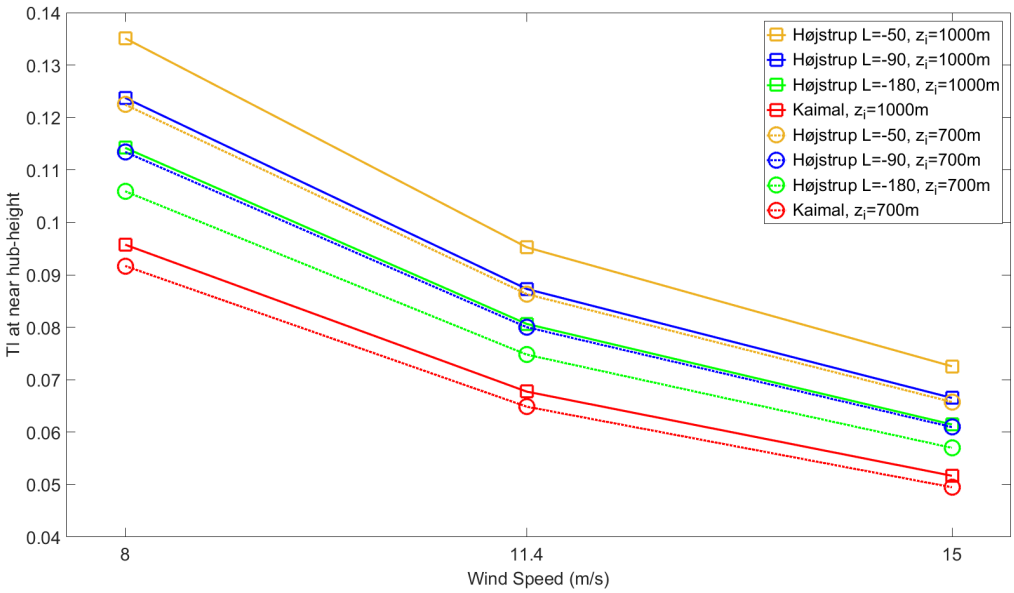

Figure 3. TI at z = 92.5 m from the simulations. Solid line for z_i = 1000 m, dotted line for z_i = 700 m.

In general, it is observed that TI is decreasing with increasing wind speed (Figure 3). We also noted that TI was decreasing with height. As shown in Figure 3, Højstrup with L = -50 m generated the highest TI followed by Højstrup with L = -90 m, L = -180 m and Kaimal respectively by considering the same z_i.

Comparing different z_i, it is clear that higher z_i results in higher TI, even though the effect of z_i on TI is not as pronounced as the effect of L (Figure 3). Variation in z_i gives approximately 14% difference between the maximum and minimum TI, while variation in L gives 40% difference between the maximum and minimum TI (Figure 3). This effect of z_i was also noted for the Kaimal model despite z_i not being an input parameter in the model (Figure 3) but is included via the u_* value in Eq. 8 which incorporates z_i.

4.2. Damage equivalent loads

Fatigue loads of the OC3-Hywind turbine components are measured in the form of damage equivalent load (DEL). Rainflow counting method [17] was used as the stress range filter. To quantify the DEL from load time series, the relation between the occurring stress and its number of cycle is required. This relation is commonly known as S-N curve and is usually obtained by experiments for different materials. In the absence of a S-N curve, the number of cycles N_i resulting in failure at a specific stress S_i can be determined with $N_i = S_0^m S_i^{-m}$, where S_0 is the highest stress in the time series and m is the Wöhler exponent. Normally, a quantified equivalent damage S_{eq} for a given number of cycles n_{eq} is considered to make an easier interpretation of the accumulated loads $D_{total} = n_{eq}\, S_{eq}^m$. By substituting $D_{total} = \sum n_i S_i^m$, the damage equivalent load is calculated as [18]:

$$S_{eq} = \left(\frac{\sum n_i S_i^m}{n_{eq}} \right)^{1/m} \tag{12}$$

where n_i is the number of cycle occurrences for the considered load range class, obtained from rainflow counting along with S_i. In the calculation, the value of n_{eq} = 10^7, m = 3 for tower and mooring line components (steel material), and m = 12 for blade (fiberglass material) were selected. DEL of the OC3-Hywind turbine were computed for the following wind turbine load components: tower base fore-aft bending, tower base side-side bending, tower top torsion, blade root flap-wise bending, blade root edge-wise bending, and mooring lines tension. DEL results are presented in the normalised form relative to the load case of Kaimal z_i = 1000 at 8 ms^{-1}. The normalised DEL shown in Figure 4 to Figure 6 are the averaged values from all six seeds.

We note that in general, the Højstrup model with L = -50 m resulted in the highest DEL followed by Højstrup with L = -90 m, L = -180 m and finally Kaimal by comparing the same z_i. This was observed for each of the aforementioned load components, except for the mooring lines tension where no clear pattern was seen. Below rated wind speed (8 ms^{-1}) very unstable conditions (L = -50 m) resulted in higher DEL for both values of z_i. At rated wind speed and above (11.4 ms^{-1} and 15 ms^{-1}), exceptions were noted for the tower base fore-aft bending and the blade root flap-wise DEL's (Figure 6), which showed no obvious trends. When comparing different z_i, generally higher z_i resulted in higher DEL's with the Kaimal model and z_i = 700 giving the lowest DEL's, compared to other load cases.

As presented in Figure 4, the largest DEL variation between load cases was observed for the tower top torsion with 65% difference between the minimum and the maximum values. The second largest DEL variation with 37% difference between the minimum and the maximum values was observed for the tower base side-side bending as shown in Figure 5. On the other hand, the least DEL's variation was noted for blade root edge-wise bending with only 3% difference between the minimum and the maximum values. A small DEL's variation of 7% was also observed for the tower base fore-aft. Mooring line 3 tension DEL's varied by 25% when comparing minimum and the maximum values, which is the highest variation amongst the three lines. Our simulations also resulted in a 24% difference between the minimum and the maximum values for the blade root flap-wise bending DEL's.

In respect to variation in wind speed, normally the DEL increases with wind speed as shown in Figure 4 for the tower top torsion DEL's. The increase of the DEL with wind speed was also observed for other load components, except for tower base side-side bending DEL's which seemed to decrease with wind speed (Figure 5). Meanwhile, mooring lines tension DEL's showed no specific pattern with wind speed.

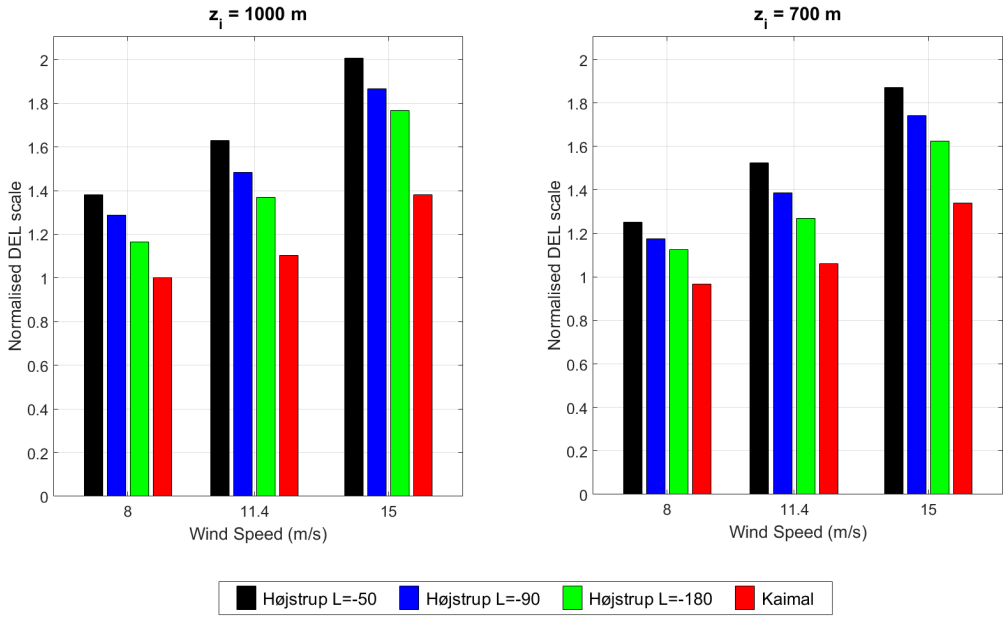

Figure 4. Normalised DEL for tower top torsion (normalized by the load case of Kaimal at 8 ms^{-1}). Left figure shows the results for z_i = 1000 m and the right hand figure for z_i = 700 m.

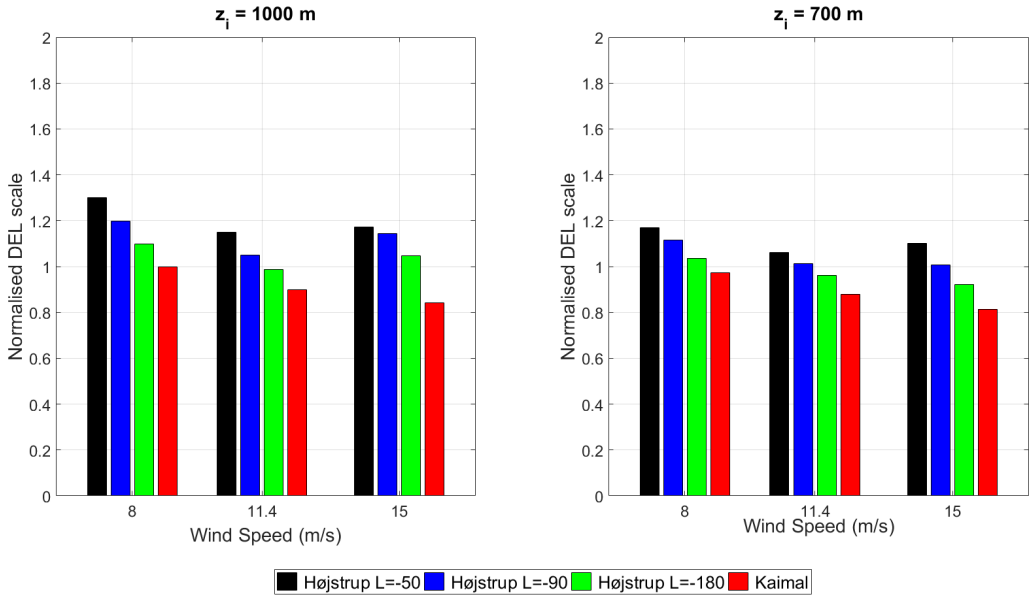

Figure 5. Normalised DEL for tower base side-side bending (normalized by the load case of Kaimal at 8 ms^{-1}). Left figure shows the results for z_i = 1000 m and the right hand figure for z_i = 700 m.

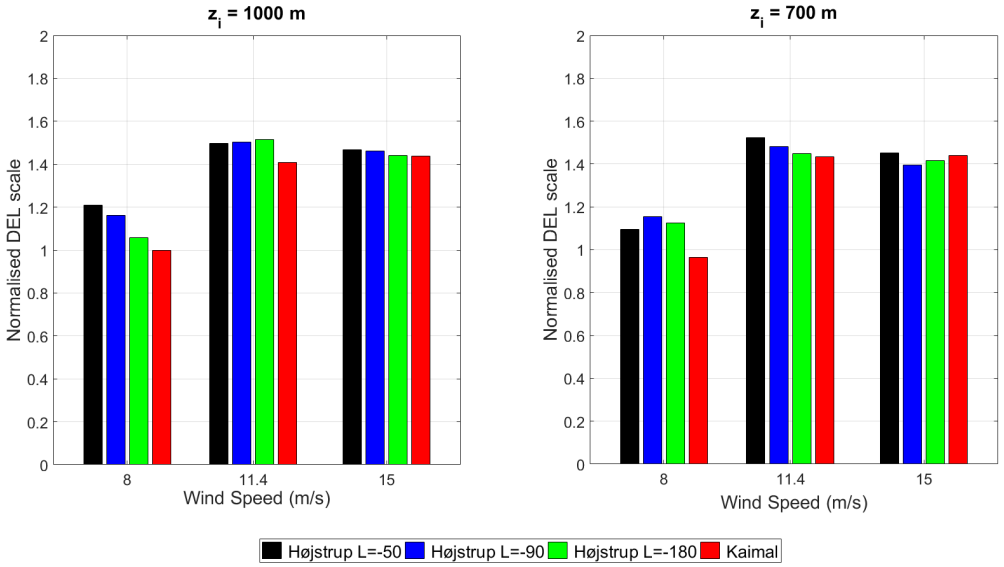

Figure 6. Normalised DEL for blade root flap-wise bending (normalized by the load case of Kaimal at 8 ms^{-1}). Left figure shows the results for z_i = 1000 m and the right hand figure for z_i = 700 m.

Figure 7 shows the spectral density plot of tower top torsion comparing neutral to very unstable stability conditions for U = 11.4 ms^{-1} and z_i = 1000 m. It can be seen that the highest spectral energy is found for Højstrup with L = -50 m, followed by Højstrup L = -90 m, Højstrup L = -180 m, and Kaimal, observed for all frequencies except at 0.2 Hz. The tower top torsion is excited by waves at frequency f = 0.083Hz, blade 1P (f = 0.2 Hz) and blade 3P (f = 0.6 Hz). The same was observed for all other wind speeds. When comparing the same results for z_i = 1000 m and z_i = 700 m, in general a similar trend was observed except at f = 0.2 Hz where Højstrup with L = -50 m produced the highest spectral energy. The boundary layer height of z_i = 700 m was also observed to result in lower energy spectra when compared to the results for z_i = 1000 m for all Højstrup cases.

The spectral energy density plots for the tower base side-side bending also showed that the highest spectral energy was found under very unstable conditions (Højstrup with L = -50 m) similar to the tower top torsion. Particularly at frequencies f < 0.15 Hz and f > 0.45 Hz whereas at 0.15 Hz < f < 0.45 Hz, the variation between the load cases was quite small. The highest spectral peak is found for f ~ 0.5 Hz which corresponds to the tower base side-side bending natural frequency. Similarly, this trend was observed for other wind speeds except that at 8 ms^{-1}, where the magnitude of the spectral energy is notably higher particularly near the natural frequency of the tower base side-side mode. Comparing z_i=1000 m and z_i= 700 m, in general a similar trend was observed and lower z_i was observed to result in lower energy spectra for all Højstrup cases.

The spectral energy of the blade root flap-wise bending shows that this mode was excited by the wave frequencies, blade 1P, 2P, and 3P at all considered wind speeds. At frequencies lower than 1P, the spectral energy showed no notable variation with different stability conditions. At frequencies higher than 1P, one can note that generally Højstrup with L = -50 m resulted in the highest spectral energy followed by Højstrup L = -90 m, Højstrup L = -180 m, and Kaimal. However, in the peak of 1P, 2P, and 3P spectral energy of Kaimal case overlapped with Højstrup with L = -50 m especially at rated wind speed and above. A similar trend was noted for the z_i = 700 m, except it produced lower energy spectra than when z_i = 1000 m for all Højstrup load cases.

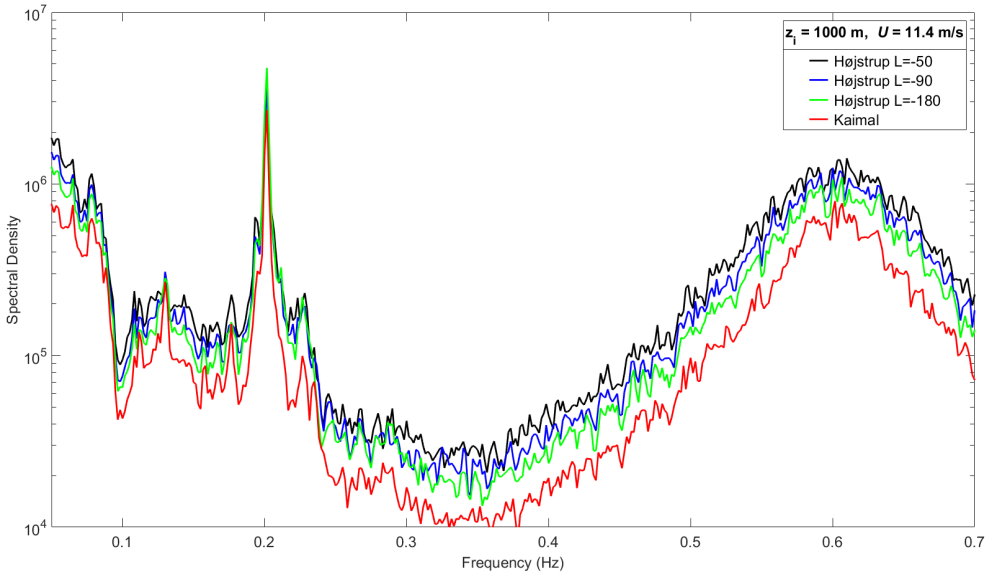

Figure 7. Spectral density plot of tower top torsion for U = 11.4 ms^{-1} at z_i = 1000 m.

4.3. Platform motions

Aside from fatigue damage (DEL's), it is also important to evaluate the motions in six DOF experienced by the OC3-Hywind. Our simulations showed that the roll, sway and yaw platform motions exhibited notable differences between the load cases as opposed to pitch, surge and heave. In this subsection, emphasis is put on platform roll and sway, however, it is important to note that the magnitude of both sway translation and roll motion were very small, within the range of -1 m to 1 m for sway and -0.3° to 0.6° for roll.

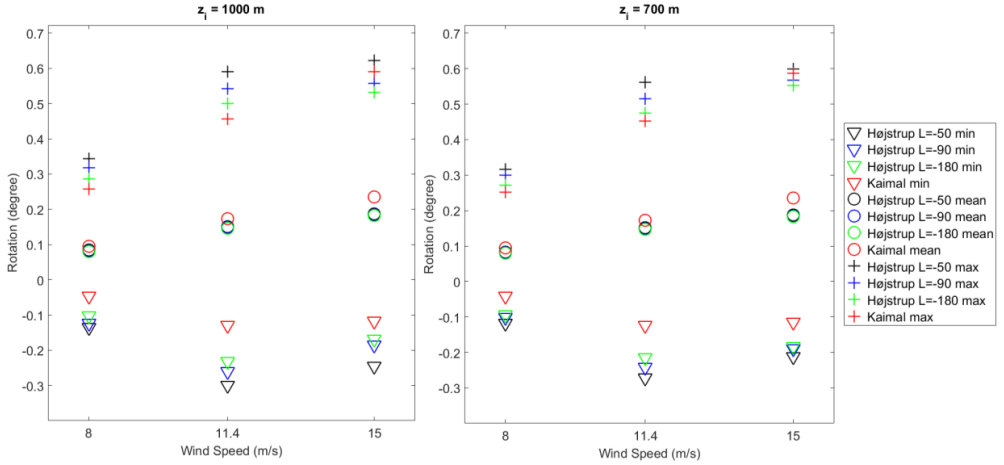

Figure 8. Platform roll rotation (all load case). Left figure z_i = 1000 m, right figure for z_i = 700 m.

Figure 8 presents platform roll of the OC3-Hywind comparing all load cases. It can be seen from this figure that generally Højstrup with L = -50 m resulted in the highest roll followed by Højstrup L=-90 m, L= -180 m and finally Kaimal. Comparing the left and right plots in Figure 8, the influence of z_i on platform roll motion was not notable since the overall platform roll distribution is relatively similar for both boundary layer heights.

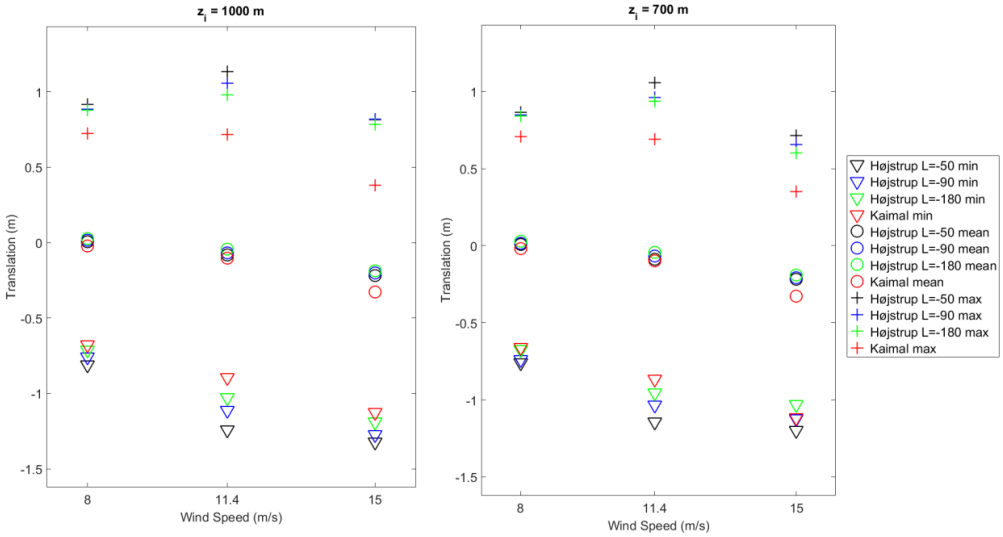

Figure 9. Platform sway translation (all load case). Left figure z_i= 1000 m, right figure for z_i= 700 m.

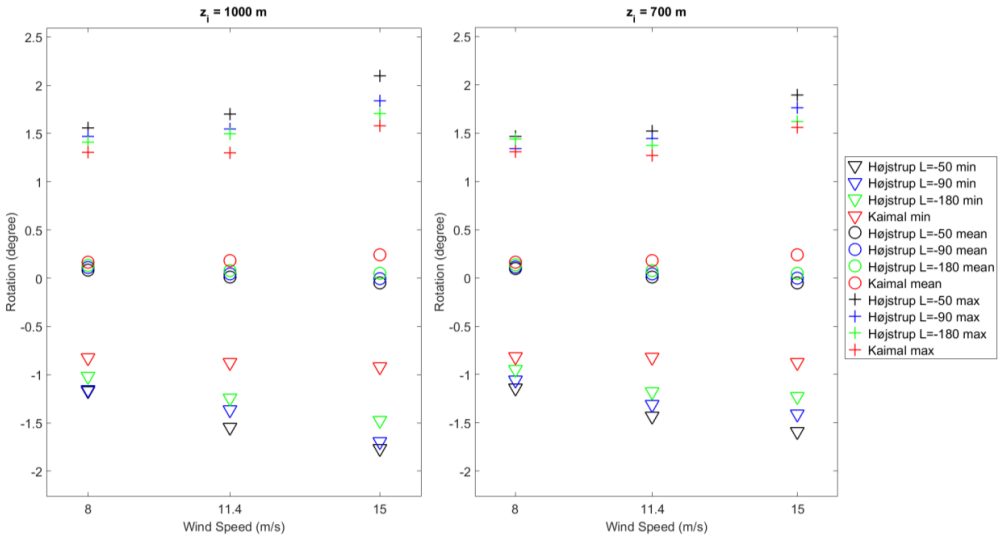

Figure 10. Platform yaw rotation (all load case). Left figure z_i = 1000 m, right figure for z_i = 700 m.

The platform sway response comparing all load cases is shown in Figure 9. As seen from this figure, one can observe a similar trend with the platform roll response where generally the highest sway was

found under Højstrup with L = -50 m, followed by Højstrup with L = -90 m, L = -180 m and Kaimal respectively. Likewise for roll motion, the influence of z_i on platform sway was not notable.

Platform yaw response comparing all load cases can be seen in Figure 10. This figure shows that Højstrup with L= -50 m generally yielded the highest platform yaw followed by Højstrup L = -90 m, L = -180 m and finally Kaimal. The effect of z_i on platform yaw was also not clearly observed.
In terms of spectral energy, platform roll, sway, and yaw motions were excited by the waves and generally, Højstrup with L = -50 m gave the highest spectral energy for roll, sway, and yaw followed by Højstrup with L = -90 m, L = -180 m and Kaimal. The highest spectral peak for platform roll was noted at the platform's roll natural frequency f ~ 0.034 Hz for all load cases. The same was observed for sway where the platform's sway natural frequency at f ~ 0.0073 Hz had the highest spectral peak for all load cases. For yaw motion, the highest spectral peak was found at low frequency f ~ 0.005 Hz, which might be the excitation from the low frequency content in the Højstrup spectral wind model for all unstable load cases. Comparing z_i = 1000 m and z_i = 700 m, higher z_i generally resulted in higher spectral energy for platform roll, sway, and yaw.

4.4. Discussion

The parameters L and z_i seem to affect the generated TI, where TI is increasing with z_i and with L as z/L<0 gets closer to zero. This is in agreement with the sensitivity study performed in section 2. The influence of the parameters L and z_i on the generated TI can also be related to the DEL's and platform motion responses, such that higher TI results in higher DEL's and platform motion, when considering the same wind speed.

When comparing the Højstrup and Kaimal wind models, one can see that the addition of lower spectral frequency components to represent unstable atmospheric conditions has resulted in higher energy spectra for u, v, and w wind components. This addition also produces higher TI as well as DEL's and platform motions of the OC3-Hywind turbine. Based on this argument, we are able to simulate the effect of enhanced turbulence levels under unstable atmospheric stability unlike previous studies which have used for example the Mann spectral tensor model fitted to measurements under unstable atmospheric conditions [16]. Having said the above, exclusions were applicable to the following components:

- Mooring lines tension DEL has no clear trends for progressively unstable conditions or even increasing wind speed
- Despite the finding that platform pitch motion did not vary much with load case variation, it is worth mentioning that the OC3-Hywind platform was found to be dominated by pitching backwards (the platform pitched in the range of -2^o to +8^o). This platform pitch response might be due to the influence of the blade-pitching activity [19]
- Platform pitch, heave, and surge motions seemed to be 'invariant' with load case variation for the OC3 Hywind turbine, probably due to these DOF being heavily influenced by the wave excitation. We noted that the spectral plots of these DOF were very similar for all load cases, especially near the peak wave frequency.

Lastly, although z_i is not an input parameter to Kaimal Model, the influence of z_i on the generated TI and DEL is probably due to the use of an approximated u_*value, given in equation 8, which involves z_i.

5. Conclusion

From this study, the importance of unstable atmospheric stability on the loads and motion responses of the OC3-Hywind turbine is highlighted. By using the Højstrup model to account for enhanced energy at low frequencies under unstable conditions, the DEL of tower top torsion is estimated to be 65% higher than in neutral conditions using the Kaimal model, similarly for the tower base side-side bending DEL which was 37% higher. It was also found that the use of an appropriate wind model for unstable

conditions can produce up to 40% higher TI compared to neutral conditions. It is therefore necessary to account for unstable conditions in the design of FOWTs, as unstable conditions are prominent in an offshore environment [4] [13]. It is therefore important to develop and validate a turbulent wind model suitable for unstable conditions in the offshore marine boundary layer, to reduce the uncertainty in the design of large floating offshore wind turbines.

Acknowledgments
Authors would like to express their gratitude to Dr. Etienne Cheynet, for the assistance, knowledge, support, and time spent to help in the completion of this article.

References

[1] C. Dyrbye and S. O. Hansen, Wind Loads in Structure, West Sussex, England: John Wiley & Sons Ltd, 1997.

[2] International Electrotechnical Commission, "Wind Turbines – Part 1 Design Requirements," International Electrotechnical Commission (IEC), Geneva, Switzerland, 2005.

[3] J. Mann, "The Spatial Structure of Neutral Atmospheric Surface-layer Turbulence," *Journal of Fluid Mechanics 273,* pp. 141 - 168, 1994.

[4] O. Krogsæter and J. Reuder, "Validation of Boundary Layer Parameterization Schemes in the Weather Research and Forecasting (WRF) Model under the Aspect of Offshore Wind Energy Applications-Part II: Boundary Layer Height and Atmospheric Stability," *Wind Energy 18(7),* pp. 1291 - 1302, 2014.

[5] J. Jonkman, "Definition of the Floating System for Phase IV of OC3," National Renewable Energy Laboratory (NREL), Golden, CO, USA, 2010.

[6] J. Højstrup, "A Simple Model for the Adjustment of Velocity Spectra in Unstable Conditions Downstream of an Abrupt Change in Roughness and Heat Flux," *Boundary-Layer Meteorology 21,* pp. 341 - 356, 1981.

[7] J. C. Kaimal, J. C. Wyngaard, Y. Izumi and O. R. Coté, "Spectral Characteristics of Surface-layer Turbulence," *Quarterly Journal of the Royal Meteorological Society, 98(417),* pp. 563 - 589, 1972.

[8] E. Cheynet, "Wind Field Simulation," MathWorks, 2018.

[9] A. G. Davenport, "The Spectrum of Horizontal Gustiness Near the Ground in High Winds," *Quarterly Journal of the Royal Meteorological Society 83(372),* pp. 194 - 211, 1961.

[10] H. Ormberg and E. Bachynski, "Global Analysis of Floating Wind Turbines: Code Development, Model Sensitivity and Benchmark Study," *Twenty-second International Offshore and Ploar Engineering Conference,* 17-22 June 2012.

[11] J. Højstrup, "Velocity Spectra in the Unstable Planetary Boundary Layer," *Journal of the Atmospheric Sciences 39(10), ,* pp. 2239 - 2248, 1982.

[12] A. Monin and A. Obukhov, "Basic Laws of Turbulent Mixing in the Surface Layer of the Atmosphere," *Contrib. Geophys. Inst. Acad. Sci. 24(151),* pp. 163 - 187, 1954.

[13] E. Cheynet, J. B. Jakobsen and J. Reuder, "Velocity Spectra and Coherence Estimates in the Marine Atmospheric Boundary Layer," *Boundary-Layer Meteorology 169(3),* pp. 429 - 460, 2018.

[14] Det Norske Veritas AS, "Environmental Conditions and Environmental Loads (DNV-RP-C205)," Oslo, 2014.

[15] A. Sathe, J. Mann, T. Barlas, W. A. A. M. Bierbooms and G. J. W. van Bussel, "Influence of Atmospheric Stability on Wind Turbine Loads," *Wind Energy 16(7),* pp. 1013 - 1032, 2013.

[16] MARINTEK, 2009. [Online]. Available: http://www.ivt.ntnu.no/imt/courses/tmr4225/lectures/2009/Lecture%20Notes_Finn%20G%20Nielsen/2009-03-17_Simo%20and%20Mathiue/SIMO_general_PCS.pdf. [Accessed December 2018].

[17] M. Matsuishi and T. Endo, "Fatigue of Metals Subjected to Varying Stress," *Japan Society of Mechanical Engineers, Fukuoka, Japan, 68(2),* pp. 37-40, 1968.

[18] DTU Wind Energy, "DTU Itslearning," [Online]. Available: https://windenergy.itslearning.com/ContentArea/ContentArea.aspx?LocationID=29&LocationType=1. [Accessed 2016].

[19] M. Hall, B. Buckham and C. Crawfor, "Evaluating the Importance of Mooring Line Model Fidelity in Floating Offshore Wind Turbine Simulations," *Wind Energy 17(12),* pp. 1835 - 1853, 2014.

[20] A. Sathe, S. E. Gryning and A. Peña, "Comparison of the Atmospheric Stability and Wind Profiles at Two Wind Farm Sites Over a Long Marine Fetch in the North Sea," *Wind Energy 14(6),* pp. 767-780, 2011.

Paper 2
Numerical analysis of the effect of offshore turbulent wind inflow on the response of a spar wind turbine

*Rieska Mawarni Putri[1], Charlotte Obhrai[1], Jasna Bogunovic Jakobsen[1], and Muk Chen Ong[1]
[1]Department of Mechanical and Structural Engineering and Materials Science, University of Stavanger, Norway

energies

MDPI

Article

Numerical Analysis of the Effect of Offshore Turbulent Wind Inflow on the Response of a Spar Wind Turbine

Rieska Mawarni Putri *, Charlotte Obhrai, Jasna Bogunovic Jakobsen and Muk Chen Ong

Department of Mechanical and Structural Engineering and Material Science, University of Stavanger, 4036 Stavanger, Norway; charlotte.obhrai@uis.no (C.O.); jasna.b.jakobsen@uis.no (J.B.J.); muk.c.ong@uis.no (M.C.O.)

* Correspondence: rieska.m.putri@uis.no

Received: 30 January 2020; Accepted: 9 May 2020; Published: 15 May 2020

Abstract: Turbulent wind at offshore sites is known as the main cause for fatigue on offshore wind turbine components. Numerical simulations are commonly used to predict the loads and motions of floating offshore wind turbines; however, the definition of representative wind input conditions is necessary. In this study, the load and motion responses of a spar-type Offshore Code Comparison Collaboration (OC3) wind turbine under different turbulent wind conditions is studied and investigated by using SIMO-Riflex in Simulation Workbench for Marine Applications (SIMA) workbench. Using the two spectral models given in the International Electrotechnical Commission (IEC) standards, it is found that a lower wind lateral coherence under neutral atmospheric stability conditions results in an up to 27% higher tower base side–side bending moment and a 20% higher tower top torsional moment. Comparing different atmospheric stability conditions simulated using a spectral model based on FINO1 wind data measurement, the highest turbulent energy content under very unstable conditions yields a 26% higher tower base side–side bending moment and a 27% higher tower top torsional moment than neutral conditions, which have the lowest turbulent energy content and turbulent intensity. The yaw-mode of the OC3 wind turbine is found to be the most influenced component by assessing variations in both the lateral coherence and the atmospheric stability conditions.

Keywords: turbulent wind; atmospheric stability; wind coherence; Offshore Code Comparison Collaboration (OC3); turbulent wind model

1. Introduction

The design phase of a wind turbine is considered as one of the most critical steps in wind farm planning. Many research studies rely on numerical simulations to predict and check the reliability of the wind turbine structures, especially those located offshore. For this reason, a justifiable environmental input must be chosen carefully, and reliable measurement data should be used whenever available. In the absence of reliable measurement data, the International Electrotechnical Commission (IEC) 61400-1, 2005 [1], is often used as the wind turbine design guideline. In this standard, two turbulent wind models are recommended for wind turbine design: Kaimal Spectra and Exponential Coherence and Mann Spectral Tensor Model. Herein, the Kaimal Spectra and Exponential Coherence is referred to as the Kaimal model and the Mann Spectral Tensor Model is referred to as the Mann spectral model. Both the Kaimal model [2] and the Mann spectral model [3] were derived from measured wind data under neutral atmospheric conditions. In the IEC 61400-1, the two models are prescribed to have equal energy content but have significant differences in terms of spatial coherence. Eliassen and Obhrai [4]

attempted to compare the vertical coherence between the Kaimal model and the Mann spectral model with measured wind data at the FINO1 platform [5]. It was shown that the observed lateral coherence at 40 m separation from FINO1 is over-predicted using the Kaimal model but under-predicted using the Mann spectral model [4].

The study by Godvik [6] shows that a 6 MW spar wind turbine's platform yaw motion is sensitive to wind coherence over the rotor area when using the two wind models provided in the IEC 61400-1 standard. The Mann spectral model was found to induce higher yaw motion of the spar wind turbine compared to the Kaimal model [6]. Bachynski and Eliassen [7] investigated the influence of the Kaimal model and the Mann spectral model on the global responses of a semisubmersible, spar, and Tensioned-Leg Platform (TLP) 5 MW wind turbines. The platform yaw responses of the three floater types were found to be higher when simulating the Mann spectral model wind fields than the Kaimal model wind fields [7]. Similarly, Doubrawa et al. [8] found that by generating wind fields using the large eddy simulations (LES) for the two spectral models, the tower base yaw moment of a 6 MW spar wind turbine was predicted higher when using the Mann spectral model than the Kaimal model. Since both spectral models differ in terms of spatial coherence (especially in the lateral separations), it is then suggested [6–8] that the wind spatial coherence under neutral atmospheric stability conditions has a significant influence for the floaters' yaw and the spar's tower base yaw moment. This being said, one should note that the wind spatial coherence varies with atmospheric stability conditions [9], and that offshore, there is a prevalence of unstable conditions [10].

An investigation into the influence of atmospheric stability for the load responses of a bottom-fixed wind turbine was conducted by Sathe et al. [9] using the Mann spectral model. In their study, the measured wind data from Høvsøre site [11] was fitted to the Mann spectral model and they simulated turbulent wind fields using the obtained Mann spectral model parameters from the wind measurement fitting. The fit of the wind measurements at Høvsøre to the Mann spectral model parameters showed an increase of the spatial coherence as the atmospheric stability conditions changed from stable through to unstable conditions [9]. However, it should be noted that the Mann spectral model has not been validated to predict the coherences for non-neutral atmosphere, but it was assumed that the influence of atmospheric stability on the coherences can be depicted using the Mann spectral model [9]. Sathe et al. [9] found that up to 17% load difference (depending on the component of interest) on a bottom-fixed wind turbine is noted when comparing only neutral conditions and various atmospheric stability conditions. To the authors' knowledge, no studies have been conducted yet with respect to analysis of measured spatial coherence of turbulent wind offshore (especially for lateral separations) under different atmospheric stability conditions due to the data availability. However, Cheynet et al. [12] derived an empirical vertical coherence model from wind measurement data at FINO1. The vertical coherences were found to be increasing from stable to neutral and then to unstable atmospheric stability conditions [12], which is in agreement with the observations from the study by Sathe et al. [9]. Yet, in the work of Sathe et al. [9], it is not specifically mentioned whether the increasing coherence from stable to neutral and then to unstable conditions are for lateral separations or vertical separations, or for both.

As the atmospheric stability conditions shift progressively from neutral to unstable conditions, the low-frequency wind energy content increases, and thus higher turbulence intensities are observed under unstable conditions compared to the neutral conditions [12,13]. Putri et al. [14] and Knight and Obhrai [15] have shown the importance of taking into account the non-neutral atmospheric stratification, especially unstable conditions, in terms of wind energy content on the loads and motions' responses of floating wind turbines. When comparing unstable and neutral conditions, higher yaw-mode loads and motions of a spar floating wind turbine under unstable conditions were noted up to 40% [14,15].

The findings of References [6–8,14,15] raise the question of whether a spar wind turbine's load and motion responses are more prone to variations in the wind coherence or to the turbulent wind energy content, as we know that the dominant atmospheric stability at offshore is unstable conditions [10]. Hence, this study aims to perform numerical analysis of different incoming turbulent wind inflow

conditions on a floating spar wind turbine rotor and investigates the spar wind turbine's load and motion responses. The Kaimal model and the Mann spectral model are used to simulate wind fields under neutral conditions with variation in coherence. In addition, the Pointed-Blunt model [12], an empirical model fitted to measured data at FINO1, is used to simulate wind fields under different atmospheric stability conditions, from neutral to very unstable. This model is paired with the IEC exponential coherence [1] in the present study.

2. Theory and Methods

This section gives a brief description of the wind models used to generate the wind fields and its characteristics with respect to the atmospheric stability conditions, as well as the methodology used in the present study.

2.1. Atmospheric Stability and Wind Models

Wind spatial coherence or wind coherence is a measure of how related the wind fluctuations at two points in the wind field are, for a specific separation distance, at different frequencies. The term 'coherence' refers to the normalized wind cross-spectrum. The coherence consists of a real part called the co-coherence and an imaginary part known as the quad-coherence. In a homogeneous turbulent wind field, the magnitude of the quad-coherence is fairly small for the across-flow separations, compared to the co-coherence. Hence, the quad-coherence is considered to be negligible [16]. In the following, the term 'coherence' therefore represents the co-coherence, unless otherwise stated.

Atmospheric stability is one factor which affects spatial and temporal characteristics of wind turbulence [9]. The general classes of atmospheric stability conditions are neutral, stable, and unstable, which depends on the non-dimensional parameter z/L_m (z = height above surface, L_m = Obukhov length) [2]. This parameter is proportional to the temperature flux at the surface $\overline{w'\theta'}$. When $z/L_m < 0$, the temperature flux is positive and causes the vertical rise of air parcels, indicating unstable conditions. This enhanced vertical mixing is often referred to as buoyancy-generated turbulence and occurs only under unstable atmospheric stability conditions [17]. On the other hand, when $z/L_m > 0$, we have stable conditions and a negative temperature flux. Stable conditions are characterized by high wind shear (mean wind profile) and suppression of vertical mixing [17]. Neutral conditions occur when $z/L_m = 0$, and hence, there is no heat exchange between the air parcels and its surroundings [17].

In the present study, different wind inflow conditions are generated by using three different wind models: the Kaimal model [1], the Mann Spectral Tensor model [1], and the Pointed-Blunt model [12]. Both the Kaimal and Mann spectral models are valid only for neutral atmospheric stability conditions, while the Pointed-Blunt model was fitted to wind data from the FINO1 offshore platform with variable atmospheric stability [12]. It is worth noting that the parameters for the Kaimal and Mann spectral models have been adjusted accordingly to meet the standard requirement and have been set to have equal energy spectra [1,18], while the spatial coherences formulation is not equalized.

For the wind models described in Section 2.1.1, Section 2.1.2, Section 2.1.3 the influence of the Coriolis force is not examined, so the directional shear effect is not taken into account. This means that the longitudinal wind component u- has the same direction as the friction velocity u_*.

2.1.1. Kaimal Spectra and Exponential Coherence

First, the Kaimal model is described. The single-sided, non-dimensional velocity spectrum for each wind component S_i is defined as follows [1]:

$$fS_i(f)/\sigma_i^2 = (4fL_i/U_{hub})/(1 + 6fL_i/U_{hub})^{5/3} \quad (1)$$

where:

f: frequency (Hz),
i: velocity component index (1: longitudinal, 2: lateral, and 3: vertical),

S_i: velocity spectrum for each component i,
σ_i: standard deviation of velocity component i (m/s) (Table 1),
L_i: integral length scale of velocity component i (m) (Table 1),
U_{hub}: mean wind speed at hub height (m/s).

Table 1. Parameters for the Kaimal model [1].

	Velocity Component		
	1 (u)	**2 (v)**	**3 (w)**
σ_i	σ_1	0.8 σ_1	0.5 σ_1
L_i	8.1 Λ_1	2.7 Λ_1	0.66 Λ_1

with $\Lambda_1 = 42$ m ($z \geq 60$ m) and z is the hub height in meters. The velocity spectra given in Equation (1) define the single point spectral energy for the three velocity components. The velocity time series at different points in space are computed based on the spatial coherence and a random phase. In this case, the following exponential coherence is associated with Equation (1) and applicable only for u velocity component [1]:

$$Coh_{uu}(f, \Delta) = \exp[-12((f\Delta/U_{hub})^2 + (0.12\Delta/L_u)^2)^{1/2}] \quad (2)$$

where:

Δ: separation distance, either lateral or vertical (m),
L_u: 8.1 Λ_1 (m).

Coherence for the v and w velocity components are not specified in the IEC 61400, and in TurbSim [19], identity coherence is recommended for both vv- and ww- coherences. In the present work, the coherence formulated in Equation (2) is adopted for both vv- and ww- turbulence components, for a more representative coherence in a real wind field than applying the identity coherence. In reality, different coherence functions should be used for each of the three turbulence components, and ideally, taken from the relevant site measurements. For the v- turbulence component, a higher lateral coherence than that for u and w components was observed in the study by Saranyasoontorn et al. [16] based on wind measurements. The wind conditions were measured from the Micon 65/13 wind turbine near Bushland in Texas for a mixture of datasets of different stability conditions [16].

2.1.2. Mann Spectral Tensor

The Mann uniform shear turbulence model was developed in the form of a spectral tensor with isotropic von Karman energy spectrum as its initial condition. The tensor will develop anisotropically over time due to the mean wind shear [3]. The resulting anisotropic tensor is given as [1,3]:

$$\Phi_{ij}(\mathbf{k}) = E(k)/4\pi k^4 (\delta_{ij}k^2 - k_i k_j) \quad (3)$$

with:

i,j: index for different wind component (1: longitudinal, 2: lateral, and 3: vertical),
Φ_{ij}: anisotropic tensor for each component ij,
k: non-dimensional wave number for each component direction (k_1, k_2, k_3),
k: non-dimensional wave number magnitude = $(k_1^2 + k_2^2 + k_3^2)^{1/2}$,
E(k): non-dimensional von Karman isotropic energy spectrum = $1.453k^4/(1 + k^2)^{17/8}$ [1],
δ_{ij}: non-dimensional spatial separation vector components.

The complete tensor matrix of Equation (3) is not shown in detail here but can be found in the IEC 61400-1 [1,18]. The non-dimensional, single-sided velocity component spectrum generated from Equation (3) can be expressed as [1]:

$$fS_i(f)/{\sigma_i}^2 = {\sigma_{iso}}^2/\ {\sigma_i}^2\ (4\pi\ell f/U_{hub})\ \Psi_{ij}(2\pi\ell f/U_{hub}) \quad (4)$$

where:

Ψ_{ij}: wave number autospectrum (i = j)/cross-spectrum (i ≠ j),
${\sigma_i}^2$: component variance (m^2/s^2) (Table 1),
σ_{iso}: 0.55 σ_1,
ℓ: 0.8 Λ_1, where Λ_1 = 42 m for z ≥ 60 m,

while the coherence is given as [1]:

$$Coh_{ij}(f, \Delta_y, \Delta_z) = Real\{\Psi_{ij}(f, \Delta_y, \Delta_z)/[S_i(f)\ S_j(f)]^{1/2}\} \quad (5)$$

with:

Δ_y = separation distance in the lateral direction,
Δ_z = separation distance in the vertical direction.

Although the mathematical definition of the Mann spectral model is rather complex, the Mann spectral model is simply described by three parameters: $\alpha\varepsilon^{2/3}$, ℓ, and γ, which later will be used as input parameters for the simulations in this study. $\alpha\varepsilon^{2/3}$ is a measure of spectral energy in the inertial subrange, ℓ is the length scale (size of the occurring eddy), and γ is the shear parameter (a measure of anisotropy) [3]. A least squares fit of the Kaimal model to Equation (5) results in shear parameter γ = 3.9 [1].

2.1.3. Pointed-Blunt

The Pointed-Blunt model [12] was developed based on two years of FINO1 measurement data (2007–2008) under different atmospheric stability conditions. This model was named after its shape, which includes the low-frequency part (pointed) and the high-frequency part (blunt). The model has four floating parameters dependent of the atmospheric stability conditions within the range of $-2 < \zeta < 2$, where $\zeta = z/L_m$, z is the observed height and L_m is the Obukhov length. The non-dimensional mathematical formulation for this model is [12]:

$$fS_i(f)/{u_*}^2 = {a_1}^i f/(1 + {b_1}^i f)^{5/3} + {a_2}^i f/(1 + {b_2}^i f^{5/3}) \quad (6)$$

where:

${a_1}^i$, ${a_2}^i$, ${b_1}^i$, ${b_2}^i$: floating parameters,
$_i$: index for different wind component (u: longitudinal, v: lateral, and w: vertical),
u_*: friction velocity (m/s), computed using [20]:

$$U(z) = u_*/\kappa\ (\ln(z/z_o) - \Psi) \quad (7)$$

with:

U(z): mean wind speed at height z (m/s),
κ: von Karman constant (0.4),
z_o: surface roughness (m), taken as 0.0001 m for open sea surface [17],
Ψ: $2\ln(1 + x) + \ln(1 + x^2) - 2\tan^{-1}(x)$; $x = (1 - 19.3\zeta)^{1/4}$.

For this study, the associated coherence for the Pointed-Blunt model is prescribed based on the exponential coherence model, as provided in Equation (2) from the IEC 61400-1. Due to the absence of validated lateral coherences following different atmospheric stability conditions, the exponential coherence in Equation (2) is applied not only for uu- but also for vv- and ww- coherences by assuming the same values are used for the three components.

2.2. Methodology

A floating spar wind turbine was selected for this study, which is based on the International Energy Agency (IEA) Annex XXIII Offshore Code Comparison Collaboration (OC3) Phase IV [21]. The OC3 wind turbine has the 5 MW National Renewable Energy Laboratory (NREL) reference wind turbine (RWT) characteristics with a modified controller to prevent the negative damping effect (excessive motions) of the spar platform [21]. The main characteristics of the OC3 wind turbine are provided in Table 2, while the detailed specifications can be found in Jonkman and Musial [21]. Time domain simulations are performed in this study, where the Simulation Workbench for Marine Applications (SIMA) [22], specifically coupled SIMO-Riflex, is used as the primary simulation tool to obtain the OC3 wind turbine's structural responses and motions. SIMO handles the spar platform's motions and station-keeping behavior, while Riflex deals with flexible slender structure analysis (i.e., forces, moments, and deflection computation of the turbine's blades, wind turbine tower, and mooring lines) based on the Finite Element Modeling [22]. Blade Element Momentum (BEM) theory is implemented in Riflex to compute the aerodynamic responses. The modelled OC3 Hywind wind turbine in SIMA is illustrated in Figure 1. The OC3 Hywind is modelled separately for the following parts: blades, nacelle, tower, spar floater, and mooring lines. Each blade is composed with 17 segments representing different airfoil cross-sections of the NREL 5 MW RWT, while the nacelle is modelled as a body. The tower is made up by 10 segments for each of the tower's cross-section properties, in accordance with Jonkman and Musial [21]. The spar floater is modelled as a body and its hydrodynamic properties are taken from Jonkman and Musial [21].

Table 2. The Offshore Code Comparison Collaboration (OC3) wind turbine general properties [21].

Properties	Value
Power production rating	5 MW
Rotor diameter (hub diameter)	126 m (3 m)
Hub height	90 m
Cut-in, rated, cut-out wind speed	3, 11.4, 25 m/s
Cut-in and rated rotor speed	6.9, 12.1 rpm
Water depth, platform draft	320 m, 120 m
Added mass, drag coefficient	0.969954, 0.6
Number of mooring lines (angle between adjacent lines), mooring line length	3 (120°), 853.87 m

As input to SIMA, environmental conditions are necessary, where waves and wind act as the main environmental loads. The waves' input are taken as constant for all load cases considered in this study, while the wind input defines the load cases. The simulated wave conditions follow a Joint North Sea Wave Project (JONSWAP) spectra with a significant wave height of H_s = 4 m, peak period T_p = 8 s, and a peakedness parameter γ = 3.3, according to DNVGL-CG-0130 [23]. In reality, H_s is dependent on wind speed and should be varied. Additional simulations were performed with variable H_s and T_p. It was noted that simulations with a variable H_s yield similar conclusions (in terms of the OC3 Hywind's responses with respect to the variation in wind input), as to when a constant H_s is adopted. Since our main objective is to investigate the impact of wind input variation on the OC3 wind turbine's responses, a constant H_s with wind speed is used in this study.

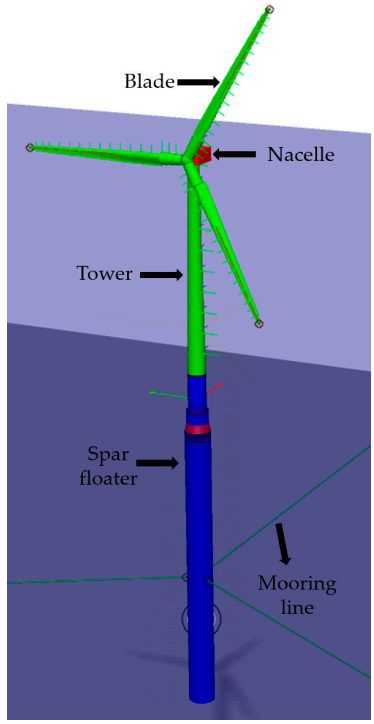

Figure 1. The OC3 Hywind spar wind turbine model in the Simulation Workbench for Marine Applications (SIMA).

The main input for the simulations in SIMA is wind inflow conditions (wind fields) that is depicted in the form of 'moving wind box' in the u-component direction. This box will be referred to as the turbulence box. The turbulence boxes are pre-generated using different pre-processing tools depending on the wind model. TurbSim [19] is used to generate the turbulence box using the Kaimal Model, Mann Turbulence Generator (MTG) [24] for the Mann spectral model, and windSimFast [25] for the Pointed-Blunt model, where the windSimFast is a MATLAB®-based code. The turbulence box contains wind velocity values at each grid point, representing the flow field variation on the rotor for a selected duration, here taken as 1 hour. The turbulence box size is set to (height × width × length = 160 m × 160 m × [U_{hub} (mean wind speed at hub) × 3600]). For example, if U_{hub} is 8 m/s, then the turbulence box size is 160 m × 160 m × 28,800 m. The selected height and width size are to cover the rotor swept area and account for the platform motions. Furthermore, it is important to note that the grids in the turbulence box have proper resolutions. A note on the turbulence box's grid resolution is given in Section 2.2.1.

The load cases (LC) for this study are summarized in Table 3. The load cases are divided into two main cases, LC 1 and LC 2. LC 1 concerns turbulent wind under neutral conditions with two different coherences and LC 2 covers turbulent wind for different atmospheric stability conditions paired with a fixed exponential coherence.

Table 3. Load case (LC).

LC No.	Wind Model	Atmospheric Stability Conditions	Coherence Model	Input Parameters
1a	Kaimal	Neutral	Equation (2)	U_{hub} * = 8 m/s (TI ** = 5.95%) U_{hub} = 11.4 m/s (TI = 6.08%) U_{hub} = 15 m/s (TI = 6.16%)
1b	Mann		Equation (5)	ℓ = 42 m, γ = 3.9 U_{hub} = 8 m/s (TI = 5.95%), $\alpha\varepsilon^{2/3}$ = 0.00956 U_{hub} = 11.4 m/s (TI = 6.08%), $\alpha\varepsilon^{2/3}$ = 0.0203 U_{hub} = 15 m/s (TI = 6.16%), $\alpha\varepsilon^{2/3}$ = 0.036
2a	Pointed-Blunt	Neutral	Equation (2)	$L_m = \infty$ (ζ = 0)
2b		Weakly unstable		L_m = −200 m (ζ = −0.407)
2c		Unstable		L_m = −100 m (ζ = −0.815)
2d		Very unstable		L_m = −50 m (ζ = −1.63) U_{hub} = 8, 11.4, 15 m/s

* U_{hub} = mean wind speed at hub, ** TI = turbulence intensity

The turbulence intensity (TI) input values for LC 1 are set equal to the values simulated with the Pointed-Blunt model under neutral stability conditions (LC 2a). Each of the load cases is simulated for 1 hour with six different random seeds to minimize the uncertainty. It is important to note that the 1-hour long time series of the incoming flow are simulated continuously, i.e., not split into 10 min long segments, in order to include the low-frequency wind gusts.

As a simplification, the effect of wind shear is neglected, and a uniform wind profile is applied for all load cases presented in Table 3. Additional simulations were also performed using a stability-corrected logarithmic mean wind profile for all load cases presented in Table 3. For unstable conditions, there is very little wind shear, and as a result, very little influence was noted on the resultant loads and motions of the OC3 Hywind (less than 10%, depending on the component of interest). Whereas for neutral conditions, we observed that the influence of coherence on the OC3 Hywind responses is greater than the variation in mean wind profile. However, since the focus of this study is a comparison of the turbulent wind models, it is then decided to simplify the comparison by using a constant mean wind profile with height.

2.2.1. A Note on the Turbulence Box's Grid Resolution

When one uses the MTG, the finding by Kim et al. [26] suggests that grid spacing plays an important role in defining a reliable input, and thus the simulation results. Their study pointed out that coarser grid resolution gives a more biased result compared to the finer grid resolution. Hence, a grid resolution check is performed, particularly for the Mann spectral model where the wind turbulence box is generated using MTG. In MTG, the number of grid points in the x, y, and z directions (Nx, Ny, Nz) must follow 2^n, where n is a positive integer. To satisfy this requirement, a number of grid point in the x-direction, Nx = 32,768 is selected, which corresponds to a time step dt of 0.11 s for a 3600 s duration (dt = duration/Nx). Table 4 provides different grid resolutions to be checked. Figure 2a presents the Mann spectral model spectra of the u-component (Su) simulated by the MTG tool for different grid resolutions in Table 4, compared with the target spectra for the Mann spectral model. It can be seen that the variation in grid resolution influences the simulated spectra of the along-wind component Su, particularly at frequencies higher than 0.7 Hz. The simulated spectra Su decays faster than the target spectra at frequencies > 0.7 Hz. The finer grid spacing resulted in simulated spectra Su values closer to the target spectra compared to the coarser grid spacing for frequencies > 0.7 Hz.

Table 4. Convergence study: grid size.

No.	Grid Size dy * = dz ** (m)	No. of Grid Points in y and z Directions Ny = Nz (–)	Lx = 3600 s × U_{hub} = Nx × dx *** (m)	Wind Model
1	10 (coarse)	16	28,800	Kaimal [1], Mann [2]
2	5 (fine)	32	41,040	Kaimal [1], Mann [2]
3	2.5 (very fine)	64	54,000	Kaimal [1], Mann [2]

* grid size in the y-direction, ** grid size in the z direction, *** grid size in the x direction, [1] TurbSim, [2] Mann Turbulence Generator.

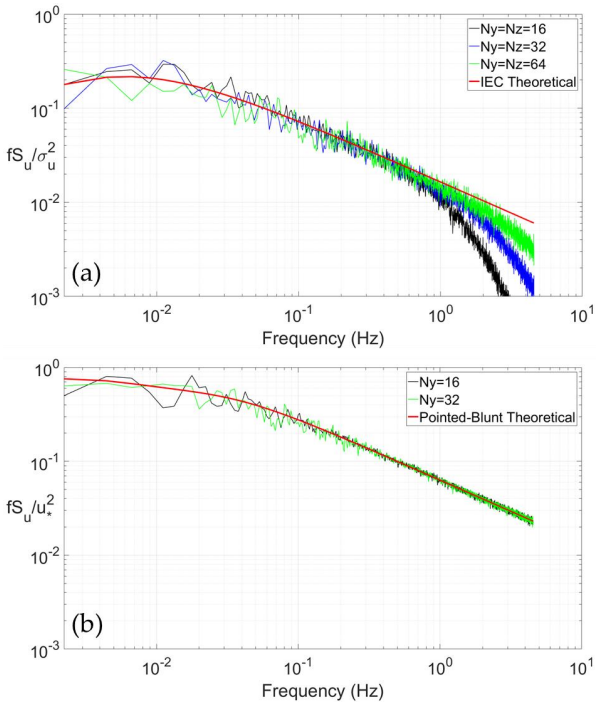

Figure 2. Normalized spectra of the u-component for: (**a**) the Mann spectral model from the Mann Turbulence Generator, and (**b**) the Pointed-Blunt model from windSimFast for different grid resolutions with Nx = 32,768 and 8 m/s mean wind speed at the hub point.

The low-pass filtering in the Mann spectral model assumes the grid points as the average wind speeds in a cube volume of air [27]. Even though a high-frequency compensation is applied when using MTG to allow the grid points to represent a local wind vector instead of the air cube, it seems that the low-pass filtering is not well compensated, even for the very fine grid size (see Table 4). A finer grid is then seen to better represent the smaller scale turbulence. When an isotropic grid (dx = dy = dz) was used, we observed that the simulated spectra in the frequency > 0.7 Hz approaches the theoretical spectra (red line in Figure 2a). Ideally, an isotropic grid spacing would give the closest values with the theoretical ones for all frequency ranges and should be used in the simulations. Nonetheless, such grid spacing is quite difficult to consider in the simulations. The number of grids, Nx, Ny, Nz, must follow 2^n, and MTG's computational power is limited. Moreover, if a constant dx is used for a constant duration of 3600 s, then Nx will change with wind speed, U_{hub}. Hence, the turbulence box size will change with wind speed, U_{hub}. We aim to have a constant wind field size with a continuous duration of 3600 s and a constant time step dt for all considered wind speeds, U_{hub}. Because the use of isotropic grid spacing

will lead to inconsistent turbulence box size with wind speed, the very fine grid size (Ny = Nz = 64) is then selected for all wind simulations using both MTG and TurbSim. As shown in Figure 2b, the grid resolution does not influence the simulated wind of the Pointed-Blunt model. Therefore, a fine grid size (Ny = Nz = 32) is used to generate the wind turbulence box using windSimFast.

The importance of Nx on the simulated spectra Su is related to the time step dt. Nx variation corresponding to a time step from 0.055 to 0.11 s shortens the x-axis, i.e., a smaller time step captures a longer high-frequency range. To save the computational time, a time step of 0.11 s is used to generate the turbulence boxes using all tools, allowing a Nyquist frequency of 4.55 Hz, adequate to capture the OC3 wind turbine's important natural frequencies.

3. Results

The results are divided into three subsections: the simulated wind turbulence in terms of wind turbulence box properties for each load case, the natural frequencies of the OC3 wind turbine, as well as the load and platform motion responses.

3.1. Simulated Wind Turbulence

The generated wind turbulence is checked to make sure that its statistical properties meet the required target values. Figure 3a shows the simulated dimensional spectra Su averaged from the six seeds for the Kaimal model and the Mann spectral model in LC 1 compared to the IEC target spectra, as well as the Pointed-Blunt model under neutral conditions (LC 2a). The comparison between the simulated dimensional spectra Su and the theoretical spectra for LC 2 is given in Figure 3b. The spectra shown in Figure 3 are calculated using the Welch's method with six windows and are plotted as a function of frequency. As shown in Figure 3a, the wind turbulence spectral properties from the Kaimal model and the Mann spectral model agree well with the targeted spectra, except for the Mann spectral model at frequencies > 1 Hz due to the grid size. A good agreement between the simulated spectra and the target spectra is also observed for the Pointed-Blunt model for all stability conditions at all considered wind speeds, and for both v- and w- wind components (Sv and Sw, respectively). Figure 3a shows that the Pointed-Blunt model under neutral conditions in LC 2a has equivalent energy content with the two IEC models, as the TI input for the two IEC models are based on the simulated TI from LC 2a. Comparing different atmospheric stability conditions for LC 2, it can be seen from Figure 3b that the spectra Su is increasing as the stability progressively shifts from neutral to very unstable, except in the 0.008 Hz < frequency < 0.05 Hz range, where neutral conditions produced slightly higher spectra Su than for weakly unstable conditions.

Table 5 gives the range of the simulated TI values of u-component from the six seeds. It can be seen that the simulated TI results for the Kaimal model and the Mann spectral model are slightly lower than the target TI given in Table 3. It is important to note that TI is not an input for the Pointed-Blunt model and thus the TI results for the Pointed-Blunt model are due to the changes in L_m and the value of u_* in Equation (7). From Table 5, it is noted that the TI is increasing as the atmospheric stability moves from neutral to very unstable conditions. This is expected as unstable conditions have higher spectra energy Su than neutral conditions, as shown in Figure 3.

Table 5. Simulated turbulence intensity of the u-component (mean ± variation).

	Turbulence Intensity (%)					
U_{hub} (m/s)	**LC 1**		**LC 2**			
	Kaimal	**Mann**	**Pointed Blunt**			
	(a) Neutral	**(b) Neutral**	**(a) Neutral**	**(b) Weakly Unstable**	**(c) Unstable**	**(d) Very Unstable**
8	5.77 ± 0.17	5.83 ± 0.4	5.95 ± 0.2	6.0 ± 0.23	6.51 ± 0.23	7.6 ± 0.27
11.4	5.93 ± 0.15	5.95 ± 0.4	6.08 ± 0.17	6.11 ± 0.2	6.61 ± 0.2	7.74 ± 0.25
15	6.03 ± 0.14	6.01 ± 0.35	6.16 ± 0.16	6.18 ± 0.2	6.67 ± 0.2	7.83 ± 0.23

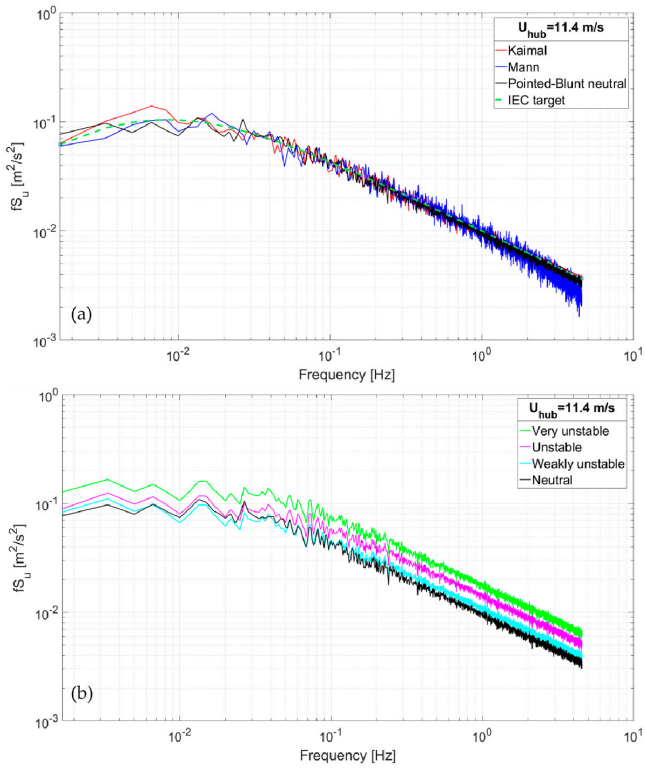

Figure 3. Spectra of the u-component for 11.4 m/s mean wind speed at hub point based on: (**a**) Kaimal model and Mann spectral model, and (**b**) Pointed-Blunt model for various stability conditions.

Figure 4 presents the comparison between the simulated wind lateral coherences and the empirical formula (target coherence function) plotted as a function of reduced frequency = $f \times \Delta/U_{hub}$. Where f is the frequency (Hz), Δ is the separation distance (m), and U_{hub} is the mean wind speed at the hub. The simulated coherences are obtained based on the Kaimal and Mann spectral models for 65 and 100 m lateral separations for all considered wind speeds. As can be seen in Figure 4, the simulated coherences for all wind speeds agree with the target function. We also note this agreement for a small lateral separation of 10 m and for the vertical separations, which are for brevity not presented here. The simulated coherences for the lateral and vertical separations of the Pointed-Blunt model are not shown here but are also observed to be in good agreement with the target exponential coherence function.

Figure 5 compares the target coherence functions for the exponential coherence model and the Mann spectral model coherence, for the lateral and vertical separations, respectively. In terms of lateral coherence, the Mann spectral model gives lower values than the exponential coherence for the considered reduced frequencies, as shown in Figure 5a. For the vertical coherence, the two coherences are closer to each other, and the one from the Mann spectral model is lower than the exponential coherence for reduced frequencies higher than 0.075 (Figure 5b).

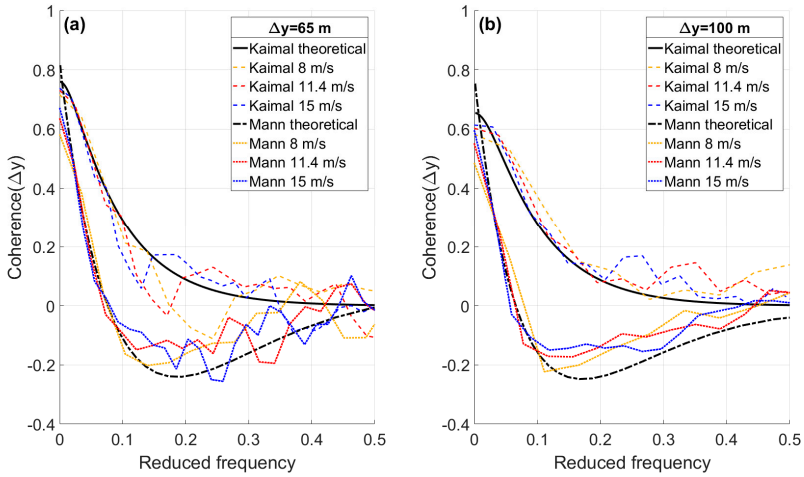

Figure 4. Simulated lateral coherences of the u-component for the Kaimal (exponential coherence) and the Mann spectral models for different mean wind speeds at: (**a**) 65 m separation (rotor radius) and (**b**) 100 m separation distances.

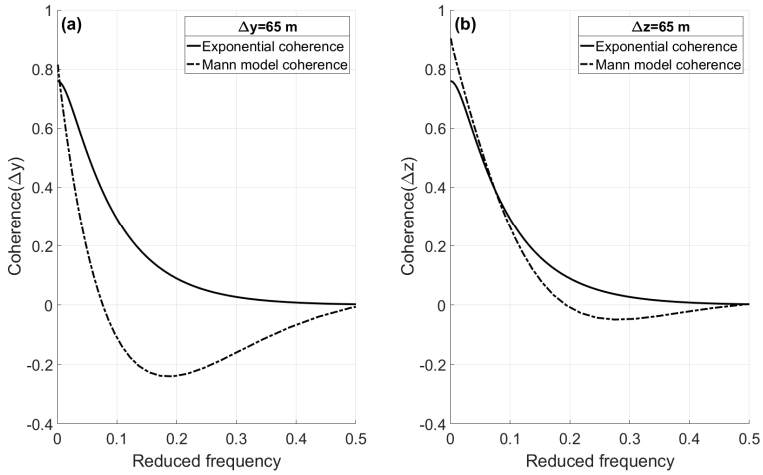

Figure 5. Theoretical coherences of the u-component at 65 m separation (rotor radius) distance for: (**a**) lateral separation and (**b**) vertical separation comparing the exponential coherence and the Mann spectral model coherence.

3.2. Natural Frequencies

Free decay tests are performed in SIMA to obtain the natural frequencies of the OC3 Hywind. This is done by considering no wind and still water (no waves) conditions in the simulations. The natural frequency for the OC3 Hywind's first eight modes is given in Table 6. The values match well with the values obtained in the OC3 code comparison study by Jonkman and Musial [21], except for the platform pitch and the first two tower modes. The corresponding natural frequencies obtained in the study by Saccoman [28] by using Horizontal Axis Wind turbine simulation Code 2nd generation (HAWC2) numerical simulation [24] are also presented in Table 6. It can be seen that the platform pitch and the first two tower modes' natural frequencies from our study are close to those by Saccoman [28]. The pitch natural frequency of 0.033 Hz as in the present study was also computed by Ahn and Shin [29]

using FAST aeroelastic tool [30]. It is important to note that the OC3 Hywind's natural frequency presented in Table 6 is far lower than the frequency region affected by the grid resolution as discussed in Section 2.2.1.

Table 6. Natural frequencies of the OC3 wind turbine.

Mode	Natural Frequency (Hz)	OC3 Code Comparison [21] (in Hz)	Saccoman [28] (in Hz)
Surge	0.00714	0.0085–0.0093	0.00776
Sway	0.0073	0.0085–0.0091	0.00776
Roll	0.045	0.51–0.55	0.0324
Pitch	0.033	0.054–0.057	0.0324
Heave	0.045	0.05–0.054	0.0305
Yaw	0.12	0.112–0.18	0.121
First tower side–side	0.492	0.67–0.7	0.448
First tower fore–aft	0.52	0.6–0.71	0.464

3.3. Load and Motion Responses

The output from the SIMA simulations are the stress-resultant time series (force, torsional moment, bending moment) for different components as well as motion response time series. The OC3 wind turbine load responses are quantified in terms of fatigue damage, while the platform motion responses are presented in the form of minimum and maximum values from the 6 seeds, and the averaged standard deviation from the six seeds. To quantify the fatigue, the rain flow counting method [31] is adopted by transforming the load response time series into Damage Equivalent Load (DEL). The DELs are then computed using:

$$\mathrm{DEL} = (\Sigma N_i St_i{}^m / n_{eq})^{1/m} \quad (8)$$

where:

DEL: damage equivalent load,
N_i: total number of cycles causing failure in bin i from rain flow counting,
S_i: load magnitude causing failure in bin i from rain flow counting,
n_{eq}: equivalent number of cycles,
m: Wöhler exponent (taken as 3 for steel material and 12 for fiberglass).

The DEL is quantified in 1 Hz duration, so n_{eq} is set as 3600 to represent the simulation duration of 1 hour. The DELs from each turbulent wind load case are computed and compared for the following resulting moments of the OC3 wind turbine: tower base fore–aft bending, tower base side–side bending, tower base torsional, tower top torsional, and blade root flap-wise bending. The load and motion responses are discussed separately in two different subsections. The first one is the load and motion responses from LC 1, where turbulent wind under neutral conditions with different coherences are compared. Secondly, the load and motion responses from LC 2, where turbulent wind under different atmospheric stability conditions, from neutral to very unstable, are described.

3.3.1. Influence of Coherences under Neutral Atmospheric Stability Conditions

The OC3 wind turbine responses with respect to variation in the coherence under neutral conditions (LC 1) show that the tower base side–side moment, the tower top torsional moment, and the tower base torsional moment are the most affected components. It is observed that the Mann spectral model results in up to 27%, 20%, and 20% higher DELs than the Kaimal model respectively, for the aforementioned components at the highest considered wind speed 15 m/s (see Figure 6 for torsional moment). In contrast, the tower base fore–aft moment and the blade root flap-wise moment are not significantly affected by the variation in coherence under neutral conditions. The Mann spectral model yields 2% higher DELs for the tower base fore–aft moment and 5% lower DELs for the blade root

flap-wise moment. The small difference in the blade root flap-wise moment responses associated with the two different spectral models are consistent with the uniform wind profile that is adopted for all cases in LC 1. Sathe and Bierbooms [32] showed that the mean wind shear profile governs the blade loads. The uniform mean wind profile, accompanied by a uniform TI with height (the numerical simulations of a flow field with nominally uniform turbulence intensity of, for example, 5.95%, result in a variation of turbulence intensity of about 0.5% across the rotor area, both for the Kaimal model and the Mann spectral model flow fields. Such variations in the simulated flow characteristics across the rotor area are considered to be of a secondary importance for the studied wind turbine responses), and the fact that turbulence correlation over smaller distances (than those relevant for the tower twisting and yawing) dominates the dynamic loading of a single blade, all contribute to a limited influence on the blade root flap-wise responses in the present study.

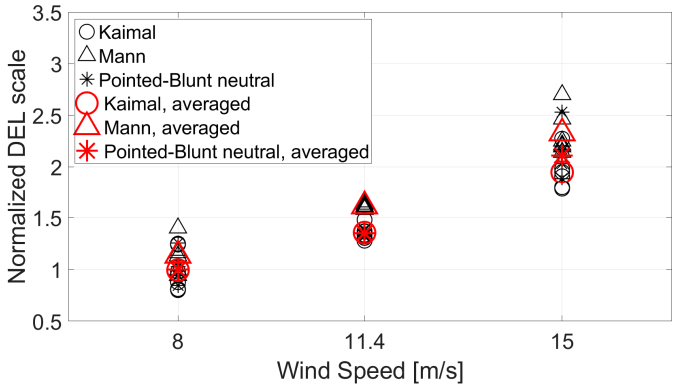

Figure 6. Normalized Damage Equivalent Loads (DELs) of tower top torsional moment for neutral conditions for the Kaimal and Mann spectral models using standard TI (LC 1) and the Pointed-Blunt model under neutral conditions (LC 2a). The black markers represent seeds while the red markers represent the average value of the six seeds at the respective wind speeds.

The tower base fore–aft moment response is the least influenced by variation in the coherences comparing the Kaimal model and the Mann spectral model. This is consistent with a small difference in vertical coherence between the two models, as shown in Figure 5b. In contrast to this, the different vertical coherences for different atmospheric stability conditions were found to give 75% difference in the tower base fore–aft loads for a bottom-fixed wind turbine [9]. A further investigation of the influence of the representative, stability dependent vertical coherence on the tower fore–aft response of a floating wind turbine is however needed to examine this and is not discussed in the present study. On the other hand, the tower base side–side responses vary greatly with the difference in the coherences, where a lower coherence produced a 27% higher response, which might be caused by the induced tower base torsional moment.

Since the characteristic of the tower top and the tower base torsional moments are alike, only the tower top torsional moment is discussed in the following. Figure 6 presents the normalized DELs for the tower top torsional moment for the Kaimal model and the Mann spectral model in LC 1 and the Pointed-Blunt model under neutral conditions in LC 2a. The DELs are normalized with the values from LC 2a at 8 m/s. The tower top torsional moment DELs are increasing significantly with wind speed, as shown in Figure 6. The difference in the tower top torsional moment DEL is evident between the Kaimal and Mann spectral models (Figure 6). From Figure 3 and Table 5, we see that the Kaimal and Mann spectral models have approximately equal energy content and TI.

The difference in the DEL values is understood to be due to the difference in the coherence functions associated with the Kaimal model and the Mann spectral model, in particular the difference in the lateral coherence (see Figures 4 and 5a). The lower lateral coherence in the Mann spectral model

than in the Kaimal model represents less correlated wind gusts at lateral separations, i.e., a higher 'asymmetry' of the wind field which then creates higher twisting loads about the wind turbine's vertical axis. A similar result has also been noted in previous studies [7,8]. Since the Pointed-Blunt model under neutral conditions is used here with the same lateral coherence as for the Kaimal model, the tower top torsional moment responses for the two models are quite similar, as can be seen in Figure 6.

With respect to platform motions, it is found that the platform's sway, roll, and yaw are the most affected responses by the differences in the coherence functions. The platform sway and roll are of relatively small magnitude, between −1.3 to +0.6 m for sway and −0.3 to +0.6° for roll at the highest wind speed. The platform yaw is in the range of −2.7 to +1.1° for LC 1 at the highest wind speed investigated, as shown in Figure 7. The standard deviations of the platform yaw resulted from the Kaimal model and the Pointed-Blunt model LC 2a are similar, while the yaw response associated with the Mann spectral model is slightly higher than the two, by 0.1 at 15 m/s wind speed (Figure 7). This is due to the Kaimal model and the Pointed-Blunt model LC 2a that have the same lateral coherences, higher than the lateral coherence of the Mann spectral model. The lower lateral coherence by the Mann spectral model causes a higher twisting moment about the wind turbine's vertical axis and thus induces a higher yaw motion of the floater.

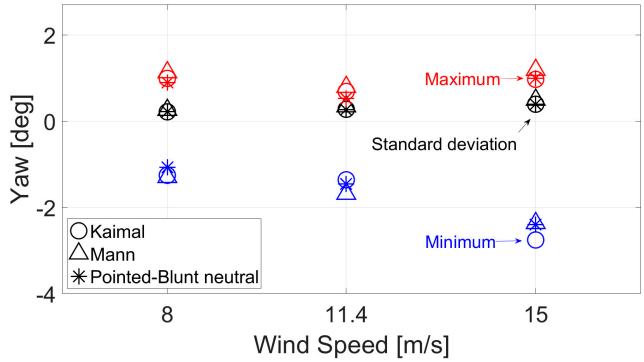

Figure 7. Platform yaw minimum (blue markers), maximum (red markers), and standard deviation (black markers) for the Kaimal and Mann spectral models (LC 1) and the Pointed-Blunt model under neutral conditions (LC 2a).

In general, the variation in platform yaw with different turbulent wind conditions in LC 1 shows similar trends with the increase in mean wind speed as the tower top torsional moment DELs (see Figures 6 and 7). This demonstrates the interdependency between the tower torsional moment and the platform yaw response. The platform surge shows a limited sensitivity to the difference in coherences between the Kaimal model and the Mann spectral model. The platform surge is mainly influenced by the thrust on the rotor, which depends greatly on the mean wind speed. The same is observed for platform pitch motion which largely follows the effect of thrust force [33]. For a spar-type wind turbine, the influence of wave conditions on the heave response is more pronounced than the influence of turbulent wind [7]. The observed insignificant response of the platform heave with the difference in the coherences is due to the wave conditions that are kept constant.

Figure 8 presents a segment of the simulated time series of the tower top torsional moment and the yaw response from the Mann spectral model. It can be seen that, generally, the platform yaw angle and the tower top torsional moment are highly correlated. The computed correlation coefficients between the tower torsional moment and the platform yaw are in the range of 0.55 to 0.8.

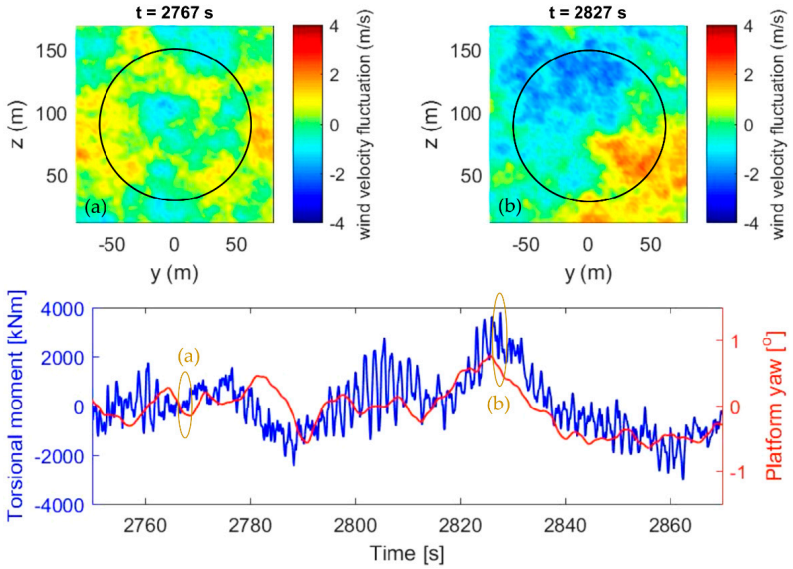

Figure 8. Wind velocity fluctuations over the rotor (**upper figure**) and the tower top torsional moment and yaw response (**lower figure**) for the Mann spectral model at 15 m/s mean wind speed at the hub, in case of a small (a) and large (b) twisting moment. The circle lines represent the rotor swept area.

The snapshots of the underlying wind velocity fluctuations across the rotor are also included, for a case of large and small twisting moment. The moments are seen to be associated with the asymmetrical and the symmetrical distribution of the wind velocity fluctuation over the rotor, with respect to the vertical line y = 0 m. A 'differential' action of wind gusts corresponding to an asymmetric field distribution leads to an extreme yaw response of the OC3 wind turbine, in line with the previous discussion. A uniform, symmetric distribution of wind fluctuation over the rotor has an opposite effect.

3.3.2. Influence of Variation in the Atmospheric Stability Conditions

For different atmospheric stability conditions, the tower base side–side moment, the tower top torsional moment, and the tower base torsional moment of the OC3 wind turbine are found to be the most affected components. In LC 2, the wind loads associated with the very unstable conditions result in 27%, 27%, and 26% higher DELs than with the neutral conditions respectively, for the aforementioned components. The DELs of the three most affected component are highest under very unstable conditions, followed by unstable, and then weakly unstable and neutral conditions with close values (less than 3% difference). This is explained by the highest wind energy content under very unstable conditions, followed by unstable, and then weakly unstable and neutral conditions with close values (see the spectra in Figure 3b and the TI values in Table 5 for LC 2). The higher the energy content, then the higher the resultant TI level, and therefore results in higher tower base side–side moment, the tower top torsional moment, and the tower base torsional moment responses. Similar results were shown in previous studies [14,15].

On the other hand, the tower base fore–aft moment and the blade root flap-wise moment are not significantly affected by the variation in turbulent wind input for progressively more unstable conditions. Very unstable conditions yield 4% and 3% higher DELs compared to those under the neutral conditions for the tower base fore–aft moment and the blade root flap-wise moment, respectively. The blade root flap-wise moment response is the least influenced by the difference in stability conditions, similar to the results in the above analysis of the wind load conditions in LC 1. The small difference in the tower base fore–aft moment response by comparing different stability conditions is due to the

fact that the tower base fore–aft response is mainly influenced by the spar platform's surge and pitch motion, that are predominantly affected by the considered waves. Since a constant wave input is considered for all cases in LC 2, we observe an insignificant response change in the tower base fore–aft response with respect to the difference in turbulent wind energy content.

Figures 9 and 10 show the tower top torsional moment and the tower base side–side moment normalized DELs respectively, for different stability conditions. The DELs are normalized with the DEL values obtained for neutral conditions (LC 2a) at 8 m/s. The tower top torsional moment DELs are increasing with wind speed (Figure 9) and so is the tower base side–side moment DELs (Figure 10).

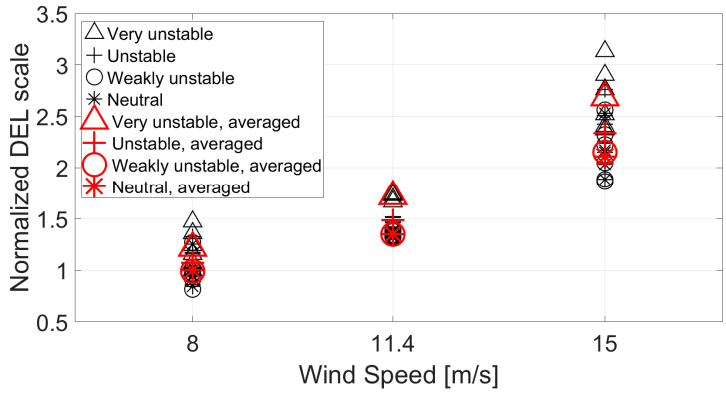

Figure 9. Normalized DELs of the tower top torsional moment for different atmospheric stability conditions for the Pointed-Blunt model (LC 2). The black markers represent seeds while the red markers represent the average value of the six seeds at the respective wind speeds.

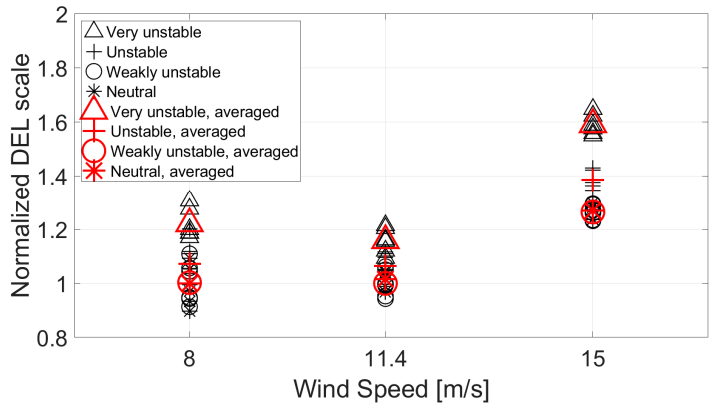

Figure 10. Normalized DELs of the tower base side–side moment for different atmospheric stability conditions for the Pointed-Blunt model (LC 2). The black markers represent seeds while the red markers represent the average value of the six seeds at the respective wind speeds.

The normalized tower top torsional DEL values as associated with the Mann spectral model LC 1b (Figure 6) appear to be 'catching up' with the resulting DEL values from the Pointed-Blunt model LC 2c (Figure 9), even though the LC 1b under neutral conditions has a somewhat lower TI level than the unstable conditions in LC 2c (Table 5). The Pointed-Blunt model for all stability conditions is simulated with a fixed exponential coherence, with a higher lateral coherence level than the Mann spectral model, as shown in Figure 4. As a result, the Mann spectral model wind fields are more 'asymmetrical' relative

to the Pointed-Blunt wind fields and result in a twisting moment about the wind turbine's vertical axis that is comparable with the Pointed-Blunt model for unstable conditions with higher TI.

The average power spectral density (PSD) from the six simulated seeds of the tower top torsional moment response for different stability conditions in LC 2 are presented in Figure 11. The tower top torsional moments are the highest under very unstable conditions, followed by unstable conditions, then weakly unstable and neutral conditions with a small discrepancy, as expected. This agrees with the DEL trend presented in Figure 9 for the tower top torsional moment. The major excitation frequencies for the tower top torsional moment are the wave peak frequency, the blade passing 1P frequency, and the blade passing 3P frequency. The wave excitation in the tower top torsional moment response might be due to the platform yaw natural frequency (0.12 Hz) that is excited by the wave peak frequency at around 0.125 Hz. Therefore, we observed the wave excitation in the tower top torsional moment response due to the interdependency between the tower top torsional moment and the platform yaw response. However, the contribution of the excitation blade passing frequencies, 1P and 3P to the tower top torsional moment is higher than that of the wave excitation. This agrees with the findings in References [7,34]. Furthermore, the low-frequency wind excitation (less than 0.1 Hz) is also seen to generate an important part of the torsional moment variations. This indicates the importance of precise description of wind inflow conditions on the rotor of a spar wind turbine, as the rotor harmonics appears to significantly affect the tower torsional moment response.

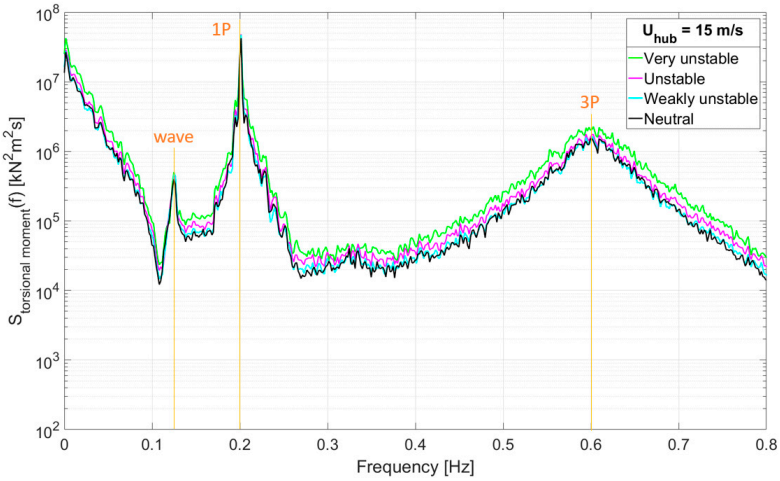

Figure 11. Tower top torsional moment power spectral density (PSD) for different stability conditions in LC 2 at 15 m/s mean wind speed at the hub.

In terms of platform motions, it is found that the platform's sway, roll, and yaw are the most sensitive to the variations in the atmospheric stability conditions in LC 2. The platform sway and roll are of relatively small magnitude, between −1.4 to +0.65 m for sway and −0.3 to +0.63° for roll. The platform yaw is in the range of −2.9 to +1.1° for LC 2 at the highest wind speed investigated, as shown in Figure 12. The platform yaw shows similar trends with the increase in mean wind speed for different stability conditions as the tower top torsional moment DELs (see Figures 9 and 12). Again, this indicates the related excitation mechanisms for both the tower torsional moment and the platform yaw response. The platform yaw standard deviation is the highest under very unstable and the lowest under neutral conditions, with the latter result being close to that for weakly unstable conditions. The platform surge and pitch are found to be driven by the wave conditions which are not varied in the present study. In the frequencies 0.033 Hz < f < 0.07 Hz, we note the highest surge and pitch spectral energy under very unstable conditions, which decreases as the stability shifts to neutral conditions with small discrepancies. In the wave excitation frequency (0.125 Hz) to 0.3 Hz, no spectral energy

discrepancies are observed and the spectral energy under all stability conditions coincides with each other. The same is noted for the platform heave, which is, again, more prone to the variation in wave conditions [7], which are not varied in the present study.

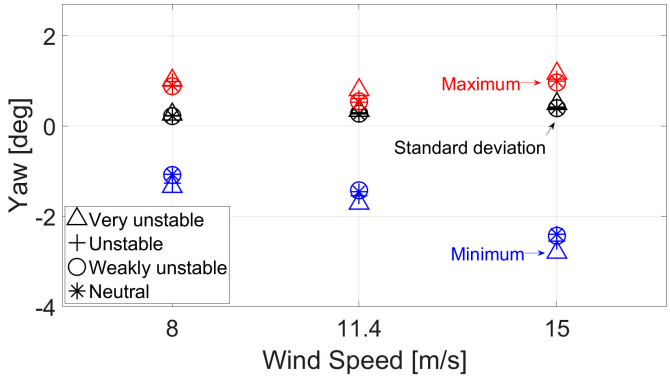

Figure 12. Platform yaw minimum (blue markers), maximum (red markers), and standard deviation (black markers) comparing the Pointed-Blunt model for different stability conditions (LC 2).

Figure 13 shows the average PSD of the platform yaw response from the six simulated seeds, for different stability conditions in LC 2. It can be seen that the platform yaw responses are the highest under very unstable conditions and decrease as the stability changes to neutral conditions. The platform yaw is mainly excited by the low-frequency turbulence, the wave excitation, and the blade passing 1P and 3P frequencies. The wave excitation in the platform yaw response might be because the platform yaw natural frequency (0.12 Hz) has a very close value with the wave peak frequency (0.125 Hz). Nonetheless, the 1P excitation gives a higher contribution than the wave excitation.

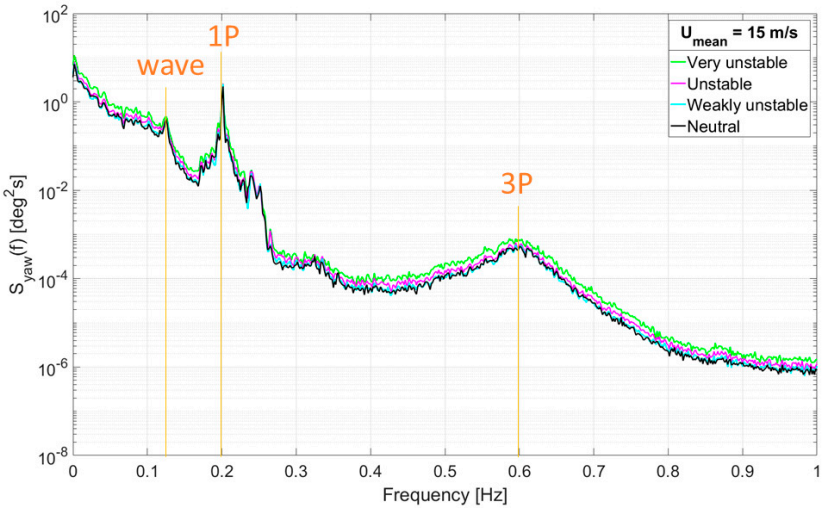

Figure 13. Platform yaw PSD comparison for the different stability conditions in LC 2 at 15 m/s mean wind speed at the hub.

4. Conclusions

The present study was motivated by previous studies [6–8] which suggest that the wind spatial coherence is an important factor to consider when simulating the motions of a spar floating wind

turbine. In addition, Putri et al. [14] demonstrated the importance of unstable atmospheric conditions for a spar floating wind turbine's loads and motions. Through SIMA simulations and relevant wind turbulence simulation tools, the influence of different turbulent wind conditions on the OC3 wind turbine loads and motions was investigated. The primary objectives of the study were to clarify how the two turbulent wind models given in the IEC standards result in different stress resultants and motion responses of the OC3 wind turbine, even though both models imply the same energy content for neutral atmospheric stability conditions for a single point spectra. The difference in the spatial coherence between the two models was demonstrated as the main cause for the differences in the wind turbulence load effects on the OC3 turbine. The importance of defining the appropriate coherence for offshore conditions was thus highlighted. The coherence functions of the Kaimal and Mann spectral models for neutral atmospheric stability gave different levels of frequency-dependent correlation of wind gusts, particularly for the across-flow, lateral separations. The lower lateral coherence simulated by the Mann spectral model resulted in higher tower top torsional moments and tower base side–side moments than the Kaimal model by 20% and 27%, respectively.

Additionally, we aimed to demonstrate the impact of the energy level and turbulence content, related to the non-neutral atmospheric stability, especially unstable conditions on the OC3 wind turbine load and motion responses. This was performed by using the Pointed-Blunt spectral model, which was previously derived from FINO1 wind measurement data. The observed increase in the simulated DELs as the atmospheric stability shifts from neutral to very unstable was strongly correlated with the increase in the turbulent wind energy content, and thus the respective increase in TI. The simulated DEL values for tower top torsional moment and tower base side–side bending moment under very unstable conditions were 27% and 26% higher than the values under neutral conditions.

The two aspects of the turbulent wind field, the coherence and the energy content, were studied by changing each aspect at the time. Different flow characteristics were simulated without considering the variations with height. Such idealized flow fields are suited to identify the importance of each aspect of the turbulent flow field, rather than to fully represent conditions in a wind field.

The same exponential coherence was assumed for uu-, vv-, and ww- components due to the absence of relevant information. We also ran simulations with the Kaimal spectral model by using the same exponential coherence for uu- (Equation (2)) but applying identity coherence for vv- and ww- (as suggested by Jonkman [19]). This case resulted in only 2% smaller DEL values than the values presented in this study, depending on the component of interest. The coherence functions for the vv- and ww- components adopted in the present study are hence considered plausible and suitable for the analyses carried out.

The variation in the spatial coherences for different atmospheric stability conditions was not considered in the present study. Instead, fixed coherence values for different atmospheric stability conditions were assumed due to the absence of a valid lateral coherence under non-neutral conditions. The study by Doubrawa et al. [8] showed that the lateral coherences obtained from LES might be sensitive to the change in atmospheric stability conditions only at frequencies lower than 0.1 Hz and separations higher than 140 m for 8 m/s wind speeds. In other words, generally, the lateral coherences yielded from LES under neutral, stable, and unstable conditions are relatively similar, except at the mentioned separations. Therefore, the assumption of pairing a fixed coherence to the Pointed-Blunt model under different unstable conditions in this study could be reasonable. A campaign attempting to acquire the spatial wind coherence information with respect to atmospheric stability conditions from the wind measurements at Obrestad site is currently on-going, but the results are yet to be published [35]. This data can potentially be used for future work.

The present study does not aim to highlight a particular turbulent wind model to predict the accurate responses of a floating wind turbine using numerical simulations. The use of reliable site-specific measured wind data to simulate the wind fields as input into numerical simulations is necessary to get an accurate structural response prediction. Alternatively, the use of LES to simulate the wind fields might also be an option, as demonstrated in the study by Doubrawa et al. [8].

Author Contributions: Conceptualization, R.M.P., C.O., J.B.J. and M.C.O.; data curation, R.M.P.; formal analysis, R.M.P., C.O. and J.B.J.; investigation, R.M.P. and C.O.; methodology, R.M.P.; software, R.M.P.; supervision, C.O., J.B.J. and M.C.O.; visualization, R.M.P.; writing—original draft preparation, R.M.P.; writing—review and editing, C.O., J.B.J. and M.C.O. All authors have read and agreed to the published version of the manuscript.

Funding: This research received no external funding.

Acknowledgments: The authors would like to express their sincerest gratitude to Etienne Cheynet for the support and knowledge provided.

Conflicts of Interest: The authors declare no conflict of interest.

References

1. IEC. *Wind Turbines–Part 1: Design Requirements*; IEC: Geneve, Switzerland, 2005.
2. Kaimal, J.C.; Wyngaard, J.C.; Izumi, Y.; Coté, O.R. Spectral Characteristics of Surface-layer Turbulence. *Q. J. R. Meteorol. Soc.* **1972**, *98*, 563–589. [CrossRef]
3. Mann, J. The spatial structure of neutral atmospheric surface-layer turbulence. *J. Fluid Mech.* **1994**, *273*, 141–168. [CrossRef]
4. Eliassen, L.O.; Obhrai, C. Coherence of Turbulence Wind under Neutral Wind Condition at FINO1. *Energy Procedia* **2016**, *94*, 388–398. [CrossRef]
5. FINO1–Research Platform in the North and Baltic Seas No. 1. Available online: https://www.fino1.de/en/ (accessed on 27 December 2019).
6. Godvik, M. Influence of Wind Coherence on the Response of a Floating Wind Turbine. In Proceedings of the NORCOWE Science Meets Industry, Stavanger, Norway, 6 April 2016.
7. Bachynski, E.E.; Eliassen, L. The Effects of Coherent Structures on the Global Response of Floating Offshore Wind Turbines. *Wind Energy* **2019**, *22*, 219–238. [CrossRef]
8. Doubrawa, P.; Churchfield, M.J.; Godvik, M.; Sirnivas, S. Load Response of a Floating Wind Turbine to Turbulent Atmospheric Flow. *Appl. Energy* **2019**, *242*, 1588–1599. [CrossRef]
9. Sathe, A.; Mann, J.; Barlas, T.; Bierbooms, W.A.; Van Bussel, G.J. Influence of Atmospheric Stability on Wind Turbine Loads. *Wind Energy* **2013**, *16*, 1013–1032. [CrossRef]
10. Krogsæter, O.; Reuder, J. Validation of Boundary Layer Parameterization Schemes in the Weather Research and Forecasting (WRF) Model under the Aspect of Offshore Wind Energy Applications—Part II: Boundary Layer Height and Atmospheric Stability. *Wind Energy* **2014**, *18*, 1291–1302. [CrossRef]
11. Energy, D.W. DTU Vindenergi: Testcenter Høvsøre. Available online: https://www.vindenergi.dtu.dk/test-centers/hoevsoere_dk(accessed on 7 June 2019).
12. Cheynet, E.J.; Jakobsen, J.B.; Reuder, J. Velocity Spectra and Coherence Estimates in the Marine Atmospheric Boundary Layer. *Bound. Layer Meteorol.* **2018**, *169*, 429–460. [CrossRef]
13. Højstrup, J. A Simple Model for the Adjustment of Velocity Spectra in Unstable Conditions Downstream of an Abrupt Change in Roughness and Heat Flux. *Bound. Layer Meteorol.* **1981**, *21*, 341–356. [CrossRef]
14. Putri, R.M.; Obhrai, C.; Knight, J.M. Offshore Wind Turbine Loads and Motions in Unstable Atmospheric Conditions. *J. Phys. Conf. Ser.* **2019**, 1356. [CrossRef]
15. Knight, J.M.; Obhrai, C. The Influence of an Unstable Turbulent Wind Spectrum on the Lodas and Motions on Floating Offshore Wind Turbines. *IOP Conf. Ser. Mater. Sci. Eng.* **2019**, 700. [CrossRef]
16. Saranyasoontorn, K.; Manuel, L.; Veers, P.S. A Comparison of Standard Coherence Models for Inflow Turbulence with Estimates from Field Measurement. *J. Sol. Energy Eng.* **2004**, *126*, 1069–1082. [CrossRef]
17. Dyrbye, C.; Hansen, S.O. *Wind Loads on Structures*; John Wiley & Sons Ltd.: West Sussex, UK, 1997.
18. IEC. *Wind Energy Generation Systems—Part 1: Design Requirements*; IEC: Geneve, Switzerland, 2019.
19. Jonkman, J. *TurbSim User's Guide: Version 2.00.00*; National Renewable Energy Laboratory (NREL): Golden, CO, USA, 2016.
20. Veritas, D.N. *Environmental Conditions and Environmental Loads*; Det Norske Veritas: Høvik, Norway, 2010; Volume DNV-RP-C205.
21. Jonkman, J.; Musial, W. *Offshore Code Comparison Collaboration (OC3) for IEA Task 23 Offshore Wind Technology and Deployment*; National Renewable Energy Laboratory (NREL): Golden, CO, USA, 2010.
22. Ocean, S. SIMA. Available online: https://www.sintef.no/en/software/sima/ (accessed on 28 September 2019).
23. DNVGL. *DNVGL-CG-0130; Wave Loads*; DNVGL AS: Høvik, Norway, 2018.

24. Larsen, T.J.; Hansen, A.M. *How 2 HAWC2, the User's Manual*; Department of Wind Energy: Roskilde, Denmark, 2019.
25. Cheynet, E. Wind Field Simulation. Available online: https://se.mathworks.com/matlabcentral/fileexchange/50041-wind-field-simulation-the-user-friendly-version (accessed on 19 October 2018).
26. Kim, Y.L.; Lutz, T.; Jost, E.; Gomez-Iradi, S.; Muñoz, A.; Méndez, B.; Lampropoulos, N.; Stefanatos, N.; Sørensen, N.N.; Madsen, H.; et al. *AVATAR Deliverable D2.5: Effects of Inflow Turbulence on Large Wind Turbines*; D2.5; ECN Wind Energy: Petten, The Netherland, 2016.
27. Energy, D.W. HAWC2 Online Course. Available online: https://windenergy.itslearning.com/ContentArea/ContentArea.aspx?LocationID=29&LocationType=1 (accessed on 12 February 2016).
28. Saccoman, M. Coupled Analysis of a Spar Floating Wind Turbine considering both Ice and Aerodynamic Loads. Master's Thesis, Aalto University, Aalto, Finland, 2015.
29. Ahn, H.-J.; Shin, H. Model test and numerical simulation of OC3 spar type floating offshorewind turbine. *Int. J. Nav. Archit. Ocean Eng.* **2019**, *11*, 1–10. [CrossRef]
30. Jonkman, J. FAST: An Aeroelastic Computer-Aided Engineering (CAE) Tool for Horizontal Axis Wind Turbines. Available online: https://nwtc.nrel.gov/FAST (accessed on 2 December 2019).
31. Tatsuo, E.; Koichi, M.; Kiyohumi, T.; Kakuichi, K.; Masanori, M. Damage evaluation of metals for random or varying loading—Three aspects of rain flow method. *Mech. Behav. Mater.* **1974**, *1*, 371–380.
32. Sathe, A.; Bierbooms, W. Influence of Different Wind Profiles due to Varying Atmospheric Stability on the Fatigue Life of Wind Turbines. *J. Phys. Conf. Ser.* **2007**, *75*, 767–780. [CrossRef]
33. Bachynski, E.E. Fixed and Floating Offshore Wind Turbine Support Structures. In *Offshore Wind Energy Technology*; John Wiley & Sons Ltd.: West Sussex, UK, 2018. [CrossRef]
34. Putri, R.M. A Study of the Coherences of Turbulent Wind on a Floating Offshore Wind Turbine. Master's Thesis, University of Stavanger, Stavanger, Norway, 2016.
35. Flügge, M.; Heggelund, Y.; Reuder, J.; Godvik, M.; Nielsen, F.G.; Jakobsen, J.B.; Svardal, B.; Cheynet, E.; Obhrai, C. COTUR Measuring Coherence and Turbulence with LIDARs. In Proceedings of the EERA DeepWind, Trondheim, Norway, 16–18 January 2019.

Paper 3
Response sensitivity of a semisubmersible floating offshore wind turbine to different wind spectral models

*Rieska Mawarni Putri[1], Charlotte Obhrai[1], and Jasna Bogunovic Jakobsen[1]
[1]Department of Mechanical and Structural Engineering and Materials Science, University of Stavanger, Norway

Response sensitivity of a semisubmersible floating offshore wind turbine to different wind spectral models

R M Putri [1], C Obhrai[1], J B Jakobsen[1]

[1]Department of Mechanical and Structural Engineering and Material Science, University of Stavanger, 4026, Stavanger, Norway

rieska.m.putri@uis.no

Abstract. Previous research on the OC3 spar floating offshore wind turbine (FOWT) has shown the sensitivity of the yaw and side-side modes' load and motion responses to different atmospheric conditions. Using the same baseline turbine of the OC3 spar wind turbine for a semisubmersible floater (OC4), this study investigates the load and motion responses of such offshore wind turbine for neutral and unstable atmospheric conditions. The effect of different levels of wind spatial coherence associated with two different wind spectral models for neutral conditions (Kaimal and Mann) are studied for the same turbulence intensity levels. An increase of 18% in the tower torsional moment fatigue damage equivalent load (DEL) is observed for the wind inflow with the weakest coherence (Mann spectral model), compared to the DELs under turbulent wind inflow with the highest coherence (Kaimal spectral model). Unstable atmospheric conditions are also simulated based on the Pointed-Blunt spectral model derived from FINO1 wind measurement. The yaw mode of the semisubmersible wind turbine is found to be the response component most affected by the variation in atmospheric stability conditions. A 28% higher fatigue DEL for the tower torsional moment is observed for very unstable atmosphere than the DELs under neutral atmospheric conditions.

1. Introduction

In recent years, the bottom fixed offshore wind industry has matured to the point that subsidies are no longer required. As we develop sites farther from shore and in deeper waters, floating offshore wind turbines will become the next generation of the offshore wind power producing devices. Floating substructures are offered as an alternative solution enabling cost reduction and installation simplicity compared to the bottom-fixed substructures in the deep water offshore. The two well-known floating offshore wind farms currently built in Europe, the Hywind Scotland and the WindFloat Atlantic, adopt a spar floater and a semisubmersible floater. A FOWT structure must be designed to withstand offshore environmental loads, primarily waves, current, and wind during its lifetime. While the overall responses of a FOWT floater under wave loading are well understood from the oil and gas designs, its responses with respect to wind loading however are still a topic of active research.

The FOWT floaters carry not only the dead loads from the wind turbine, but also the rotating blade harmonic loads which are affected by the turbulent wind conditions on the rotor. In particular, the low-frequency part of the turbulent wind contributes to loading in the rotating rotor frequencies [1]. Moreover, the interaction between each degree of freedom (DOF) of the floater motions and the rotor's responses due to the wind inflow is also a concern. When a FOWT is pitching, the resulting rotor tilt may cause yaw loads on the FOWT, specifically for a spar-type floater [1]. A spar FOWT has been shown to have an increased yaw response when exposed to a less coherent turbulent wind inflow [2, 3,

4]. A less spatially-coherent wind inflow for lateral separations results in higher twisting moments about the spar wind turbine's vertical axis and thus creates greater yaw loads and motion responses [2, 3]. Furthermore, different levels of turbulent wind energy associated with various atmospheric conditions are also found to affect the yaw load and motion of a spar-type wind turbine [5, 6]. The two aspects of turbulent wind flow (spatial coherence and turbulent wind energy content) significantly contribute to the yaw responses since a spar-type FOWT has low resistance to yaw. Motivated by previous studies on a spar-type floating wind turbine [2, 3, 4, 5] and the fact that a semisubmersible FOWT also corresponds to long eigen-periods susceptible to wind excitation, we aim to investigate the response sensitivity of a semisubmersible FOWT to the variation in turbulent wind inflow. In the present study the responses of the DeepCwind from the OC4 project [7] is investigated under different turbulent wind inflow conditions.

2. Turbulent wind models

Turbulent wind is a random process which is complex to simulate. In common engineering design of wind turbines, standard guidelines such as IEC 61400-1 [8] are commonly used. In this standard, two wind spectral models are recommended for numerical simulations of turbulent wind fields for neutral atmospheric stability conditions: the Kaimal Spectra [9] with an Exponential Coherence, and the Mann Spectral Tensor Model [10]. A neutral atmospheric stability condition indicates no vertical temperature flux in the atmosphere, a condition not necessarily prevailing in the offshore atmospheric [9]. Over the ocean, there often exists significant temperature discrepancies between the sea water surface and the air, which results in enhanced vertical mixing under unstable atmospheric stability conditions [11]. The present offshore wind turbine design guidelines take into account wind spectral models for neutral atmospheric conditions only. A wind spectral model such as the Pointed-Blunt [12], which was derived based on wind measurement data from an offshore site, can be used to represent non-neutral atmospheric conditions.

The turbulent wind fields used in this study are simulated by focusing on two different aspects of turbulent wind: (1) variation in the spatial coherence, and (2) variation in the atmospheric stability. Variation in the spatial coherence is represented by simulated wind fields comparing the Kaimal and the Mann spectral models [8] for neutral atmospheric stability conditions. The Kaimal and Mann spectral models are equivalent in terms of turbulent energy, but not the spatial coherence [8]. Variation in the atmospheric stability is represented by wind fields simulated using the Pointed-Blunt spectral model [12] for progressively decreasing atmospheric stability from neutral to very unstable, assuming fixed spatial coherences for all stabilities.

2.1. Kaimal spectra

The Kaimal spectra was derived based on measured wind data in Kansas [9] and widely used to simulate turbulent wind fields. The adopted formulation of the single-sided one-point Kaimal spectra in the IEC 61400-1 is expressed as [8]:

$$\frac{fS_i(f)}{\sigma_i^2} = \frac{\frac{4fL_i}{U_{hub}}}{\left(1+\frac{6fL_i}{U_{hub}}\right)^{5/3}} \tag{1}$$

where
f: frequency (Hz)
i: velocity component index (u: longitudinal, v: lateral, and w: vertical)
S_i: velocity spectrum for each component i
σ_i: standard deviation of velocity component i (m/s), detailed in ref. [8]
L_i: integral length scale of velocity component i (m), detailed in ref. [8]
U_{hub}: mean wind speed at hub height (m/s)

The one-point spectra given in Eq. (1) is paired with an exponential coherence to compute the surrounding points' spectral properties of the u- wind component [8]:

$$Coh_{uu}(f,\Delta) = exp\left[-12\sqrt{\left(\frac{f\,\Delta}{U_{hub}}\right)^2 + \left(\frac{0.12\,\Delta}{L_u}\right)^2}\right] \tag{2}$$

where Δ is the separation distance, either lateral or vertical (m). As stated in the IEC 61400-1, Eq. (2) is applicable only for the longitudinal wind component u-, while coherence formulation for the lateral (v) and vertical (w) components are not given. In the TurbSim guideline [13], identity coherence is recommended for v- and w- components. However, in the absence of validated coherence values for v- and w- components, the present study utilizes Eq. (2) as the coherence formulation for v- and w- components as well.

2.2. Mann spectral tensor model

The Mann spectral tensor implies isotropic von Kármán spectra as the initial condition, and the presence of wind shear allows the isotropic flow transforms into anisotropic flow with time as the eddies' structure is stretched until they break [10]. The velocity component spectra for the Mann spectral tensor model as given in the IEC 61400-1 is [8]:

$$\frac{fS_i(f)}{\sigma_i^2} = \frac{{\sigma_{iso}}^2}{\sigma_i^2}\left(\frac{4\pi\ell f}{U_{hub}}\right)\Psi_{ij}\left(\frac{2\pi\ell f}{U_{hub}}\right) \tag{3}$$

where

Ψ_{ij}: autospectrum/cross-spectrum as a function of spectral tensor components, detailed in ref. [8]

σ_i^2: component variance (m^2/s^2)

σ_{iso}: 0.55 σ_u (m/s)

ℓ: 0.8 Λ_u, taken as 33.6 m

To account for the anisotropy, the shear parameter γ is added to the spectral tensor model so the model has three representative parameters in total: $\alpha\epsilon^{2/3}$ (a measure of the turbulent kinetic energy dissipation rate), ℓ, and γ [10]. A fit to the Kaimal spectral model in Eq. (1) gives the value of 3.9 for the shear parameter γ [8]. The coherence is then calculated as [10]:

$$Coh_{ij}(f,\Delta_y,\Delta_z) = \frac{\left|\Psi_{ij}(f,\Delta_y,\Delta_z)\right|^2}{S_i(f)S_j(f)} \tag{4}$$

with Δ_y and Δ_z are the separation distances respectively in the lateral and vertical directions with respect to the incoming wind inflow. The resulting coherences for lateral separations from Eq. (4) are much lower than those given in Eq. (2), especially at frequencies lower than 0.2 Hz [4]. The same applies to the involved co-coherences, which concern the in-phase, simultaneous action of turbulence across the considered separations.

2.3. Pointed-Blunt spectra

The Pointed-Blunt spectral model was derived based on two-year measured wind data from FINO1 platform [12]. The model is a one-point spectra presented in a similar form to the Kaimal spectra, except it is made up by a low-frequency part and a high-frequency part. Each of the parts has two floating parameters which depend on the atmospheric stability. The parameters are defined for the range of $-2 < \zeta < 2$; where ζ is the stability parameter = z/L_m, z is the measured height (m) and L_m is the Obukhov length (m). For the considered stability, from very stable (ζ=2) to neutral (ζ=0) and then very unstable (ζ=-2), the turbulent kinetic level increases progressively [12]. The Pointed-Blunt spectra is given as [12]:

$$\frac{fS_i(f)}{u_*^2} = \frac{{a_1}^i f}{\left(1 + {b_1}^i f\right)^{5/3}} + \frac{{a_2}^i f}{\left(1 + {b_2}^i f^{5/3}\right)} \quad (5)$$

where a_1^i, a_2^i, b_1^i, b_2^i are the floating parameters for different velocity component i (u: longitudinal, v: lateral, w: vertical), and u_* is the friction velocity (m/s). Here, the spectral model in Eq. (5) is paired with the exponential coherence given in Eq. (2) for u-, v-, and w- velocity components, which is adopted for all considered stability conditions.

3. Numerical simulations

Coupled SIMO-Riflex included in the Simulation Workbench for Marine Application (SIMA) is used as the main numerical simulation tool. By utilizing SIMO-Riflex and simulated wind fields as input, the load and motion responses of the OC4-DeepCwind wind turbine corresponding to different turbulent wind inflow conditions are computed and analyzed. Turbulent wind fields are generated accordingly for all load cases presented in Table 1 by means of TurbSim [13] for Kaimal spectral model, Mann Turbulence Generator [14] for Mann spectral model, and windSimFast [15] for Pointed-Blunt spectral model. These wind fields are produced in the form of moving 'turbulence box' in the direction of the incoming longitudinal wind u- component for the coupled SIMO-Riflex simulations.

3.1. Load case

The load cases (LCs) are divided into LC 1 (variation in the wind spatial coherence) and LC 2 (variation in the atmospheric stability). The turbulent intensity (TI) input for LC 1 are adopted to match the simulated values for LC 2a. Table 1 presents the simulated TI and other input values for all load cases. It can be observed from Table 1 that the TI values for LC 1 are close to the target values in LC 2a. A uniform mean wind profile is used for all load cases in Table 1. Additional simulations were performed for LC 2 by applying a stability-corrected logarithmic mean wind profile. This is discussed further in Subsection 4.5. A constant irregular wave input for all load cases is added to SIMA simulations using the JONSWAP spectra with significant wave height H_s = 4 m, peak period T_p = 8 s, and peakedness parameter γ = 3.3. The selected wave peak period is far shorter than the OC4-DeepCwind's first six eigen-periods. To minimize the uncertainties, each load case is simulated with six different random seeds and the simulation time step is taken as 0.01 s for a continuous 3600 s duration. Three mean wind speeds at hub height (U_{hub}) are considered for each load case given in Table 1, 8 m/s (below rated), 11.4 m/s (rated), and 15 m/s (above rated).

Table 1. Load case.

Load case	Wind model	Atmospheric stability	Coherence function	$\alpha\epsilon^{2/3}$ for 8, 11.4, 15 m/s	Input TI [%] for 8, 11.4, 15 m/s	Simulated TI [%] for 8, 11.4, 15 m/s
1a	Kaimal	Neutral (ζ=0)	Eq. (2)	-	5.95, 6.08, 6.16	5.77, 5.93, 6.03
1b	Mann[1]	Neutral (ζ=0)	Eq. (4)	0.00956, 0.0203, 0.036	5.95, 6.08, 6.16	5.83, 5.95, 6.01
2a	Pointed-Blunt	Neutral (ζ=0)	Eq. (2)	-		5.95, 6.08, 6.16
2b		Weakly unstable (ζ=-0.407)				6.0, 6.11, 6.18
2c		Unstable (ζ=-0.815)				6.51, 6.61, 6.67
2d		Very unstable (ζ=-1.63)				7.6, 7.74, 7.83

[1]other input parameters: ℓ=33.6m, γ=3.9

3.2. DeepCwind characteristics

The OC4-DeepCwind is the phase II of the Offshore Code Comparison Collaboration Continuation (OC4) project which adopts the NREL 5 MW offshore baseline turbine with a semisubmersible floater [7]. For shortness, the properties of the DeepCwind are not shown here but can be found in Robertson

et al. [7]. Figure 1a illustrates the DeepCWind semisubmersible wind turbine model in SIMA. The NREL 5 MW offshore baseline turbine has the cut-in, rated, and cut-out wind speeds of 3, 11.4, and 25 m/s respectively. The hub height is 90 m above mean seawater level and the rotor diameter is 126 m. The cut-in and rated rotor speeds are 6.9 and 12.1 rpm respectively. The simulated eigen-frequencies of the first eight modes of the OC4-DeepCwind compared to the OC4 code comparison are given in Figure 1b and show a good agreement.

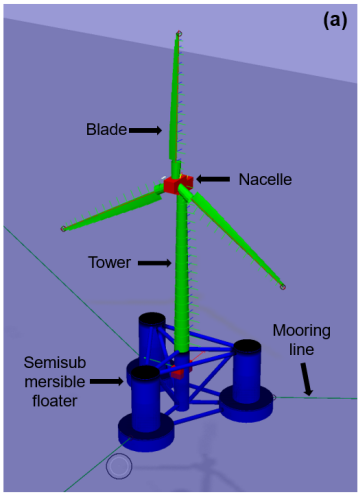

(b)

Mode	Simulated [Hz]	OC4 code comparison [7] in [Hz]
Surge	0.00875	0.0089-0.0105
Sway	0.00867	0.0089-0.0105
Yaw	0.0125	0.012-0.016
Pitch	0.038	0.0385-0.046
Roll	0.04	0.0385-0.049
Heave	0.055	0.054-0.056
1st tower side-side	0.44	0.38-0.5
1st tower fore-aft	0.45	0.38-0.5

Figure 1. (a) DeepCWind wind turbine model in SIMA and (b) the simulated eigen-frequencies.

4. Result

Structural response of the DeepCwind wind turbine with respect to the different turbulent wind inflows is studied in terms of the fatigue DEL. The 1-hour output time series of the considered stress resultants (in this case bending and torsional moment) are quantified as DEL and calculated by assuming an equivalent number of cycles n_{eq} of 10^7 during a 20-year lifetime:

$$DEL = \left(\frac{\Sigma N_i {S_i}^m}{n_{eq}} \right)^{1/m} \quad (6)$$

where N_i is the total number of cycles causing failure due to repeated stresses with a magnitude of S_i. The number of stresses in each bin is obtained from the Rainflow counting method [16]; m is the Wöhler exponent, here taken as 3 for steel material (tower) and 12 for fiberglass material (blade). The moments and the related fatigue damage are evaluated for the tower base fore-aft, tower base side-side, and the blade root flap-wise. The tower base and tower top torsional moments are also studied. In addition, the displacement responses (motions) are presented in the form of minimum, maximum, and standard deviation. The resulting force and displacement responses of the DeepCwind are discussed separately, when exposed to different turbulent wind conditions for neutral atmospheric stability with variable coherences (LC 1) and for different atmospheric stability conditions with constant coherences (LC 2).

4.1. Fore-aft response

It is noted that the tower base fore-aft moment DELs are increasing with wind speed. The tower base fore-aft moment power spectral density (PSD) plots are given in Figure 1 for the rated wind speed (11.4 m/s). The highest response is found for LC 2d (very unstable atmospheric condition) and is reduced as

turbulence level decreases as the atmospheric stability tends to neutral conditions (from LC 2d to LC 2a, Figure 2). Figure 2 shows that the tower base fore-aft moment response from LC 1b (Mann spectral model) are of a similar magnitude to those in LC 2d even though LC 1b considers neutral stability. However, the observed DEL difference between the highest (LC 2d) and the lowest (LC 2a) averaged tower base fore-aft DELs is only 3.4% (noted at 8 m/s), which is negligible. The highest excitation for the tower fore-aft moment is observed at the wave frequency as shown in Figure 2. In our simulations, the wave input was kept the same, and as a result there is negligible variation at the wave excitation for different load cases. Figure 3 shows the platform pitch response and it is noted that the platform pitch standard deviation is neither affected by variation in the spatial coherence nor influenced by variation in the turbulent energy content.

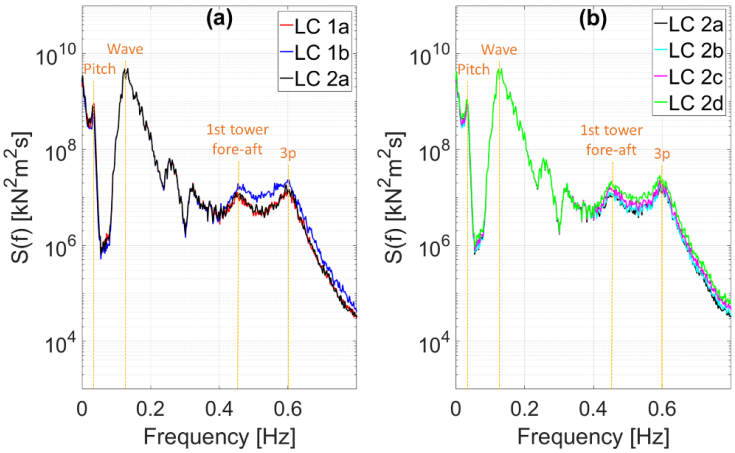

Figure 2. PSD of tower base fore-aft moment at the rated wind speed (11.4 m/s) for: (a) neutral stability and (b) different stability conditions.

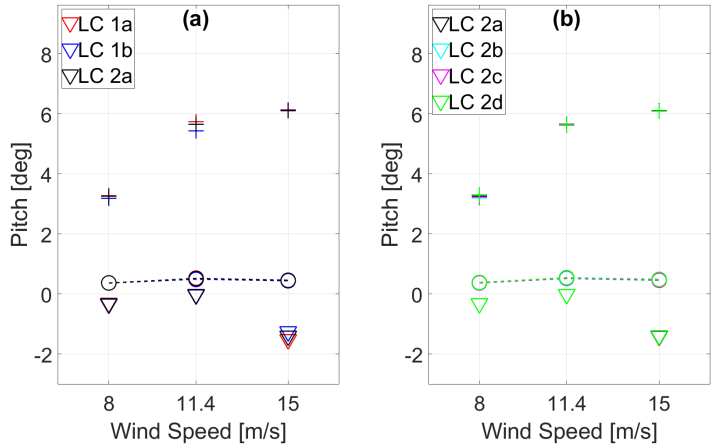

Figure 3. Platform pitch for: (a) neutral stability and (b) different stability conditions. Triangles indicate the minimum values, circles indicate the standard deviations, and plus indicate the maximum values.

4.2. Side-side response

Figure 4 gives the normalized DELs and Figure 5 gives the PSD response at 8 and 11.4 m/s of the tower base side-side for all load cases. Figure 4 shows that the DELs are the lowest at the rated wind speed (11.4 m/s) which might be caused by the influence of blade controller transition from a constant pitch angle to variable pitch angle. We note at wind speeds below rated, the tower base side-side DELs are primarily excited in the 1st tower side-side (Figure 5a). As the wind speeds approach rated and above, the excitation in the 1st tower side-side is reduced and excitation at the 3p frequency appears (Figure 5b). The highest averaged DEL is observed for LC 2d (very unstable conditions) and decreases as turbulence level decreases with the atmospheric conditions tend towards neutral (LC 2d to LC 2a, Figure 4b). However the DELs from LC 1b (Mann spectral model) are of similar magnitude to the DELs from LC 2d. The observed difference between the highest (LC 1b) and the lowest (LC 1a) averaged tower base side-side DEL is 30% at 15 m/s (Figure 4a).

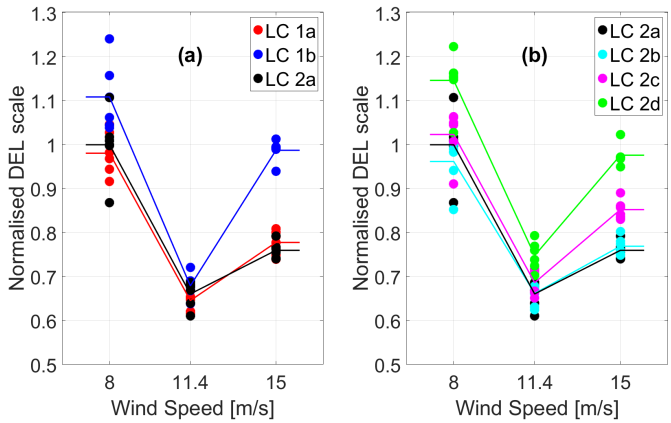

Figure 4. Normalized DELs of tower base side-side moment for: (a) neutral stability and (b) different stability conditions. Normalized by the values of LC 2a at 8 m/s.

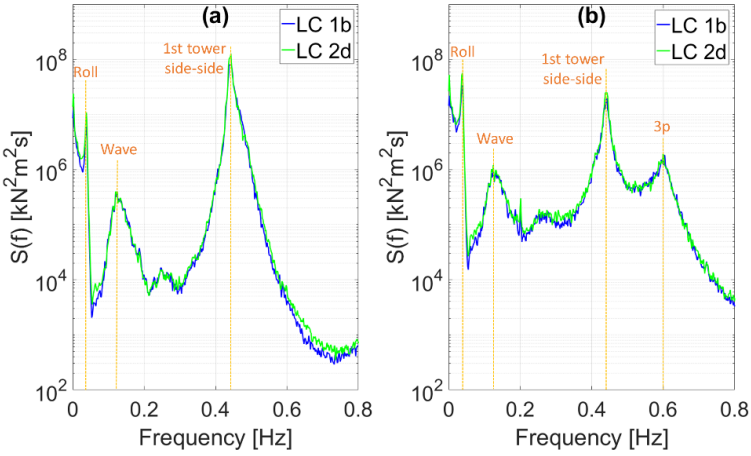

Figure 5. PSD of tower base side-side moment at: (a) 8 m/s and (b) 11.4 m/s.

Figure 6 presents the platform sway response and it shows a clear trend of sway response both with variation in the spatial coherence (Figure 6a) and the variation in atmospheric stability (Figure 6b). A less coherent turbulent wind inflow (LC 1b) results in larger sway, whereas the platform sway is decreasing gradually as the atmospheric conditions tend towards neutral (from LC 2d to LC 2a). The platform roll response is not shown here but it is noted that the platform roll is decreasing gradually from very unstable (LC 2d) to neutral conditions (LC 2a), while no clear trend is observed for variation in the spatial coherence (LC 1).

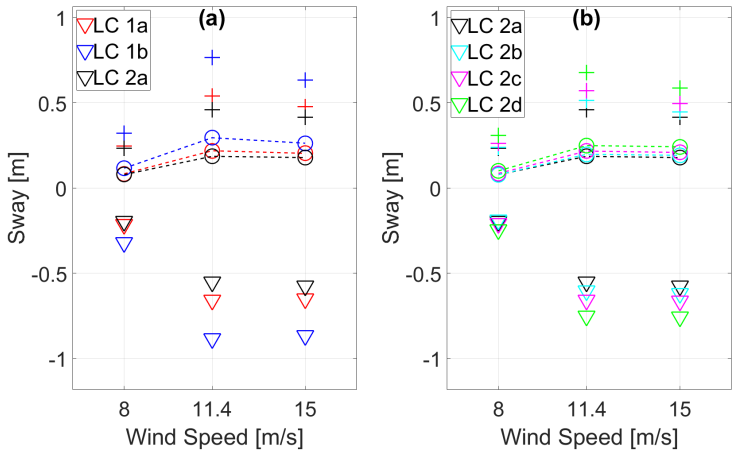

Figure 6. Platform sway for: (a) neutral stability and (b) different stability conditions. Triangles indicate the minimum values, circles indicate the standard deviation, and plus indicate the maximum values.

4.3. Yaw/torsion response

It is observed that the characteristics of the tower base torsional moment and the tower top torsional moment responses are very similar, therefore only tower top torsional moment is discussed here. In Figure 7, the normalized tower top torsional moment DELs are noted to increase with wind speed. Again, the highest averaged DEL is observed for LC 2d (very unstable conditions) and decreasing as the stability tends towards neutral atmospheric stability (from LC 2d to LC 2a, Figure 7b).

The DELs from LC 1b (Mann spectral model) are higher than the DELs under unstable conditions (LC 2c), due to the lower lateral coherence and the associated higher twisting moments about the turbine's vertical axis. This effect is also apparent for the platform yaw responses as presented in Figure 8, where the standard deviations from LC 1b even exceed the standard deviations from LC 2d. The difference between the highest (LC 2d) and the lowest (LC 2a) averaged tower top torsional moment DELs is 28% at 15 m/s (Figure 7b).

4.4. Blade root flap-wise bending

The blade root flap-wise moment DELs are seen to increase with wind speed. The difference between the highest (LC 1a) and the lowest (LC 1b) averaged blade root flap-wise moment DELs is 5.5% at 15 m/s. This is likely due to a more coherent wind inflow (for both vertical and lateral separations) in the LC 1a (Kaimal spectral model) compared to the wind flow defined by the Mann spectral model (LC 1b). With respect to the variation in the atmospheric stability (LC 2), the averaged DEL values do not vary significantly.

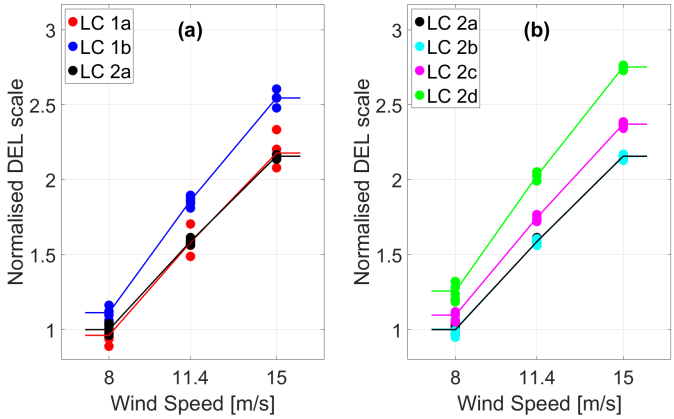

Figure 7. Normalized DELs of tower top torsional moment for: (a) neutral stability and (b) different stability conditions. Normalized by the values of LC 2a at 8 m/s.

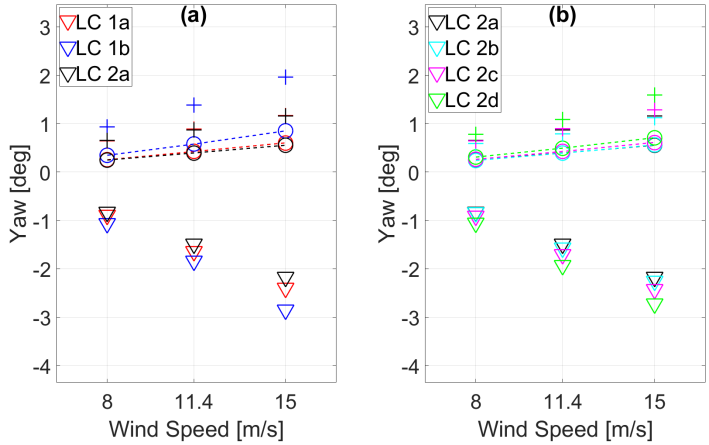

Figure 8. Platform yaw for: (a) neutral stability and (b) different stability conditions. Triangles indicate the minimum values, circles indicate the standard deviation, and plus indicate the maximum values.

4.5. Influence of the stability-corrected mean wind profile

The use of stability-corrected mean wind profile for LC 2 results in similar platform motions as shown in Subsection 4.1 to 4.4. The associated DELs with the use of stability-corrected mean wind profile for LC 2 also give similar DEL values to the simulations with a uniform mean wind profile. However, the observed average DEL values are lower by up to 8% for the tower base side-side moment, tower base torsional moment, and tower top torsional moment than those described in Subsection 4.1 to 4.4. The average blade root flap-wise DELs are shown to be increasing by 1.5% with the inclusion of stability-corrected mean wind profile as the stability shifts from neutral to very unstable. This is in agreement with Kretschmer et al. [18] who studied the measured blade root flap-wise DEL response from Alpha Ventus wind farm located near FINO1 platform, where the wind model used in LC 2 is derived from. Nonetheless, the 1.5% increase is negligible as there is very little wind shear for very unstable

conditions. Mean wind profile contribution could be more significant under stable atmospheric conditions which are not addressed in the present study.

5. Discussion

We note that the yaw and side-side responses of the DeepCwind are affected by different turbulent wind fields in a similar manner to the spar Hywind wind turbine from the OC3 project studied previously [3, 5]. The observed similar sensitivity of the yaw and side-side modes could be because the OC4 DeepCwind and the OC3 Hywind share the same turbine, the NREL 5 MW offshore baseline. When a FOWT experiences yaw errors between the rotor axis and the incoming wind direction (in the present case due to the prominent rotor yawing), side-side induced loads are triggered [17]. Such side-side induced loads' variation is then dependent on the turbine's properties i.e. rotor mass as well as the floater resistance to roll. From this study, the DeepCwind platform's roll is seen to have smaller deviations than those studied for the Hywind turbine [5].

The platform heave responses of the DeepCwind show negligible variation with different turbulence conditions because waves are the governing load for the platform heave translation [3]. In the present study, the wave input is kept constant for all load cases, therefore such conclusion is observed.

6. Conclusion

The yaw and the side-side response of the OC4 DeepCwind are demonstrated to be sensitive to the variation in the different turbulent wind inflow conditions, related to the spatial coherence and the atmospheric stability. The side-side response is largely triggered by the rotor-wind yaw error due to the rotor yawing. Other response components are seen to be less sensitive to the studied turbulent wind conditions. An 18% increase in the tower torsional moment and 30% increase for the tower side-side moment averaged DELs are observed for the simulated responses using the Mann spectral model (weaker coherence) than the simulated responses using the Kaimal spectral model (higher coherence). A 28% increase in the tower torsional moment and 28% increase for the tower side-side moment averaged DELs are observed for the simulated responses under very unstable conditions than the values obtained from neutral conditions.

Acknowledgement

The authors would like to express their gratitude to Dr. Lene Eliassen and Dr. Etienne Cheynet for their guidance and valuable knowledge through the completion of this work.

References

[1] DNV GL 2018 *DNV GL-ST-0119 Floating wind turbine structures* (DNV GL)
[2] Godvik M 2016 Influence of Wind Coherence on the Response of a Floating Wind Turbine *NORCOWE Science Meets Industry Stavanger*
[3] Bachynski E E and Eliassen L 2019 The Effects of Coherent Structures on the Global Response of Floating Offshore Wind Turbines *Wind Energy* **22** 219–38
[4] Doubrawa P, Churchfield M J, Godvik M and Sirnivas S 2019 Load response of a floating wind turbine to turbulent atmospheric flow *Applied Energy* **242** 1588–99
[5] Putri R M, Obhrai C and Knight J M 2019 Offshore Wind Turbine Loads and Motions in Unstable Atmospheric Conditions *J. Phys: Conf. Ser.* **1356** 012016
[6] Knight J M and C. Obhrai 2019 The Infulence of an Unstable Turbulent Wind Spectrum on the Loads and Motions on Floating Offshore Wind Turbines *IOP Conf. Ser: Materials Science and Engineering* **700** 012005
[7] Robertson A et al. 2014 Offshore code comparison collaboration continuation within IEA wind task 30: phase II results regarding a floating semisubmersible wind system *American Society of Mechanical Engineers Digital Collection*
[8] IEC 2005 Wind energy generation systems, Part 1: Design requirements (Geneva: IEC)
[9] Kaimal J C and Finnigan J J 1994 *Atmospheric boundary layer flows: their structure and*

measurement (New York: Oxford University Press)
[10] Mann J 1994 The Spatial Structure of Neutral Atmospheric Surface-Layer Turbulence *Journal of fluid mechanics* **273** 141–68
[11] Krogsæter O and Reuder J 2014 Validation of Boundary Layer Parameterization Schemes in the Weather Research and Forecasting (WRF) Model under the Aspect of Offshore Wind Energy Applications-Part II: Boundary Layer Height and Atmospheric Stability *Wind Energy* **18** 769–82
[12] Cheynet E, Bogunovic J B and Reuder J 2018 Velocity Spectra and Coherence Estimates in the Marine Atmospheric Boundary Layer *Boundary-Layer Meteorology* **169** 429–60
[13] Jonkman J 2016 *TurbSim User's Guide: Version 2.00.00* (Golden: NREL)
[14] Larsen T J and Hansen A M 2019 *How 2 HAWC2, the user's manual* (Risø: DTU Wind Energy)
[15] Cheynet E 2018 *Wind Field Simulation* [Online, accessed January 2019]
[16] Tatsuo E, Koichi M, Kiyohumi T, Kakuichi K and Masanori M 1974 Damage evaluation of metals for random or varying loading—three aspects of rain flow method *Mechanical Behavior of Materials* 21–4
[17] Kretschmer M, Schwede F, Guzmán R F, Lott S and Cheng P W 2018 Influence of atmospheric stability on the load spectra of wind *J. Phys: Conf. Ser.* **1037** 052009
[18] Jonkman J and Matha D 2010 *Quantitative comparison of the responses of three floating platforms No. NREL/CP-500-46726* (Golden: NREL)

Paper 4
Turbulence in a coastal environment: the case of Vindeby

*Rieska Mawarni Putri[1], Etienne Cheynet[2], Charlotte Obhrai[1], and Jasna Bogunovic Jakobsen[1]
[1]Department of Mechanical and Structural Engineering and Materials Science, University of Stavanger, Norway; [2]Geophysical Institute and Bergen Offshore Wind Centre (BOW), University of Bergen, Norway

Wind Energ. Sci., 7, 1693–1710, 2022
https://doi.org/10.5194/wes-7-1693-2022

Open Access WIND ENERGY SCIENCE

Turbulence in a coastal environment: the case of Vindeby

Rieska Mawarni Putri[a], Etienne Cheynet[b], Charlotte Obhrai[a], and Jasna Bogunovic Jakobsen[a]

[a]Department of Mechanical and Structural Engineering and Materials Science,
University of Stavanger, 4036 Stavanger, Norway
[b]Geophysical Institute and Bergen Offshore Wind Centre (BOW), University of Bergen, 5007 Bergen, Norway

Correspondence: Rieska Mawarni Putri (rieska.m.putri@uis.no)

Received: 16 July 2021 – Discussion started: 23 August 2021
Revised: 3 July 2022 – Accepted: 18 July 2022 – Published: 11 August 2022

Abstract. The one-point and two-point power spectral densities of the wind velocity fluctuations are studied using the observations from an offshore mast at Vindeby Offshore Wind Farm, for a wide range of thermal stratifications of the atmosphere. A comparison with estimates from the FINO1 platform (North Sea) is made to identify shared spectral characteristics of turbulence between different offshore sites. The sonic anemometer measurement data at 6, 18, and 45 m a.m.s.l. (above mean sea level) are considered. These heights are lower than at the FINO1 platform, where the measurements were collected at heights between 40 and 80 m. Although the sonic anemometers are affected by transducer-flow distortion, the spectra of the along-wind velocity component are consistent with those from FINO1 when surface-layer scaling is used, for near-neutral and moderately diabatic conditions. The co-coherence of the along-wind component, estimated for vertical separations under near-neutral conditions, matches remarkably well with the results from the dataset at the FINO1 platform. These findings mark an important step toward more comprehensive coherence models for wind load calculation. The turbulence characteristics estimated from the present dataset are valuable for better understanding the structure of turbulence in the marine atmospheric boundary layer and are relevant for load estimations of offshore wind turbines. Yet, the datasets recorded at Vindeby and FINO1 cover only the lower part of the rotor of state-of-the-art offshore wind turbines. Further improvements in the characterisation of atmospheric turbulence for wind turbine design will require measurements at heights above 100 m a.m.s.l.

1 Introduction

In the early 1990s, the first generations of offshore wind farms were commissioned to test the viability of extracting wind power in the marine atmospheric boundary layer (MABL). The first was Vindeby Offshore Wind Farm, which provided electricity to around 2200 homes during its 25 years of operation, with a total generated power of 243 GW h (Power Technology, 2020). The project was deemed successful and marked the beginning of the offshore wind sector.

Not only was the Vindeby project the first offshore wind farm, but also it provided precious information on meteorological conditions in the MABL using offshore and onshore meteorological masts. The data collected have been used to study the characteristics of the mean wind speed profile under various atmospheric conditions (Barthelmie et al., 1994; Barthelmie, 1999). The masts were also instrumented with 3D sonic anemometers to study turbulence, but these data were used in a limited number of studies only (e.g. Mahrt et al., 1996, 2001).

The characteristics of the MABL differ from the overland atmospheric boundary layer (ABL) due to the large proportion of non-neutral atmospheric stability conditions (Barthelmie, 1999; Archer et al., 2016) and low roughness lengths. Since the 2010s, several studies have indicated that diabatic wind conditions may significantly affect the fatigue life of offshore wind turbine (OWT) components (Sathe et al., 2013; Hansen et al., 2014; Holtslag et al., 2016; Doubrawa et al., 2019; Nybø et al., 2020; Putri et al., 2020). Recent measurements from the first commercial floating wind farm (Hywind Scotland) have even shown the di-

rect influence of atmospheric stability on the floater motions (Jacobsen and Godvik, 2021). Diabatic conditions are more likely to affect floating wind turbines than bottom-fixed ones as the first few eigenfrequencies of large floating wind turbines are close to or below 0.02 Hz (Nielsen et al., 2006), which is the frequency range mainly affected by the thermal stratification of the atmosphere. To model properly the wind load for wind turbine design, a better understanding of the spectral structure of turbulence in the MABL is necessary, which addresses partly the first of the three great challenges in the field of wind energy (Veers et al., 2019).

The limitations of current guidelines for offshore turbulence modelling, such as IEC 61400-1 (2005), have been highlighted in the past (Cheynet et al., 2017, 2018). Site-specific measurements advised by IEC 61400-1 (2005) are related to the mean flow and integral turbulence characteristics. However, for the spectral characteristics, appropriate scaling can be used to display universal shapes over specific frequency ranges. In this regard, the present study addresses similar challenges to those discussed by Kelly (2018) but focuses on some specific aspects not covered by the spectral tensor of homogeneous turbulence (Mann, 1994). Firstly, the low-frequency fluctuations are generally underestimated by the uniform-shear model, especially under convective conditions (De Maré and Mann, 2014; Chougule et al., 2018). Secondly, the version of the uniform-shear model (Mann, 1994) used within the field of wind energy does not account for the blocking by the ground, which may lead to an overestimation of the co-coherence of both the along-wind and the vertical wind components for near-neutral conditions (Cheynet, 2019). Thus, the co-coherence modelling using the uniform-shear model (Mann, 1994) is not discussed further in the present study.

Using the unexplored sonic anemometer data from the Vindeby database, this study looks at the characteristics of offshore turbulence in the frequency space. The objective is to quantify the similarities between these characteristics and those identified at FINO1 (Cheynet et al., 2018). Such a comparison is relevant to establishing new offshore wind turbulence models that can be used to improve the design of future multi-megawatt offshore wind turbines. Whereas the measurement data from FINO1 were obtained 40 km away from the shore, at heights between 40 m and 80 m a.m.s.l. (above mean sea level), those from the Vindeby database were collected only 3 km from the coast and at heights between 6 m and 45 m a.m.s.l. Therefore, the two datasets offer a complementary description of wind turbulence above the sea.

The present study is organised as follows: Sect. 2 describes the instrumentation and the site topography. Section 3 summarises the data processing, the assumptions, and the models used to study the spectral characteristics of turbulence. Section 4 presents the methodology used to assess the data quality and selection of stationary velocity data. Section 5 first evaluates the applicability of surface-layer scaling for the anemometer records at 6 m a.m.s.l. Then, the one-point velocity spectra and co-coherence estimates from Vindeby are compared with predictions from semi-empirical models which are based on FINO1 observations (Cheynet et al., 2018) to assess the similarities of the spectral characteristics between the two sites. Finally, the applicability of the Vindeby database to the design of an adequate turbulence model for offshore wind turbines is discussed in Sect. 5.5.

2 Instrumentation and site description

Vindeby Offshore Wind Farm operated in Denmark from 1991 to 2016 and was decommissioned in 2017. It was located 1.5 to 3 km from the northwestern coast of the island of Lolland (Fig. 1). Due to its location, Vindeby may be regarded as a coastal site instead of an offshore one. Vindeby has a flat topography with an average elevation of under 11 m a.m.s.l., whereas the water depth around the wind farm ranges from 2 to 5 m (Barthelmie et al., 1994). As pointed out by Johnson et al. (1998), the average significant wave height H_s at Vindeby is under 1 m. The water depth increases from around 3 m in the proximity of the wind farm up to approximately 20 m away from the northern side of the wind farm.

The wind farm comprised 11 Bonus 450 kW turbines arranged in two rows with 300 m spacing along the 325–145° line and three meteorological masts (Fig. 2). The three masts were Land Mast (LM), Sea Mast South (SMS), and Sea Mast West (SMW), and the latter two were placed offshore (Fig. 2). Both SMS and SMW were installed in 1993 and were decommissioned in 2001 and 1998, respectively. Measurements from LM and SMS were used by Barthelmie (1999) to assess the influence of the thermal stratification of the atmosphere on coastal wind climates. The present study considers only wind measurements from SMW due to the availability of the data.

SMW was a triangular lattice tower with a height of 48 km a.m.s.l. as sketched in Fig. 3. The booms on the SMW were mounted on both sides of the tower at 46 and 226° from the north and are referred to as the northern and southern boom, respectively. The booms' length ranged from 1.6 to 4 m, and their diameter was 50 mm (Barthelmie et al., 1994). Three F2360a Gill three-axis ultrasonic anemometers (SAs) were mounted on the southern booms at 45, 18, and 6 m a.m.s.l. and operated with a sampling rate of 20 Hz. Two Risø P2021 resolver wind vanes with P2058 wind direction transmitters were located on the northern booms at 43 m and 20 m a.m.s.l. using a sampling frequency of 5 Hz. The height of the vanes' centres above the boom was 600 mm. There were seven cup anemometers mounted on SMW as shown in Fig. 3; however, their measurements were not used here. The air temperature at 10 m a.m.s.l. was recorded using a Risø P2039 PT 100 sensor. The sea surface elevation η was measured using an acoustic wave recorder (AWR) placed on the seabed, 30 m away from SMW, at a depth of 4 m (Johnson

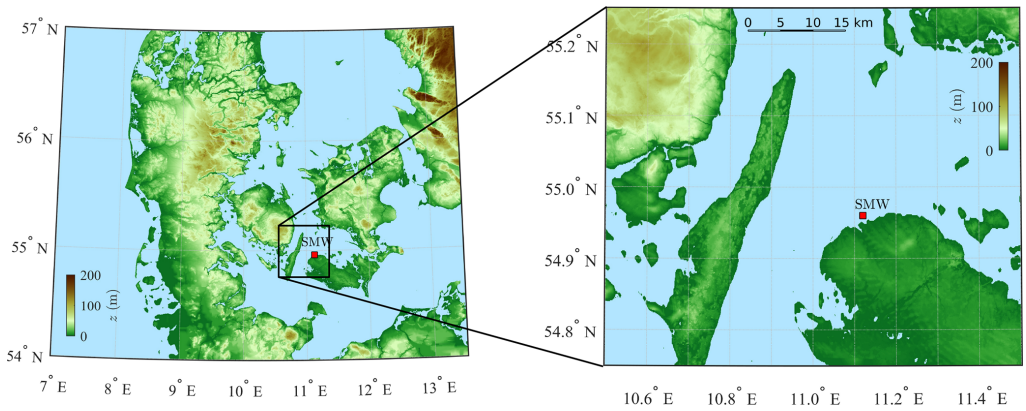

Figure 1. Digital elevation model of southern Denmark showing the location of Sea Mast West (SMW), in a sheltered flat coastal environment. Only the wind from 220 to 330° is considered for SMW.

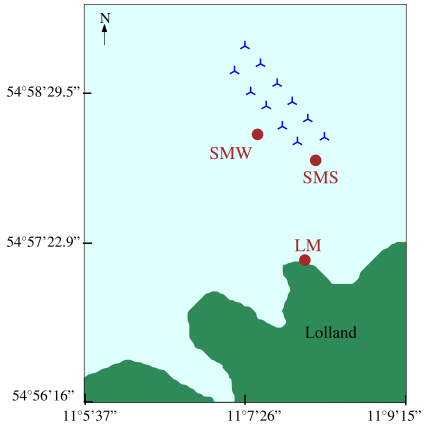

Figure 2. Vindeby Offshore Wind Farm layout with circles marking the position of the masts: SMW, SMS, and LM. SMW is located approximately 1.5 km from Lolland.

et al., 1998). The sea surface elevation data were recorded at a sampling frequency of 8 Hz but stored with a sampling frequency of 20 Hz. The data collected from SMW were transferred to LM using an underwater fibre optic link and stored as time series of 30 min duration. Such a duration is appropriate to study turbulence in coastal and offshore areas (Dobson, 1981). Therefore, the flow characteristics studied herein are based on the averaging time of 30 min.

The fetch around SMW comprises open sea, land, and mixed fetch as shown in Fig. 1. The so-called sea fetch is considered when the wind blows from 220 to 90°, with a fetch distance of up to 135 km for the sector ranging from 345 to 355°. The direction sectors from 0–50° are those most affected by flow distortion due to the presence of the mast (Barthelmie et al., 1994). Furthermore, the flow from 335–110° might be affected by the wake effects from the wind farm. To exclude the flow disturbed by the presence of the mast and wind turbine wakes and/or internal boundary layers due to roughness changes, only the flow from 220–330° is considered in the present study, which represents 40 % of the velocity data recorded in 1994 and 1995 at SMW. The surface roughness z_0 within the 247-to-292° direction varies with the mean wind speed from 0.00011 to 0.0012 m (Johnson et al., 1998). A more detailed description of the other directional sectors is given by Barthelmie et al. (1994).

3 Theoretical background

3.1 Monin–Obukhov theory

The along-wind, cross-wind, and vertical velocity components are denoted as u, v, and w, respectively. Each component is split into a mean ($\overline{u}$, $\overline{v}$, $\overline{w}$) and fluctuating part (u', v', w'). In flat and homogeneous terrain, the flow is fairly horizontal; i.e. $\overline{v}$ and $\overline{w}$ are approximatively zero. Here, the fluctuating components are assumed to be stationary, Gaussian, ergodic random processes (Monin, 1958).

Although the u component drives the wind turbine's rotor fatigue loads, proper modelling of the v component in terms of power spectral density (PSD) and root coherence may be necessary for skewed flow conditions, which can occur because of a large wind direction shear (Sanchez Gomez and Lundquist, 2020) or wind turbine yaw error (Robertson et al., 2019). To estimate a wind turbine's fatigue loads, the vertical velocity component is likely more relevant in complex terrain than offshore (Mouzakis et al., 1999). Nevertheless, this component is studied here for the sake of completeness. Also, the vertical velocity component provides precious information on the sonic anemometer flow distortion (Cheynet

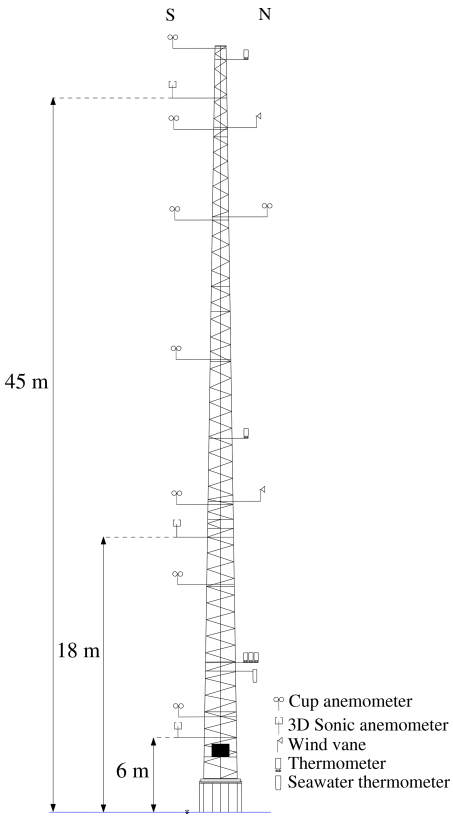

Figure 3. Sketch of the atmospheric instrumentation at SMW. The sonic anemometers are located in the southern boom "S" oriented at 226° from the north.

et al., 2019; Peña et al., 2019). The vertical velocity component is also necessary to assess the atmospheric stability using the eddy covariance method and facilitates the study of the waves' influences on the velocity data recorded by the sonic anemometers (e.g. Benilov et al., 1974).

In the atmospheric surface layer, where Monin–Obukhov similarity theory (MOST) generally applies, the scaling velocity is the friction velocity u_*, whereas the scaling lengths are the height z above the surface and the Obukhov length L (Monin and Obukhov, 1954), defined as

$$L = -\frac{u_*^3 \overline{\theta}_v}{g\kappa\left(\overline{w'\theta'_v}\right)}, \tag{1}$$

where $\overline{\theta}_v$ is the mean virtual potential temperature, $g = 9.81\,\mathrm{m\,s^{-2}}$ is the gravitational acceleration, $\kappa \approx 0.4$ is the von Kármán constant (Högström, 1985), and $\overline{w'\theta'_v}$ is the vertical flux of virtual potential temperature. For a given height z above the surface, the non-dimensional stability parameter $\zeta = z/L$ is used herein to classify the thermal stratification of the atmosphere.

While θ'_v can be fairly well approximated by the fluctuating sonic temperature measurement (Schotanus et al., 1983; Sempreviva and Gryning, 1996), the mean value $\overline{\theta}_v$ could not be reliably obtained from the sonic anemometers deployed on SMW (Kurt Hansen, personal communication, 2020). Therefore, $\overline{\theta}_v$ was obtained using the absolute temperature recorded from the Risø P2039 PT 100 sensor at 10 m a.m.s.l., which was converted into the virtual potential temperature using the pressure data from LM and assuming an air relative humidity of 90 % near the sea surface (Stull, 1988). The air pressure data from LM are used due to the absence of air pressure data at SMW and SMS.

Since the covariance between the cross-wind and the vertical component may not be negligible in the MABL (Geernaert, 1988; Geernaert et al., 1993), the friction velocity u_* is computed as suggested by Weber (1999); that is

$$u_* = \sqrt[4]{\overline{u'w'}^2 + \overline{v'w'}^2}. \tag{2}$$

A common approach to assess the applicability of MOST is to study the non-dimensional mean wind speed profile ϕ_m defined as

$$\phi_m\left(\frac{z}{L}\right) = \frac{\kappa z}{u_*}\frac{\partial \overline{u}}{\partial z} \tag{3}$$

as a function of the atmospheric stability (Kaimal and Finnigan, 1994). In the following, ϕ_m is empirically modelled as by Högström (1988):

$$\phi_m \approx \begin{cases} (1 + 15.2|\zeta|)^{-1/4}, & -2 \le \zeta < 0, \\ 1 + 4.8(\zeta), & 0 \le \zeta \le 1. \end{cases} \tag{4}$$

The validity of Eq. (4) is assessed for each anemometer in Sect. 5.1. It should be noted that the presence of waves, especially swell, may invalidate MOST in the first few metres above the surface (Edson and Fairall, 1998; Sjöblom and Smedman, 2003b; Jiang, 2020), and this possibility will be discussed in Sect. 5.2. Under convective conditions, the validity of MOST may also be questionable if the fetch is only a few kilometres long due to the presence of internal boundary layers (Jiang et al., 2020). In the present case, the choice of wind directions from 220 to 330° limits strongly the possibility that internal boundary layers affect the velocity measurements.

3.2 One-point turbulence spectrum

Appropriate modelling of the one-point velocity spectrum is required to compute reliably the dynamic wind-induced response and the power production of wind turbines (Sheinman and Rosen, 1992; Hansen and Butterfield, 1993). Integral turbulence characteristics, especially the turbulence in-

tensity, are not always appropriate for turbulence characterisation (Wendell et al., 1991), which motivates the study of the spectral characteristics of turbulence herein.

Following Kaimal et al. (1972), the normalised surface-layer one-point velocity spectra express a universal behaviour in the inertial subrange:

$$\frac{fS_{\mathrm{u}}(f)}{u_*^2\phi_\epsilon^{2/3}} \simeq 0.3 f_{\mathrm{r}}^{-2/3} \text{ at } f_{\mathrm{r}} \gg 1, \tag{5}$$

$$\frac{fS_{\mathrm{v}}(f)}{u_*^2\phi_\epsilon^{2/3}} \approx \frac{fS_{\mathrm{w}}(f)}{u_*^2\phi_\epsilon^{2/3}} \simeq 0.4 f_{\mathrm{r}}^{-2/3} \text{ at } f_{\mathrm{r}} \gg 1, \tag{6}$$

where $f_{\mathrm{r}} = fz/\overline{u}$ and f is the frequency; S_{u}, S_{v}, and S_{w} are the velocity spectra for the along-wind, cross-wind, and vertical velocity components, respectively; and ϕ_ϵ is the non-dimensional turbulent kinetic energy dissipation rate (Wyngaard and Coté, 1971). The latter is given by

$$\phi_\epsilon = \frac{\kappa z \epsilon}{u_*^3}, \tag{7}$$

where ϵ is the turbulent kinetic energy dissipation rate.

In the present case, ϕ_ϵ is modelled as (Kaimal and Finnigan, 1994)

$$\phi_\epsilon^{2/3} = \begin{cases} 1 + 0.5|\zeta|^{2/3}, & \zeta \le 0, \\ (1+5\zeta)^{2/3}, & \zeta \ge 0. \end{cases} \tag{8}$$

3.3 The coherence of turbulence

The coherence of turbulence describes the spatial correlation of eddies. The root coherence is defined as the normalised cross-spectral density of turbulence and is a complex-valued function. The real part of the root coherence, known as the co-coherence, is one of the governing parameters for the structural design of wind turbines (IEC 61400-1, 2005). At vertical separations, the co-coherence γ_i, where $i = \{u, v, w\}$, is defined as

$$\gamma_i(z_1, z_2, f) = \frac{Re\{S_i(z_1, z_2, f)\}}{\sqrt{S_i(z_1, f) S_i(z_2, f)}}, \tag{9}$$

where $S_i(z_1, z_2, f)$ is the two-point cross-spectral density between heights z_1 and z_2, whereas $S_i(z_1, f)$ and $S_i(z_2, f)$ are the one-point spectra estimated at heights z_1 and z_2, respectively.

Davenport (1961) proposed an empirical model to describe the co-coherence for vertical separations, which depends only on a decay parameter c^i and a reduced frequency n:

$$\gamma_i(n) \approx \exp\left(-c^i n\right), \tag{10}$$

$$n = \frac{2 f d_z}{\overline{u}(z_1) + \overline{u}(z_2)}, \tag{11}$$

where $d_z = |z_1 - z_2|$. For three heights $z_1 > z_2 > z_3$ such that $z_1 - z_2 = z_2 - z_3$, Davenport's model predicts that $\gamma_i(z_1, z_2, f)$ and $\gamma_i(z_2, z_3, f)$ collapse onto a single curve when expressed as a function of n. This behaviour, referred to as Davenport's similarity herein, is questioned by Bowen et al. (1983) for vertical separations and by Kristensen et al. (1981) and Sacré and Delaunay (1992) for lateral separations.

Bowen et al. (1983) modified the Davenport model by assuming that c^i was a linear function of the distance; i.e.

$$c^i = c_1^i + \frac{2c_2^i d_z}{(z_1 + z_2)}, \tag{12}$$

where c_1^i and c_2^i are constants. Equation (12) reflects the blocking by the ground or the sea surface, which leads to an increase in the co-coherence with measurement height. This equation implies that the co-coherence decreases more slowly than predicted by the Davenport model if measurements are conducted far from the surface and at short separations. On the other hand, the co-coherence may decrease faster than predicted by the Davenport model if the measurements are associated with large separation distances. This implies that fitting the Davenport model to measurements with short or large separations may lead to an inadequate design of wind turbines.

The model by Bowen et al. (1983) was further modified by Cheynet (2019) by including a third decay parameter c_3^i to account for the fact that the co-coherence cannot reach values of 1 at zero frequency unless the separation distance is zero. This led to the following three-parameter co-coherence function, which is herein referred to as the modified Bowen model:

$$\gamma_{ii}(z_1, z_2, f) = \exp(-f_a)\exp(-f_b), \tag{13}$$

$$f_a = \frac{|z_2 - z_1|}{\overline{u}(z_1, z_2)} \sqrt{\left(c_1^i f\right)^2 + \left(c_3^i\right)^2}, \tag{14}$$

$$f_b = \frac{2c_2^i f |z_2 - z_1|^2}{(z_1 + z_2)\overline{u}(z_1, z_2)}. \tag{15}$$

It should be noted that both c_1^i and c_2^i are dimensionless, whereas c_3^i has the dimension of the inverse of a time. Following Kristensen and Jensen (1979), $c_3^i \propto 1/T$, where T is a timescale of turbulence. Therefore, low values of c_3^i are associated with a co-coherence converging toward 1 at low frequencies for which the separation distance is small compared to a typical turbulence length scale. The rotor diameter of multi-megawatt OWTs commissioned after 2015 in the North Sea is slightly larger than 150 m. For such structures, assuming $c_3^i \approx 0$ may no longer be appropriate.

IEC 61400-1 (2005) recommends the use of two empirical coherence formulations. The first one was derived based on the exponential coherence proposed by Davenport (1961), which read as

$$\gamma_{\mathrm{u}}(f,d_z)=\exp\left\{-12\left[\sqrt{\left(\frac{f\,d_z}{\overline{u}_{\mathrm{hub}}}\right)^2+\left(0.12\frac{d_z}{8.1L_{\mathrm{c}}}\right)^2}\right]\right\}, \quad (16)$$

where $\overline{u}_{\mathrm{hub}}$ is the mean wind speed at the hub height and

$$L_{\mathrm{c}}=\begin{cases}0.7z, & z\le 60\,\mathrm{m},\\ 42\,\mathrm{m}, & z\ge 60\,\mathrm{m}.\end{cases} \quad (17)$$

The second coherence model was derived based on a spectral tensor of homogeneous turbulence (Mann, 1994) but is not described in detail here. Further assessments of this model can be found in, for example, Mann (1994), Saranyasoontorn et al. (2004), and Cheynet (2019).

4 Data processing

Sonic anemometer data monitored continuously from May 1994 to July 1995 were selected. No data were collected in July and October 1994, leading to 13 months of available records. The sonic anemometer at $z = 18$ m was chosen as the reference sensor throughout the data processing. The measurements at $z = 45$ m were associated with higher measurement noise than at the other two heights. Although this noise was almost negligible at wind speeds above $10\,\mathrm{m\,s^{-1}}$, it was visible in the velocity records at low wind speeds.

Since the wind sensors at 6, 18, and 45 m a.m.s.l. were omnidirectional sonic anemometers, they were prone to flow distortion by the transducer. This flow distortion was investigated in terms of friction velocity estimated from the asymmetric solent anemometer mounted at 10 m a.m.s.l., between May and September 1994 only due to data availability. The corrected friction velocities for the sensors at 6, 18, and 45 m were computed using the data at 10 m, as elaborated in Appendix B. When using the corrected friction velocity, no significant improvement was found for the ensemble-averaged normalised PSD estimates. It was then concluded that for the relatively narrow selected sector (220–330°), the application of an ensemble averaging limits the influence of the transducer-induced flow distortion on the spectral flow characteristics. Therefore, it was decided not to apply a correction for both friction velocity and the Obukhov length to avoid over-processing the data.

Both the double-rotation technique and the sectoral planar fit (PF) method (Wilczak et al., 2001) were considered to correct the tilt angles of the SAs. The choice of the algorithm relied on a comparison between the friction velocity u_* estimated using Eq. (2) and the method by Klipp (2018), which does not require any tilt correction. The latter method provides an estimate $u_{*\mathrm{R}}$ of the friction velocity using the eigenvalues of the Reynolds stress tensor. Following this comparison, the double-rotation technique was found to provide, in the present case, slightly more reliable results than the PF algorithm (see Appendix A). It should be noted that this finding is likely specific to the Vindeby dataset as the planar fit method usually provides better estimates of the turbulent fluxes (Wilczak et al., 2001).

The time series were sometimes affected by outliers. Here, the outliers were identified using a moving median window based on a 5 min window length. The same outlier detection algorithm was also used for the sea surface elevation data but with a moving window of 180 s. The local median values were then used to compute the median absolute deviation (MAD), as recommended by Leys et al. (2013). Data located more than five MADs away from the median were replaced with NaNs (NaN denotes "not a number"). The generalised extreme Studentised deviate test (Rosner, 1983) was also assessed to detect outliers but did not bring significant improvements. When the number of NaNs in the time series was under 5 %, the NaNs were replaced using a non-linear interpolation scheme based on the inpainting algorithm by D'Errico (2004) with the "spring" method. A more adequate but slower approach using autoregressive modelling (Akaike, 1969) was also applied but yielded a similar conclusion and therefore was not used. Time series containing more than 5 % of NaNs were dismissed. Although other spike detection and interpolation algorithms exist in the literature (e.g. Hojstrup, 1993), the approach adopted in this study was found to provide an adequate trade-off between computation time and accuracy.

To assess the first- and second-order stationarity of the velocity recordings, the moving mean and the moving standard deviation of the along-wind component were calculated using a window length of 10 min. The time series were considered stationary when the two following criteria were fulfilled: (1) the maximum absolute relative difference between the moving mean and the static mean was lower than a threshold value of 20 %; (2) for the moving standard deviation, the maximum absolute relative difference was also used with a threshold value of 40 %. The choice of a larger threshold value for the moving standard deviation test is justified by the larger statistical uncertainty associated with the variance of a random process compared to its mean (Lumley and Panofsky, 1964).

Velocity records with an absolute value of skewness larger than 2 or a kurtosis below 1 or above 8 are likely to display an unphysical behaviour (Vickers and Mahrt, 1997) and were subsequently dismissed. The statistical uncertainties in the records were quantified as by Wyngaard (1973) and Stiperski and Rotach (2016):

$$a_{ii}^2=\frac{4z}{T\overline{u}}\left[\frac{\overline{i'^4}}{\sigma_i^4}-1\right], \quad (18)$$

$$a_{\mathrm{uw}}^2=\frac{z}{T\overline{u}}\left[\frac{\overline{(u'w')^2}}{u_*^4}-1\right], \quad (19)$$

$$a_{\mathrm{vw}}^2 = \frac{z}{T\overline{u}}\left[\frac{\overline{(v'w')^2}}{u_*^4} - 1\right], \tag{20}$$

where a_{ij} with $i, j = (u, v, w)$ is the uncertainty associated with the variance and covariance estimates. Time series with a large random error, i.e. $a_{ii} > 0.20$ or $a_{ij} > 0.50$ with $i \neq j$, were excluded.

The records with a mean wind speed below $5.0\,\mathrm{m\,s^{-1}}$ at 18 m a.m.s.l. were discarded. Assuming a logarithmic mean wind profile, a near-neutral atmosphere, and a roughness length z_0 of 0.0002 m (WMO, 2008), the corresponding mean wind speed at a typical offshore wind turbine hub height (90 m a.m.s.l.) is $5.7\,\mathrm{m\,s^{-1}}$. The present choice of a lower mean wind speed threshold is, therefore, consistent with the cut-in wind speed of large offshore wind turbines, which is $5.0\,\mathrm{m\,s^{-1}}$ at hub height. It also ensures a consistent comparison of the spectral characteristics of turbulence with the data collected at FINO1, where the lowest mean wind speed considered was $5.0\,\mathrm{m\,s^{-1}}$ at 80 m a.m.s.l.

The PSD estimates of the velocity fluctuations were evaluated using Welch's method (Welch, 1967) with a Hamming window, three segments, and 50 % overlap. The spectra were ensemble-averaged using the median of multiple 30 min time series that passed the data-quality tests described above and were smoothed by using bin averaging over logarithmically spaced bins. The co-coherence estimates were also computed using Welch's method but using eight segments and 50 % overlap to further reduce the statistical uncertainty.

Table 1 displays the percentage of samples at each measurement height that failed the data-quality assessment. It relies on initial data availability of 86 %, 97 %, and 86 % for the anemometers at 6, 18, and 45 m a.m.s.l., respectively. Following the criteria used in the data processing and Table 1, the percentages of data considered for the analysis were 69 %, 76 %, and 45 % at 6, 18, and 45 m a.m.s.l., respectively. These percentages correspond to 1566 time series of 30 min duration for the SA at 6 m, 1771 time series at 18 m, and 854 at 45 m. The data from SA at 45 m showed the highest portion of non-stationary and large statistical uncertainties compared to the other SAs. Furthermore, the SA at 45 m also contained the highest fraction of NaNs in the time series, due to a large number of outliers. The larger fraction of data removal for the anemometer at 45 m is attributed to the observed uncorrelated white noises in the signal. This measurement noise, which may be linked to the length of the cable joining the anemometer and the acquisition system, is usually small for wind speed above $10\,\mathrm{m\,s^{-1}}$. Therefore, it was decided not to filter it out using digital low-pass filtering techniques. Time series that were flagged as non-physical made up less than 5 % for each SA in the present dataset, likely because the test was applied after the outlier detection algorithm. The portion of non-stationary time series increased with height (see Table 1). Closer to the surface, the eddies are smaller and are less likely to be affected by the sub-mesospheric and mesospheric atmospheric motion, which contributes to non-stationary fluctuations (Högström et al., 2002).

Table 1. Percentage of the records between April 1994 and July 1995 from SMW that failed the data-quality assessment.

	6 m	18 m	45 m
NaNs > 5 %	5 %	< 1 %	22 %
Unphysical kurtosis and skewness	4 %	3 %	< 1 %
Non-stationary	9 %	15 %	19 %
Large statistical uncertainties	2 %	4 %	22 %

5 Results

5.1 Applicability of MOST

In the atmospheric surface layer, the friction velocity u_* is often assumed constant with the height (constant flux layer). However, Fig. 4 shows that the friction velocity is generally larger at 6 m than at the other two measurement heights, especially under stable conditions. The different friction velocity values at 6 m compared to 18 and 45 m were suspected to be due to the transducer-induced flow distortion and/or the contribution of the wave-induced stress to the total turbulent stress (Janssen, 1989; Tamura et al., 2018).

The applicability of MOST is assessed by studying ϕ_{m} as a function of ζ. The similarity relation describing the mean wind speed profile agrees well with the sonic anemometer measurements under all stability conditions except between the sensor at 6 m and 18 m a.m.s.l. at $\zeta > 0.3$. It should be noted that at 6 m a.m.s.l., the local estimate of ζ shows a much greater portion of near-neutral conditions than at 18 m a.m.s.l. The right panel of Fig. 5 does not show such a deviation, maybe because the friction velocity estimated at 45 m a.m.s.l. is slightly underestimated due to the high-frequency noise in the velocity records of the top sensor. This further justifies the use of the sonic anemometer at 18 m a.m.s.l. to estimate the non-dimensional stability parameter ζ.

The distribution of ζ as a function of the mean wind speed $\overline{u}$ is given in Fig. 6 for the sector between 220 and 330°. The majority (82 %) of the stationary record samples were associated with a wind speed between 7–15 $\mathrm{m\,s^{-1}}$ at 18 m a.m.s.l. Non-neutral conditions are defined herein as situations where $|\zeta| > 0.1$. They represent 69 % of the samples at $\overline{u} < 12\,\mathrm{m\,s^{-1}}$ and 12 % at $\overline{u} \geq 12\,\mathrm{m\,s^{-1}}$. The distribution of the atmospheric stability conditions is in overall agreement with Barthelmie (1999) and Sathe and Bierbooms (2007) for the Vindeby site.

Strongly unstable or stable stratifications ($|\zeta| > 0.5$) made up only about 8 % of the total number of samples (Fig. 6). A low number of samples can lead to large uncertainties when comparing the flow characteristics between SMW and FINO1 for specific stability bins. Therefore, only stability

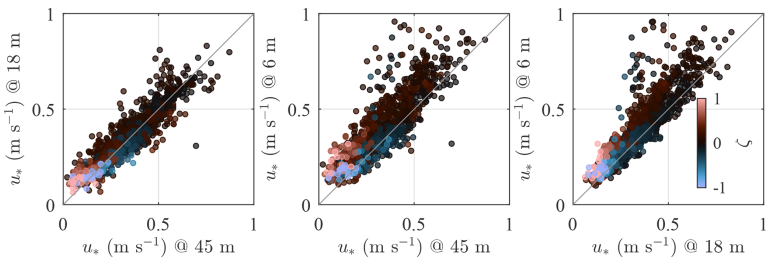

Figure 4. Friction velocity estimated by the three sonic anemometers on SMW for a wide range of stability conditions with $|\zeta| < 2$.

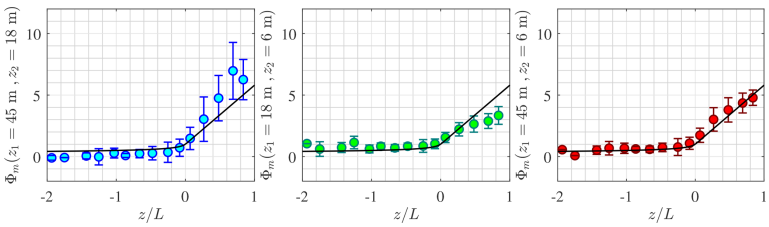

Figure 5. Variation in ϕ_m with the non-dimensional stability parameter ζ estimated from SA at 18 m a.m.s.l. The solid black line is Eq. (4), and the error bar represents the interquartile range.

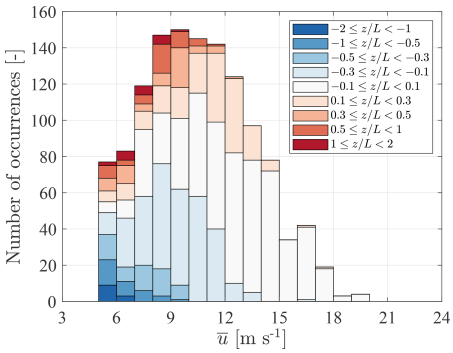

Figure 6. Stability distribution as a function of mean wind speed for the considered fetches (220–330°) at height $z = 18$ m.

conditions satisfying $|\zeta| \le 0.5$ are discussed herein unless indicated otherwise.

5.2 Wind–wave interactions

The fairly close proximity of the sensor at 6 m to the sea surface is used to study the potential influence of the wave boundary layer (WBL) (Sjöblom and Smedman, 2003a). This layer is also called the wave sublayer by Emeis and Türk (2009), who suggest that its depth is approximately $5H_s$, although there is no consensus on this value. The objective of this subsection is to identify whether the wave-induced turbulence can be detected in the velocity records at 6 m a.m.s.l.

The wave elevation data collected by the AWR near SMW are explored herein in terms of wind–wave interactions. A total of 925 high-quality samples collocated in time with the wind velocity data were identified. Each wave elevation record was 30 min long and corresponded to a wind direction between 220 and 330°. There exist methods to filter out the wave-induced velocity component from the turbulent velocity component (e.g. Hristov et al., 1998), but these methods are not addressed herein for brevity.

The interactions between wind turbulence and the sea surface were explored in terms of the co-coherence and the quad-coherence (the imaginary part of the root coherence) between the vertical velocity component w and the velocity of the wave surface $\dot{\eta} = \mathrm{d}\eta/\mathrm{d}t$. Similar approaches were adopted earlier by, for example, Grare et al. (2013) or Kondo et al. (1972) but using the coherence and without taking advantage of the ensemble average to reduce the systematic and random error, which are typically associated with the root-coherence function. In the present case, neither the co-coherence nor the quad-coherence between $\dot{\eta}$ and w differs significantly from zero for $H_s < 0.7$ m. For the sensor at 6 m a.m.s.l., a non-zero root coherence was discernible from the background noise at $0.7\,\mathrm{m} < H_s < 0.9\,\mathrm{m}$. The co-coherence and quad-coherence estimates were significantly different from zero for $H_s > 0.9$ m, as illustrated in Fig. 7, where the ensemble averaging of the 60 samples was applied to reduce the random error. The inset in Fig. 7 shows that

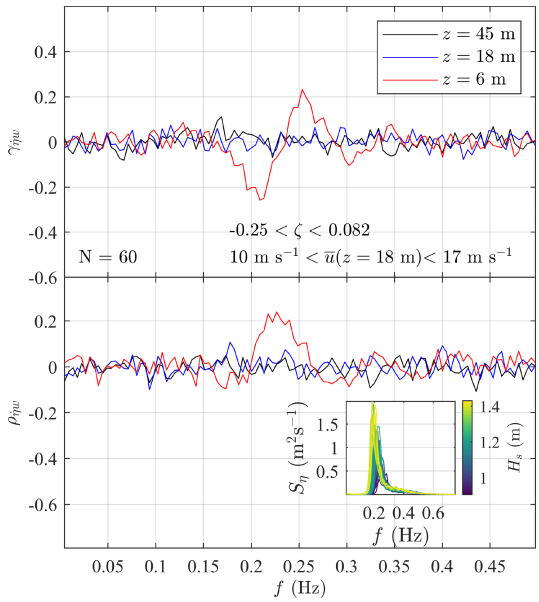

Figure 7. Co-coherence $\gamma_{\dot{\eta}w}$ and quad-coherence $\rho_{\dot{\eta}w}$ between the velocity of the wave surface $\dot{\eta}$ and the vertical wind velocity w from the three sonic anemometers on SMW. The inset shows the individual wave elevation spectra S_η associated with $H_s > 0.9$ m (60 samples) used to estimate $\gamma_{\dot{\eta}w}$ and $\rho_{\dot{\eta}w}$.

the selected records are characterised by a single spectral peak f_p located at frequencies between 0.20 and 0.25 Hz, which is the frequency range where the quad-coherence is substantially different from zero. The observed co-coherence and the quad-coherence at this frequency range show the 90° out-of-phase fluctuations between $\dot{\eta}$ and w, where the latter is lagging. The co-coherence and quad-coherence estimates between $\dot{\eta}$ and the horizontal wind component u were also investigated but were nearly zero for the three sonic anemometers on SMW.

The limited number of data showing a clear correlation between the velocity of the sea surface and the vertical wind component implies that the wave-induced turbulence has a limited impact on the anemometer records at 6 m. The influence of the sea surface elevation on the vertical turbulence was not clearly visible in the one-point vertical velocity spectra S_w, except for at $H_s > 1.2$ m, where a weak spectral peak near 0.2 Hz was distinguishable. The wave-induced fluctuating wind component is generally much weaker compared to the wind turbulence as highlighted by, for example, Weiler and Burling (1967), Kondo et al. (1972) and Naito (1983). An exception may be the case of weak wind and swell conditions, which are more likely to result in the observation of a sharp spectral peak near f_p in the S_w spectrum (Kondo et al., 1972). Nonetheless, as previously mentioned, such conditions are rare near SMW, most likely because SMW was located in a relatively sheltered closed-water environment rather than in the open ocean.

5.3 Turbulence spectra

When performing numerical simulations to compute the wind-induced response of wind turbines, an essential input to model the wind inflow conditions is the PSD of the velocity fluctuations. Figures 8–10 depict the PSD estimates for the along-wind, cross-wind, and vertical wind components, respectively, as a function of the reduced frequency f_r for five stability classes. Surface-layer scaling is adopted; i.e. the PSDs are normalised with u_* (Eq. 2) and $\phi_\epsilon^{2/3}$ (Eq. 8). The number of available samples for each stability class is denoted as N and displayed in each panel.

Figures 8 to 10 compare the estimated spectra at $z = 45$ m, $z = 18$ m, and $z = 6$ m a.m.s.l. with the empirical model established on FINO1 (solid black line) at $z = 41$ m a.m.s.l. (Cheynet et al., 2018). The red curves represent the high-frequency asymptotic behaviour of surface-layer spectra for each stability class. It should be noted that the latter curves do not indicate when the inertial subrange starts since the frequencies they cover were arbitrarily chosen.

In Fig. 8, the maximum values of the normalised spectra for near-neutral conditions ($-0.1 \le \zeta \le 0.1$) are close to unity, as described by Kaimal et al. (1972). The velocity spectra estimated at 45 m a.m.s.l. sometimes show deviations from the surface-layer scaling under near-neutral and stable conditions, likely due to the observed aforementioned uncorrelated high-frequency noise, which leads to an underestimation of the friction velocity. Under light and moderate unstable conditions, i.e. $-0.3 \le \zeta \le -0.1$, the velocity spectra at 6 m and 18 m a.m.s.l. are similar, which supports the idea that the wave sublayer is shallower than 6 m. As mentioned in Sect. 5.1, the non-dimensional stability parameter ζ estimated at 6 m reflected the predominance of near-neutral conditions. This results in discrepancies between the spectral estimates at 6 and 18 m in Figs. 8 to 10 which increase with $|\zeta|$.

Following surface-layer scaling, the normalised spectra at different heights should collapse onto one single curve at high frequencies, which was observed at heights between 40 and 80 m a.m.s.l., at FINO1 for $|\zeta| < 1$. However, this is not always the case in Figs. 8–10. Deviations from surface-layer scaling may be partly attributed to transducer-induced flow distortion. Regarding the velocity data at 45 m a.m.s.l., the measurement noises lift the high-frequency range of the velocity spectra above the spectral slope predicted by Eq. (5) or Eq. (6). At 18 m a.m.s.l., Eqs. (5) and (6) predict remarkably well the velocity spectra at $f_r > 3$, indicating that surface-layer scaling is applicable at this height.

The presence of the spectral gap (Van der Hoven, 1957), separating the microscale fluctuations from the sub-

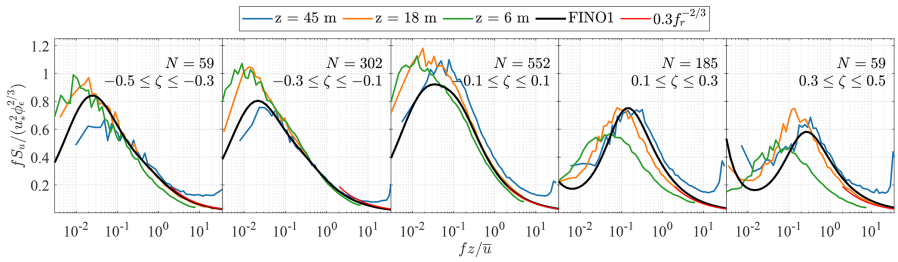

Figure 8. Normalised spectra of the along-wind component at 45, 18, and 6 m a.m.s.l. for various stability conditions. The red curve is derived from Eq. (5), and N denotes the number of samples considered for ensemble averaging.

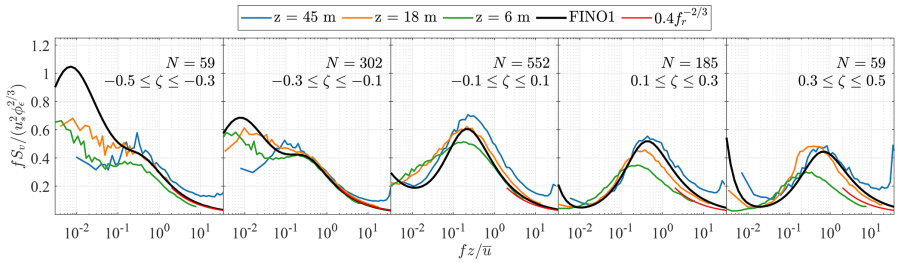

Figure 9. Normalised spectra of the cross-wind component at 45, 18, and 6 m a.m.s.l. for various stability conditions. The red curve is derived from Eq. (6), and N denotes the number of samples considered for ensemble averaging.

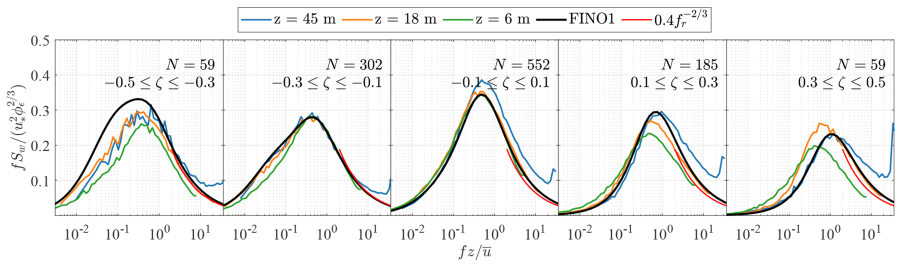

Figure 10. Normalised spectra of the vertical wind component at 45, 18, and 6 m a.m.s.l. for various stability conditions. The red curve is derived from Eq. (6), and N denotes the number of samples considered for ensemble averaging.

mesoscale and mesoscale ones, is noticeable at $\zeta > 0.3$, in line with previous observations (Smedman-Högström and Högström, 1975; Cheynet et al., 2018). Under stable conditions, the spectral gap seems to move toward lower frequencies as the height above the surface decreases. This contrasts with the observations from an onshore mast on Østerild (Denmark) by Larsén et al. (2018), which indicated that the location of the spectral gap on the frequency axis was relatively constant with height.

As mentioned by Vickers and Mahrt (2003), the spectral gap timescale can be only a few minutes long under stable conditions. For $\zeta > 0.3$, the averaging period selected in the present study may be too large to provide reliable integral turbulence characteristics. However, filtering out the mesoscale motion may not be desirable for structural design purposes since operating wind turbines experience both turbulence and mesoscale fluctuations (Veers et al., 2019). In this regard, the use of spectral flow characteristics to parametrise the wind loading on OWTs is preferable.

Under near-neutral conditions, the sensors at 6 and 18 m a.m.s.l. are likely located in the so-called eddy surface layer (Högström et al., 2002; Drobinski et al., 2004), where the sea surface blocks the flow and distorts eddies. This leads to a flat spectral peak. As a result, the integral length scale would be estimated with large uncertainties. Such a spectral behaviour has also been observed above the eddy surface

layer (Drobinski et al., 2004; Mikkelsen et al., 2017), but its consequences for wind turbine loads are unclear.

Overall, the velocity spectra estimated at 18 and 45 m a.m.s.l. at Vindeby match well with the empirical spectra estimated at 41 m a.m.s.l. on FINO1 for $-0.5 \leq \zeta < 0.5$. This comparison is encouraging for further explorations of the surface-layer turbulence characteristics at coastal and offshore sites. Nonetheless, detailed wind measurements at heights of $z \geq 100$ m are needed to obtain a complete overview of the turbulence characteristics in the MABL that is relevant for OWT designs.

5.4 Co-coherence of turbulence

The vertical co-coherence of the along-wind, cross-wind, and vertical wind components are denoted by γ_u, γ_v, and γ_w, respectively. Under near-neutral conditions ($|\zeta| \leq 0.1$), these are expressed as a function of kd_z in Fig. 11 where $k = 2\pi f/\overline{u}$ is the wave number, assuming that turbulence is frozen (Taylor, 1938). The co-coherence estimates are presented for three separation distances d_z because three measurement heights ($z_1 = 45$ m, $z_2 = 18$ m, and $z_3 = 6$ m) were used. The co-coherences estimated on SMW are compared to the IEC coherence model (Eq. 16) and the modified Bowen model (Eq. 13). For the latter model, the parameters estimated on FINO1 (Cheynet, 2019) are directly used. The decay coefficients used for Eq. (13) were, therefore, $[c_1^u, c_2^u, c_3^u] = [6.0, 17.8, 0.02]$ and $[c_1^w, c_2^w, c_3^w] = [2.7, 4.0, 0.16]$ as well as $[c_1^v, c_2^v, c_3^v] = [0, 23.0, 0.09]$.

Figure 11 shows that the coefficients of the modified Bowen model estimated on FINO1 apply very well to γ_u estimated on SMW. Larger deviations are observed for the cross-wind components, for which γ_v displays large negative values, especially for separations between 6 and 45 m a.m.s.l. At FINO1, the negative part of γ_v was relatively small, which justified the use of Eq. (13) with no negative co-coherence values. Following Bowen et al. (1983), ESDU 85020 (2002), or Chougule et al. (2012), the negative part is a consequence of the phase difference and is non-negligible for the cross-wind component, which is also observed in the present case. Since this phase difference increases with the mean wind shear, it is more visible at SMW than at FINO1, where the measurements are at greater heights than at SMW. The co-coherence of the vertical component estimated on SMW deviates from the one fitted to observations at the FINO platform. The source of such deviations remains unclear.

The IEC exponential coherence model over-predicts γ_u when the measurement height decreases and when the separation distance increases because this model follows fairly well Davenport's similarity, except at $kd_z < 0.1$. In Cheynet (2019), the Davenport model was suspected to lead to an overestimation of the turbulent wind loading on OWTs. The present results indicate that a similar overestimation may be obtained if the IEC exponential coherence model is used. Further studies are, however, needed to better quantify this possible overestimation in terms of dynamic wind loading on the wind turbine's rotor and tower, as well as on the floater's motions in the case of a floating wind turbine. Finally, additional data collection is needed to study the co-coherence at lateral separations, which is required for wind turbine design since it was not available at FINO1 or SMW.

To demonstrate the effect of the thermal stratification on the observed co-coherence at SMW, Fig. 12 shows the estimated co-coherence for $-2 \leq \zeta \leq 2$ for the three turbulence components. As observed by, for example, Soucy et al. (1982) or Cheynet et al. (2018) and modelled by Chougule et al. (2018), the vertical co-coherence is generally highest for convective conditions and smallest for stable conditions. Such results reinforce the idea that modelling the turbulent loading on offshore wind turbines using a coherence model established for neutral conditions may only be appropriate for the ultimate limit state design but not for the fatigue life design.

5.5 Relevancy of the database for load calculation of OWTs

This study provides a thorough overview of the MABL spectral turbulence characteristics with respect to the variation in the atmospheric stability at SMW. However, its direct applicability for the designs of OWTs should be assessed carefully due to the assumptions made in the data analysis.

The presented results do not include the non-stationary conditions encountered in the field, which were removed before the analysis. About 20 % of the data were disregarded as non-stationary to establish reliable spectra and co-coherence estimates. In the present case, non-stationary fluctuations were mainly associated with frequencies close to or below 0.05 Hz. For typical spar-type and semisubmersible OWT floaters, these frequencies encompass the quasi-static motions and a few of the lowest eigenfrequencies of the floaters (Jonkman and Musial, 2010; Robertson et al., 2014). Additionally, the non-stationary turbulence fluctuations could result in non-Gaussian loadings, which could further lead to underestimation of fatigue loading (Benasciutti and Tovo, 2006, 2007).

Furthermore, the present dataset was recorded at heights lower than the hub height of the recent and the future OWTs, which is around 130 m (e.g. GE Renewable Energy, 2021). At such heights, MOST may no longer be applicable (Peña and Gryning, 2008; Cheynet et al., 2021). Above the surface layer, the velocity spectra may become independent of the height above the surface, which is coarsely accounted for in IEC 61400-1 (2005).

6 Conclusions

This study explores the turbulence spectral characteristics from wind records of a year duration on an offshore mast called Sea Mast West (SMW) near the first offshore wind

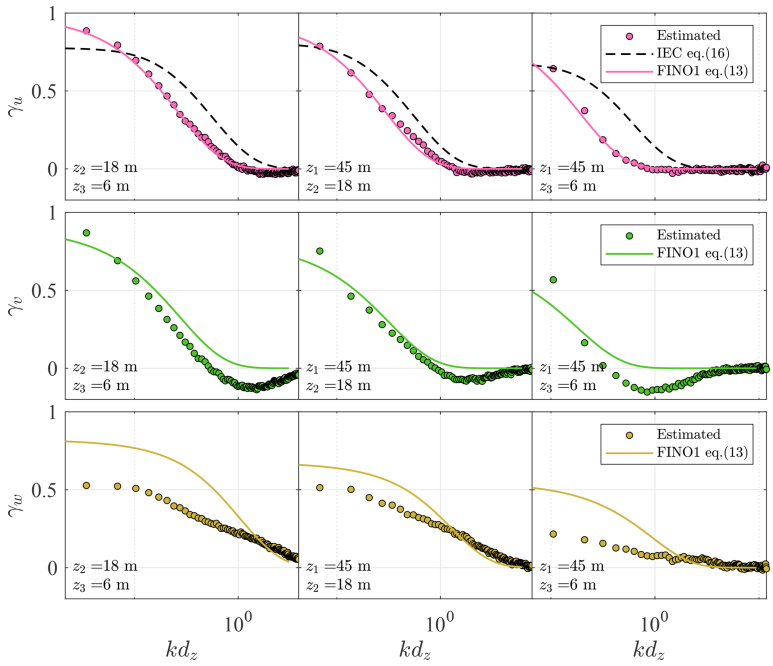

Figure 11. Co-coherences of the along-wind (top panels), lateral (middle panels), and vertical velocity components (lower panels) for $|\zeta| \leq 0.1$ at three different vertical separation distances. The dots represent the measurement, and the lines mark the predictions using the IEC exponential coherence model (dashed line) and the modified Bowen model (solid line) with the fitted coefficients from FINO1 (Cheynet, 2019).

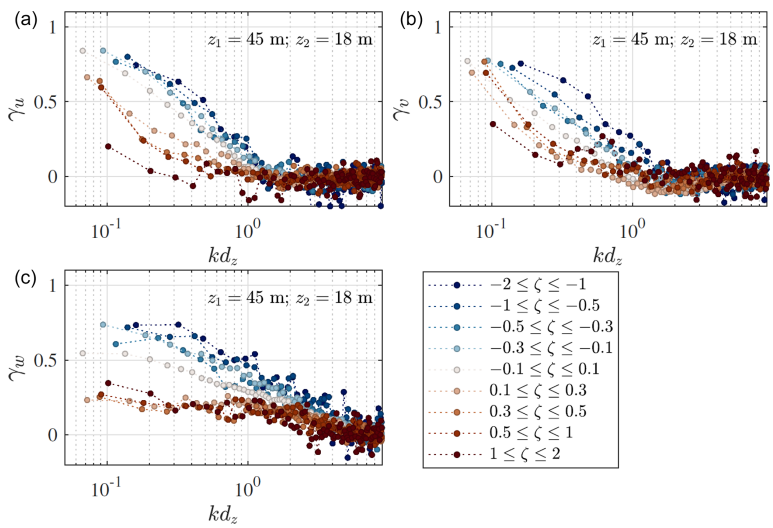

Figure 12. Co-coherence of the along-wind **(a)**, cross-wind **(b)**, and vertical **(c)** velocity components for nine stability classes, given by $\zeta = z/L$. The separation distance is 27 m between the sensors at 18 m and 45 m a.m.s.l.

farm Vindeby. We aim to identify similarities between the turbulence characteristics estimated on the FINO1 platform in the North Sea and those at Vindeby. Such an investigation is crucial to establish appropriate turbulence models relevant for the design of offshore wind turbines (OWTs). The dataset analysed was acquired by 3D sonic anemometers at 6, 18, and 45 m a.m.s.l., which complements the dataset collected between 40 m and 80 m a.m.s.l. on FINO1 (Cheynet et al., 2018).

The correlation between the sea surface elevation and the vertical turbulent fluctuations at 6 m a.m.s.l. is quantified in terms of co-coherence between the vertical turbulent component and the velocity of the sea surface elevation. However, it is clearly visible for significant wave heights H_s exceeding 0.9 m only. Therefore, it is concluded that the sonic anemometers are located above the wave boundary layer most of the time.

The measurements at 18 m a.m.s.l. follow fairly well surface-layer scaling, as expected. Because the sensors at 6 and 18 m are located in the lower part of the surface layer, a wide spectral peak for near-neutral stratification is observed, which reflects the distortion of the eddies as they scrape along the surface. For $\zeta = |z/L| \leq 0.3$, the power spectral density of the along-wind velocity component at 18 and 45 m is consistent with the empirically defined spectral models estimated at 41 m on FINO1 (Cheynet et al., 2018). In the present case, most of the wind records are associated with $|\zeta| < 0.3$. Nonetheless, for $|\zeta| > 0.3$, deviations from the empirical spectral model fitted to the data recorded on the FINO1 platform may be attributed to transducer-induced flow distortion and/or limited applicability of the surface-layer scaling.

The co-coherence estimates of the along-wind component for neutral atmospheres are well described by the same three-parameter exponential decay function as used at FINO1 (Cheynet, 2019). However, this is not the case for the lateral wind components due to the closer distance to the sea surface, which amplifies the phase differences between measurements at two different heights. For the vertical component, the co-coherence decreases faster than the predicted values at FINO1 (Cheynet et al., 2018). Under stable stratification, the co-coherence estimates of the three turbulent components (γ_u, γ_v, and γ_w) are significantly lower than for near-neutral conditions, in particular for $kd_z < 1$. On the other hand, γ_u, γ_v, and γ_w are slightly higher for convective conditions compared to near-neutral conditions at $kd_z < 1$. Since the co-coherence is one of the governing parameters for wind loading on structures, its dependency on the atmospheric stability, which is rarely documented in the marine atmospheric boundary layer, may become essential to establishing design criteria for OWT fatigue life. The variability in Hywind Scotland wind turbines' floater motion with atmospheric stability (Jacobsen and Godvik, 2021) may be one example that demonstrates the importance of stability-corrected co-coherence in OWT responses.

Although the Vindeby dataset is located below recent wind turbines' sizes, this does not mean that the dataset may not be useful for wind turbine design purposes. In fact, the widely known Kansas spectra were based on the observations at heights not exceeding 30 m (Kaimal et al., 1972) and have been adopted in IEC 61400-1 (2005). From the Vindeby dataset, we found some similarities with the Kansas spectra for near-neutral conditions. For non-neutral conditions, the turbulence spectra at height 45 m a.m.s.l. have a consistent behaviour with the predicted spectra at FINO1 at 41.5 m a.m.s.l. The comparison between the turbulence characteristics at Vindeby and FINO1 is therefore valuable to further develop comprehensive spectral turbulence models that are suitable for modern OWT designs. Nevertheless, future atmospheric measurements at heights up to 250 m a.m.s.l. are necessary to obtain the knowledge of turbulence characteristics where the surface-layer scaling may no longer be applicable.

Appendix A: Sonic anemometer tilt correction

The friction velocity estimates using the double-rotation technique, sectoral planar fit, and the method by Klipp (2018) are compared in Fig. A1. In general, the friction velocity estimates from all methods are in good agreement. The average correlation coefficient for all heights is 0.985 for $|\zeta| \leq 2$. The PF algorithm leads to a slightly larger scatter between u_{*R} and u_*, where the average correlation coefficient from all heights is 0.976 for $|\zeta| \leq 2$ (Table A1). The double-rotation algorithm seems to give a smaller deviation between u_{*R} and u_* than the PF algorithm in the present study, which justified the adoption of the double rotation as a tilt correction method herein.

Klipp (2018) noted that u_{*R} is appropriate to estimate the friction velocity if the thermal stratification of the atmosphere is neutral only. Yet, Fig. A1 suggests that Klipp's method performs well for non-neutral conditions too, as highlighted by the correlation coefficients in Table A1, which vary between 0.963 and 0.989. Additional studies using measurements from other coastal or offshore sites are needed to assess if such observations are recurring.

The angle between the stress vector and the wind vector is given as $\alpha = \arctan\left(\overline{v'w'}/\overline{u'w'}\right)$ (Grachev et al., 2003). It is found that α increases from 8° at 6 m a.m.s.l. to 13° at 45 m a.m.s.l. when $\overline{v'w'} < 0$. When $\overline{v'w'} > 0$, α is almost constant with the height with an average value of −7°. The relatively low value of α, therefore, suggests that the direction of the wind–wave-induced stress is fairly well aligned with the mean wind direction near SMW.

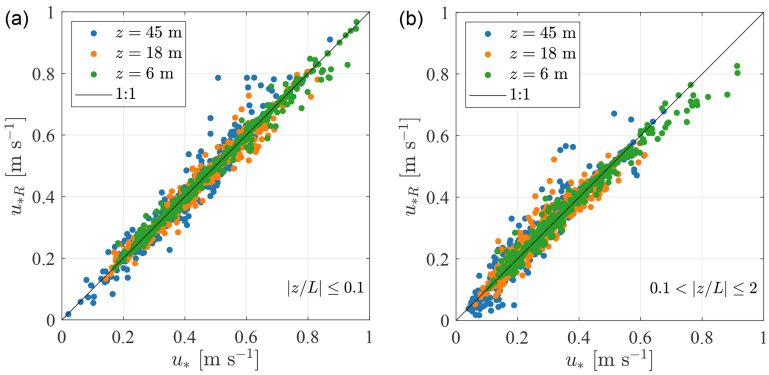

Figure A1. Friction velocity computed using the eddy covariance method with the double-rotation method compared with the Klipp method. Panel **(a)** considers only $|z/L| \leq 0.1$, and panel **(b)** considers $0.1 < |z/L| \leq 2$.

Table A1. Correlation coefficients between $u_{*\mathrm{R}}$ and u_* using the planar fit (PF) or double rotation (DR).

	$\lvert z/L\rvert \leq 0.1$			$0.1 < \lvert z/L\rvert \leq 2.0$		
	6 m	18 m	45 m	6 m	18 m	45 m
PF	0.989	0.976	0.962	0.981	0.954	0.942
DR	0.995	0.986	0.973	0.989	0.968	0.963

Appendix B: Transducer-shadow effect

The sonic anemometers mounted at 6, 18, and 45 m a.m.s.l. were omnidirectional solent anemometers, which can be prone to flow distortion by the transducer. Between May and September 1994, a Gill solent anemometer with an asymmetric head was installed at 10 m a.m.s.l. on the southern boom of SMW (i.e. on the same side as the other three anemometers). The asymmetric head reduces the flow distortion by the transducer, at least for a specific wind sector. Although the flow distortion by the asymmetric solent was actually unknown, this sensor was used to assess the error in the friction velocity calculated with the omnidirectional solent anemometers. Only wind directions from 220 to 330° were selected as they corresponded to the sector investigated in the present study.

Flow distortion is assumed to be a function of the angle of attack $\alpha(z)$ and wind direction $\theta(z)$ only. Therefore, using a multivariate regression analysis, it is possible to quantify the variability in $u_*(z)$ with its value at 10 m, denoted $(u_*)_{10}$, as a function of $\alpha(z)$ and $\theta(z)$. For the relatively narrow sector selected, it was found that cubic functions of $\alpha(z)$ and $\theta(z)$ were sufficient to describe this variability. This leads to the following relationship between the friction velocity at 10 m and the one u_* at height z:

$$u_*(z) = (u_*)_{10} \cdot \mathbf{A}\mathbf{X}^\top, \tag{B1}$$

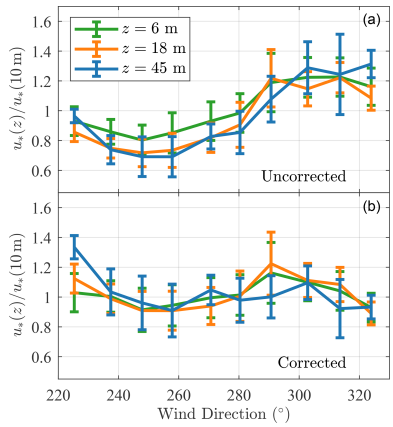

Figure B1. Ratio of the friction velocity by the omnidirectional solent anemometers to the one estimated at 10 m (asymmetric solent anemometer) before **(a)** and after **(b)** correction using a multivariate regression analysis. Velocity data recorded between May and September 1994 for the sector 220–330° were used (480 samples of 30 min duration), and $|z/L| < 2$ at 10 m a.m.s.l.

$$\mathbf{A} = \begin{bmatrix} a_1 & a_2 & a_3 & a_4 & a_5 & a_6 \end{bmatrix}, \tag{B2}$$

$$\mathbf{X} = \begin{bmatrix} \theta(z) & \theta(z)^2 & \theta(z)^3 & \alpha(z) & \alpha(z)^2 & \alpha(z)^3 \end{bmatrix}, \tag{B3}$$

where $\mathbf{A}$ is the matrix of coefficients to be determined with the regression analysis. In Eqs. (B1)–(B3), the friction velocity is not forced to be constant with the height and we do not assume that the flow distortion is similar for the three omnidirectional anemometers.

In the top panel of Fig. B1, the maximum variations in the friction velocity between the sonic anemometer at 10 and 18 m are ±20 %, when all the samples in the sector 10 m are

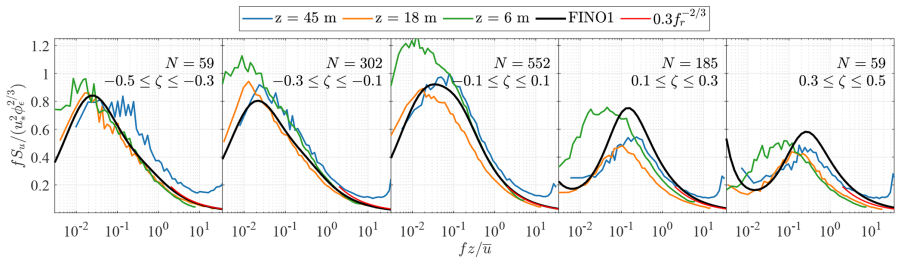

Figure B2. Normalised spectra of the along-wind component on SMW with the corrected friction velocity and five stability bins. The red curve is derived from Eq. (5), and N denotes the number of samples considered for ensemble averaging.

4 %, 12 %, and 11 %, respectively. After the multivariate regression, the sector-averaged error is nearly zero, although it is clearly not zero for a given wind direction. On average, the friction velocity estimates at 6 and 10 m are, therefore, almost identical, given that the random error in the friction velocity is above 10 % for a sample duration of 30 min (Kaimal and Finnigan, 1994). As shown in Fig. B1, the use of sector-averaged flow characteristics may mitigate the influence of transducer-induced flow distortion of the spectral flow characteristics estimated at 6, 18, and 45 m.

A comparison of the power spectral densities of the u component was conducted with and without the corrected friction velocity. Only data between May and September 1994 were selected, and the Obukhov length was computed at 10 m a.m.s.l. Five stability bins were identified in this dataset. However, limited improvement was observed after the application of the correction algorithm. A further comparison was also conducted for the entire dataset, i.e. between May 1994 and July 1995, as shown in Fig. B2. This resulted in similar conclusions, where the uncorrected (Fig. 8) and the corrected PSDs of the u component are not too far off each other. Therefore, it was decided not to use any correction for the friction velocity to avoid over-processing the data.

Data availability. The data used for SMW have been openly available under CC BY 4.0 since 2021 (Hansen et al., 2021).

Author contributions. RMP and EC curated the data and provided the formal analysis, methodology, software, and visualisation. RMP and EC prepared the original draft. JBJ and CO conducted supervision, review, and editing of the manuscript. All authors contributed to the conceptualisation and finalisation of the paper.

Competing interests. The contact author has declared that none of the authors has any competing interests.

Disclaimer. Publisher's note: Copernicus Publications remains neutral with regard to jurisdictional claims in published maps and institutional affiliations.

Acknowledgements. The authors would like to express their gratitude to Kurt Hansen for providing the Vindeby dataset. Joachim Reuder and Stephan Kral are acknowledged for fruitful discussion on the wave and wind conditions near SMW.

Review statement. This paper was edited by Sandrine Aubrun and reviewed by Bernhard Lange and two anonymous referees.

References

Akaike, H.: Fitting autoregressive models for prediction, Ann. Inst. Stat. Math., 21, 243–247, 1969.

Archer, C. L., Colle, B. A., Veron, D. L., Veron, F., and Sienkiewicz, M. J.: On the predominance of unstable atmospheric conditions in the marine boundary layer offshore of the US northeastern coast, J. Geophys. Res.-Atmos., 121, 8869–8885, 2016.

Barthelmie, R. J.: The effects of atmospheric stability on coastal wind climates, Meteorol. Appl., 6, 39–47, 1999.

Barthelmie, R. J., Courtney, M., Højstrup, J., and Sanderhoff, P.: The Vindeby project: A description, Tech. Rep. 741(EN), Risø National Laboratory, Denmark, https://orbit.dtu.dk/en/publications/the-vindeby-project-a-description (last access: 31 July 2022), 1994.

Benasciutti, D. and Tovo, R.: Fatigue life assessment in non-Gaussian random loadings, Int. J. Fatig., 28, 733–746, 2006.

Benasciutti, D. and Tovo, R.: Frequency-based fatigue analysis of non-stationary switching random loads, Fatig. Fract. Eng. Mater.Struct., 30, 1016–1029, 2007.

Benilov, A. Y., Kouznetsov, O., and Panin, G.: On the analysis of wind wave-induced disturbances in the atmospheric turbulent surface layer, Bound.-Lay. Meteorol., 6, 269–285, 1974.

Bowen, A. J., Flay, R. G. J., and Panofsky, H. A.: Vertical coherence and phase delay between wind components in strong winds below 20 m, Bound.-Lay. Meteorol., 26, 313–324, 1983.

Cheynet, E.: Influence of the measurement height on the vertical coherence of natural wind, in: Conference of the Italian Association for Wind Engineering, IN VENTO, 9–12 Septem-

ber 2018, Naples, Italy, 207–221, https://doi.org/10.1007/978-3-030-12815-9_17, 2019.

Cheynet, E., Jakobsen, J. B., and Obhrai, C.: Spectral characteristics of surface-layer turbulence in the North Sea, Energy Proced., 137, 414–427, 2017.

Cheynet, E., Jakobsen, J., and Reuder, J.: Velocity Spectra and Coherence Estimates in the Marine Atmospheric Boundary Layer, Bound.-Lay. Meteorol., 169, 429–460, 2018.

Cheynet, E., Jakobsen, J. B., and Snæbjörnsson, J.: Flow distortion recorded by sonic anemometers on a long-span bridge: Towards a better modelling of the dynamic wind load in full-scale, J. Sound Vibrat., 450, 214–230, 2019.

Cheynet, E., Flügge, M., Reuder, J., Jakobsen, J. B., Heggelund, Y., Svardal, B., Saavedra Garfias, P., Obhrai, C., Daniotti, N., Berge, J., Duscha, C., Wildmann, N., Onarheim, I. H., and Godvik, M.: The COTUR project: remote sensing of offshore turbulence for wind energy application, Atmos. Meas. Tech., 14, 6137–6157, https://doi.org/10.5194/amt-14-6137-2021, 2021.

Chougule, A., Mann, J., Kelly, M., Sun, J., Lenschow, D., and Patton, E.: Vertical cross-spectral phases in neutral atmospheric flow, J. Turbulence, 36, 1–13, https://doi.org/10.1080/14685248.2012.711524, 2012.

Chougule, A., Mann, J., Kelly, M., and Larsen, G.: Simplification and Validation of a Spectral-Tensor Model for Turbulence Including Atmospheric Stability, Bound.-Lay. Meteorol., 167, 371–397, 2018.

Davenport, A. G.: The spectrum of horizontal gustiness near the ground in high winds, Q. J. Royal Meteorol. Soc., 87, 194–211, 1961.

De Maré, M. and Mann, J.: Validation of the Mann spectral tensor for offshore wind conditions at different atmospheric stabilities, J. Phys.: Conf. Ser., 524, 012106, https://doi.org/10.1088/1742-6596/524/1/012106, 2014.

D'Errico, J.: inpaint_nans, MATLAB Central File Exchange, http://kr.mathworks.com/matlabcentral/fileexchange/4551-inpaint-nans (last access: November 2021), 2004.

Dobson, F. W.: Review of reference height for and averaging time of surface wind measurements at sea, World Meteorological Organization, https://library.wmo.int/doc_num.php?explnum_id=7561 (last access: 2 March 2021), 1981.

Doubrawa, P., Churchfield, M. J., Godvik, M., and Sirnivas, S.: Load response of a floating wind turbine to turbulent atmospheric flow, Appl. Energy, 242, 1588–1599, 2019.

Drobinski, P., Carlotti, P., Newsom, R. K., Banta, R. M., Foster, R. C., and Redelsperger, J. L.: The structure of the near-neutral atmospheric surface layer, J. Atmos. Sci., 61, 699–714, 2004.

Edson, J. and Fairall, C.: Similarity relationships in the marine atmospheric surface layer for terms in the TKE and scalar variance budgets, J. Atmos. Sci., 55, 2311–2328, 1998.

Emeis, S. and Türk, M.: Wind-driven wave heights in the German Bight, Ocean Dynam., 59, 463–475, 2009.

ESDU 85020: ESDU 85020 Characteristics of atmospheric turbulence near the ground. Part II: single point data for strong winds (neutral atmosphere), ESDU – Engineering Sciences Data Unit, https://www.osti.gov/etdeweb/biblio/10158377 (last access: 31 July 2022), 2002.

Geernaert, G.: Measurements of the angle between the wind vector and wind stress vector in the surface layer over the North Sea, J. Geophys. Res.-Oceans, 93, 8215–8220, 1988.

Geernaert, G., Hansen, F., Courtney, M., and Herbers, T.: Directional attributes of the ocean surface wind stress vector, J. Geophys. Res.-Oceans, 98, 16571–16582, 1993.

GE Renewable Energy: Haliade-X offshore wind turbine, https://www.ge.com/renewableenergy/wind-energy/offshore-wind/haliade-x-offshore-turbine, last access: 8 April 2021.

Grachev, A., Fairall, C., Hare, J., Edson, J., and Miller, S.: Wind stress vector over ocean waves, J. Phys. Oceanogr., 33, 2408–2429, 2003.

Grare, L., Lenain, L., and Melville, W. K.: Wave-coherent airflow and critical layers over ocean waves, J. Phys. Oceanogr., 43, 2156–2172, 2013.

Hansen, A. and Butterfield, C.: Aerodynamics of horizontal-axis wind turbines, Annu. Rev. Fluid Mech., 25, 115–149, 1993.

Hansen, K. S., Larsen, G. C., and Ott, S.: Dependence of offshore wind turbine fatigue loads on atmospheric stratification, J. Phys.: Conf. Ser., 524, 012165, https://doi.org/10.1088/1742-6596/524/1/012165, 2014.

Hansen, K. S., Vasiljevic, N., and Sørensen, S. A.: Resource data and turbulence array measurements from the 3 Vindeby masts, DTU, https://doi.org/10.11583/DTU.14387480.v1, 2021.

Högström, U.: Von Karman's constant in atmospheric boundary layer flow: Reevaluated, J. Atmos. Sci., 42, 263–270, 1985.

Högström, U.: Non-dimensional wind and temperature profiles in the atmospheric surface layer: A re-evaluation, in: Topics in Micrometeorology. A Festschrift for Arch Dyer, Springer, 55–78, https://doi.org/10.1007/978-94-009-2935-7_6, 1988.

Högström, U., Hunt, J., and Smedman, A.-S.: Theory and measurements for turbulence spectra and variances in the atmospheric neutral surface layer, Bound.-Lay. Meteorol., 103, 101–124, 2002.

Hojstrup, J.: A statistical data screening procedure, Meas. Sci. Technol., 4, 153–157, https://doi.org/10.1088/0957-0233/4/2/003/, 1993.

Holtslag, M. C., Bierbooms, W. A. A. M., and Van Bussel, G. J. W.: Wind turbine fatigue loads as a function of atmospheric conditions offshore, Wind Energy, 19, 1917–1932, 2016.

Hristov, T., Friehe, C., and Miller, S.: Wave-coherent fields in air flow over ocean waves: Identification of cooperative behavior buried in turbulence, Phys. Rev. Lett., 81, 5245, https://doi.org/10.1103/PhysRevLett.81.5245, 1998.

IEC: IEC 61400-1: Wind turbines – Part 1: Design requirements (2005), https://webstore.iec.ch/publication/5426 (last access: 3 August 2022), 2005.

Jacobsen, A. and Godvik, M.: Influence of wakes and atmospheric stability on the floater responses of the Hywind Scotland wind turbines, Wind Energy, 24, 149–161, 2021.

Janssen, P. A.: Wave-induced stress and the drag of air flow over sea waves, J. Phys. Oceanogr., 19, 745–754, 1989.

Jiang, Q.: Influence of Swell on Marine Surface-Layer Structure, J. Atmos. Sci., 77, 1865–1885, 2020.

Jiang, Q., Wang, Q., Wang, S., and Gaberšek, S.: Turbulence adjustment and scaling in an offshore convective internal boundary layer: A CASPER case study, J. Atmos. Sci., 77, 1661–1681, 2020.

Johnson, H. K., Højstrup, J., Vested, H. J., and Larsen, S. E.: On the dependence of sea surface roughness on wind waves, J. Phys. Oceanogr., 28, 1702–1716, 1998.

Jonkman, J. and Musial, W.: Offshore code comparison collaboration (OC3) for IEA Wind Task 23 offshore wind technology and deployment, Tech. rep., NREL – National Renewable Energy Lab., Golden, CO, USA, https://www.nrel.gov/docs/fy11osti/48191.pdf (last access: 21 December 2020), 2010.

Kaimal, J. C. and Finnigan, J. J.: Atmospheric Boundary Layer Flows: Their Structure and Measurement, Oxford University Press, ISBN 0-19-506239-6, 1994.

Kaimal, J. C., Wyngaard, J. C. J., Izumi, Y., and Coté, O. R.: Spectral characteristics of surface-layer turbulence, Q. J. Roy. Meteorol. Soc., 98, 563–589, 1972.

Kelly, M.: From standard wind measurements to spectral characterization: turbulence length scale and distribution, Wind Energ. Sci., 3, 533–543, https://doi.org/10.5194/wes-3-533-2018, 2018.

Klipp, C.: Turbulent friction velocity calculated from the Reynolds stress tensor, J. Atmos. Sci., 75, 1029–1043, 2018.

Kondo, J., Fujinawa, Y., and Naito, G.: Wave-induced wind fluctuation over the sea, J. Fluid Mech., 51, 751–771, 1972.

Kristensen, L. and Jensen, N.: Lateral coherence in isotropic turbulence and in the natural wind, Bound.-Lay. Meteorol., 17, 353–373, 1979.

Kristensen, L., Panofsky, H. A., and Smith, S. D.: Lateral coherence of longitudinal wind components in strong winds, Bound.-Lay. Meteorol., 21, 199–205, 1981.

Larsén, X. G., Petersen, E. L., and Larsen, S. E.: Variation of boundary-layer wind spectra with height, Q. J. Roy. Meteorol. Soc., 144, 2054–2066, 2018.

Leys, C., Ley, C., Klein, O., Bernard, P., and Licata, L.: Detecting outliers: Do not use standard deviation around the mean, use absolute deviation around the median, J. Exp. Social Psychol., 49, 764–766, 2013.

Lumley, J. and Panofsky, H.: The Structure of Atmospheric Turbulence, Interscience monographs and texts in physics and astronomy, Interscience Publishers, ISBN 9780470553657, 1964.

Mahrt, L., Vickers, D., Howell, J., Højstrup, J., Wilczak, J. M., Edson, J., and Hare, J.: Sea surface drag coefficients in the Risø Air Sea Experiment, J. Geophys. Res.-Oceans, 101, 14327–14335, 1996.

Mahrt, L., Vickers, D., Edson, J., Wilczak, J. M., Hare, J., and Højstrup, J.: Vertical structure of turbulence in offshore flow during RASEX, J. Geophys. Res.-Oceans, 101, 14327–14335, 2001.

Mann, J.: The spatial structure of neutral atmospheric surface-layer turbulence, J. Fluid Mech., 273, 141–168, 1994.

Mikkelsen, T., Larsen, S. E., Jørgensen, H. E., Astrup, P., and Larsén, X. G.: Scaling of turbulence spectra measured in strong shear flow near the Earth's surface, Physica Scripta, 92, 124002, https://doi.org/10.1088/1402-4896/aa91b2, 2017.

Monin, A. S.: The structure of atmospheric turbulence, Theor. Probabil. Appl., 3, 266–296, 1958.

Monin, A. S. and Obukhov, A. M.: Basic laws of turbulent mixing in the atmosphere near the ground, Tr. Geofiz. Inst., Akad. Nauk SSSR, 24, 163–187, 1954.

Mouzakis, F., Morfiadakis, E., and Dellaportas, P.: Fatigue loading parameter identification of a wind turbine operating in complex terrain, J. Wind Eng. Indust. Aerodynam., 82, 69–88, 1999.

Naito, G.: Spatial structure of surface wind over the ocean, J. Wind Eng. Indust. Aerodynam., 13, 67–76, 1983.

Nielsen, F. G., Hanson, T. D., and Skaare, B.: Integrated dynamic analysis of floating offshore wind turbines, in: vol. 47462, 25th International Conference on Offshore Mechanics and Arctic Engineering, 4–9 June 2006, Hamburg, Germany, 671–679, https://doi.org/10.1115/OMAE2006-92291, 2006.

Nybø, A., Nielsen, F. G., Reuder, J., Churchfield, M. J., and Godvik, M.: Evaluation of different wind fields for the investigation of the dynamic response of offshore wind turbines, Wind Energy, 23, 1810–1830, 2020.

Peña, A. and Gryning, S.-E.: Charnock's roughness length model and non-dimensional wind profiles over the sea, Bound.-Lay. Meteorol., 128, 191–203, 2008.

Peña, A., Dellwik, E., and Mann, J.: A method to assess the accuracy of sonic anemometer measurements, Atmos. Meas. Tech., 12, 237–252, https://doi.org/10.5194/amt-12-237-2019, 2019.

Power Technology: Full circle: decommissioning the first ever offshore windfarm, https://www.power-technology.com/features/full-circle-decommissioning-first-ever-offshore-windfarm/ (last access: 28 March 2021), 2020.

Putri, R., Obhrai, C., Jakobsen, J., and Ong, M.: Numerical Analysis of the Effect of Offshore Turbulent Wind Inflow on the Response of a Spar Wind Turbine, Energies, 13, 2506, https://doi.org/10.3390/en13102506, 2020.

Robertson, A., Jonkman, J., Vorpahl, F., Popko, W., Qvist, J., Frøyd, L., Chen, X., Azcona, J., Uzunoglu, E., Guedes Soares, C., Luan, C., Yutong, H., Pengcheng, F., Yde, A., Larsen, T., Nichols, J., Buils, R., Lei, L., Anders Nygard, T., Manolas, D., Heege, A., Ringdalen Vatne, S., Ormberg, H., Duarte, T., Godreau, C., Fabricius Hansen, H., Wedel Nielsen, A., Riber, H., Le Cunff, C., Abele, R., Beyer, F., Yamaguchi, A., Jin Jung, K., Shin, H., Shi, W., Park, H., Alves, M., and Guérinel, M.: Offshore code comparison collaboration continuation within IEA wind task 30: phase II results regarding a floating semisubmersible wind system, in: vol. 45547, International Conference on Offshore Mechanics and Arctic Engineering, American Society of Mechanical Engineers, V09BT09A012, https://www.nrel.gov/docs/fy14osti/61154.pdf (last access: 21 December 2020), 2014.

Robertson, A. N., Shaler, K., Sethuraman, L., and Jonkman, J.: Sensitivity analysis of the effect of wind characteristics and turbine properties on wind turbine loads, Wind Energ. Sci., 4, 479–513, https://doi.org/10.5194/wes-4-479-2019, 2019.

Rosner, B.: Percentage points for a generalized ESD many-outlier procedure, Technometrics, 25, 165–172, 1983.

Sacré, C. and Delaunay, D.: Structure spatiale de la turbulence au cours de vents forts sur differents sites, J. Wind Eng. Indust. Aerodynam., 41, 295–303, 1992.

Sanchez Gomez, M. and Lundquist, J. K.: The effect of wind direction shear on turbine performance in a wind farm in central Iowa, Wind Energ. Sci., 5, 125–139, https://doi.org/10.5194/wes-5-125-2020, 2020.

Saranyasoontorn, K., Manuel, L., and Veers, P. S.: A comparison of standard coherence models for inflow turbulence with estimates from field measurements, J. Sol. Energy Eng., 126, 1069–1082, 2004.

Sathe, A. and Bierbooms, W.: Influence of different wind profiles due to varying atmospheric stability on the fatigue life of wind turbines, J. Phys.: Conf. Ser., 75, 012056, https://doi.org/10.1088/1742-6596/75/1/012056, 2007.

Sathe, A., Mann, J., Barlas, T., Bierbooms, W., and van Bussel, G.: Influence of atmospheric stability on wind turbine loads, Wind Energy, 16, 1013–1032, 2013.

Schotanus, P., Nieuwstadt, F., and De Bruin, H.: Temperature measurement with a sonic anemometer and its application to heat and moisture fluxes, Bound.-Lay. Meteorol., 26, 81–93, 1983.

Sempreviva, A. M. and Gryning, S. E.: Humidity fluctuations in the marine boundary layer measured at a coastal site with an infrared humidity sensor, Bound.-Lay. Meteorol., 77, 331–352, 1996.

Sheinman, Y. and Rosen, A.: A dynamic model of the influence of turbulence on the power output of a wind turbine, J. Wind Eng. Indust. Aerodynam., 39, 329–341, 1992.

Sjöblom, A. and Smedman, A.-S.: Vertical structure in the marine atmospheric boundary layer and its implication for the inertial dissipation method, Bound.-Lay. Meteorol., 109, 1–25, 2003a.

Sjöblom, A. and Smedman, A.-S.: Vertical structure in the marine atmospheric boundary layer and its implication for the inertial dissipation method, Bound.-Lay. Meteorol., 109, 1–25, 2003b.

Smedman-Högström, A.-S. and Högström, U.: Spectral gap in surface-layer measurements, J. Atmos. Sci., 32, 340–350, 1975.

Soucy, R., Woodward, R., and Panofsky, H.: Vertical cross-spectra of horizontal velocity components at the Boulder observatory, Bound.-Lay. Meteorol., 24, 57–66, 1982.

Stiperski, I. and Rotach, M. W.: On the measurement of turbulence over complex mountainous terrain, Bound.-Lay. Meteorol., 159, 97–121, 2016.

Stull, R. B.: An Introduction to Boundary Layer Meteorology, in: 1st Edn., Kluwer Academic Publishers, ISBN 978-90-277-2768-8, https://doi.org/10.1007/978-94-009-3027-8, 1988.

Tamura, H., Drennan, W. M., Collins, C. O., and Graber, H. C.: Turbulent airflow and wave-induced stress over the ocean, Bound.-Lay. Meteorol., 169, 47–66, 2018.

Taylor, G. I.: The spectrum of turbulence, P. Roy. Soc. Lond. A, 164, 476–490, 1938.

Van der Hoven, I.: Power spectrum of horizontal wind speed in the frequency range from 0.0007 to 900 cycles per hour, J. Atmos. Sci., 14, 160–164, 1957.

Veers, P., Dykes, K., Lantz, E., Barth, S., Bottasso, C. L., Carlson, O., Clifton, A., Green, J., Green, P., Holttinen, H., Laird, D., Lehtomäki, V., Lundquist, J. K., Manwell, J., Marquis, M., Meneveau, C., Moriarty, P., Munduate, X., Muskulus, M., Naughton, J., Pao, L., Paquette, J., Peinke, J., Robertson, A., Sanz Rodrigo, J., Sempreviva, A. M., Smith, J. C., Tuohy, A., and Wiser, R.: Grand challenges in the science of wind energy, Science, 366, eaau2027, https://doi.org/10.1126/science.aau2027, 2019.

Vickers, D. and Mahrt, L.: Quality control and flux sampling problems for tower and aircraft data, J. Atmos. Ocean. Tech., 14, 512–526, 1997.

Vickers, D. and Mahrt, L.: The cospectral gap and turbulent flux calculations, J. Atmos. Ocean. Tech., 20, 660–672, 2003.

Weber, R. O.: Remarks on the definition and estimation of friction velocity, Bound.-Lay. Meteorol., 93, 197–209, 1999.

Weiler, H. S. and Burling, R.: Direct measurements of stress and spectra of turbulence in the boundary layer over the sea, J. Atmos. Sci., 24, 653–664, 1967.

Welch, P.: The use of fast Fourier transform for the estimation of power spectra: a method based on time averaging over short, modified periodograms, IEEE T. Audio Electroacoust., 15, 70–73, 1967.

Wendell, L., Gower, G., Morris, V., and Tomich, S.: Wind turbulence characterization for wind energy development, Tech. rep., Pacific Northwest Lab., Richland, WA, USA, https://www.osti.gov/servlets/purl/602073 (last access: 3 November 2021), 1991.

Wilczak, J., Oncley, S., and Stage, S.: Sonic anemometer tilt correction algorithms, Bound.-Lay. Meteorol., 99, 127–150, 2001.

WMO: Guide to meteorological instruments and methods of observation, Secretariat of the World Meteorological Organization, ISBN 978-92-63-10008-5, 2008.

Wyngaard, J. C.: On the surface-layer turbulence, in: Workshop on Micrometeorology, edited by: Haugen, D. A., American Meteorological Society, 101–149, https://cir.nii.ac.jp/crid/1570291225953095424 (last access: 1 March 2021), 1973.

Wyngaard, J. C. and Coté, O. R.: The budgets of turbulent kinetic energy and temperature variance in the atmospheric surface layer, J. Atmos. Sci., 28, 190–201, 1971.

Paper 5
Wind-induced response of an offshore wind turbine under non-neutral conditions: A comparison with Hywind Scotland

*Rieska Mawarni Putri[1] and Charlotte Obhrai[1]
[1]Department of Mechanical and Structural Engineering and Materials Science, University of Stavanger, Norway

Wind-induced response of an offshore wind turbine under non-neutral conditions: A comparison with Hywind Scotland

Rieska Mawarni Putri and Charlotte Obhrai

Department of Mechanical and Structural Engineering and Materials Science, University of Stavanger, Norway

E-mail: rieska.m.putri@uis.no

Abstract. In this study, aeroelastic simulations of a 5 MW spar wind turbine are performed by using simulated wind fields that are representative of surface layer marine atmospheric turbulence under different atmospheric stratifications. The spar floater's motion responses from the simulations are then compared with the observations from Hywind Scotland's 6 MW spar wind turbine. The platform's pitch and yaw motions from the simulations are consistent with the observations, in terms of mean wind speed and atmospheric stratification. The simulations and the observations show that a stable atmosphere induces the lowest platform pitch and yaw motions compared to neutral and unstable stratifications. Nonetheless, the discrepancy of platform motions between stable and unstable conditions is more pronounced from the observations than in the simulations. Uncertainties associated with the estimation of the atmospheric stability and the modelling of the turbulence's co-coherence for lateral separation may partly account for the discrepancies between the observed and the simulated motion responses of the spar wind turbine.

1. Introduction

In 2020, Jacobsen and Godvik [1] documented the spar floater motions from the first commercial floating wind farm, the Hywind Scotland, as a function of atmospheric stability. Hywind Scotland Wind Farm consists of five 6 MW spar wind turbines, which are located approximately 25 km from the coast of Peterhead, Scotland [1]. Due to its location, the wind farm is located in the marine atmospheric boundary layer (MABL), which is known for its variable atmospheric stability conditions throughout a year [2]. The study by Jacobsen and Godvik [1] clearly shows that atmospheric stability affects the spar wind turbines' floater motion responses in both free wind and wake conditions. The most significant effect was observed for the platform yaw motion of the spar floater under a stable atmosphere.

The influence of surface layer atmospheric stability on offshore wind turbine (OWT) load responses has been previously studied by e.g. Sathe et al. [3] and Holtslag et al. [4]. In Sathe et al. [3], the wind-induced response of a bottom-fixed wind turbine was found to depend on the atmospheric stability. In their study, the uniform shear turbulence model (Mann model) [5] which is outlined in the IEC 61400-1 [6], was used. Additionally, site-specific measurements were fitted to the uniform shear model for different atmospheric stability conditions. However, the uniform shear model was originally intended to be used only for neutral surface layer atmospheric stratification. Therefore, it cannot fully capture the effects of buoyancy-generated turbulence in non-neutral stratifications ([5, 7]).

There exist only a few turbulence models developed specifically for non-neutral atmospheric stability conditions, including the modified spectral tensor model [7], the Højstrup spectral model [8], and the Pointed-Blunt model [9]. The modified spectral tensor model was shown to work reasonably well for surface layer stable atmosphere, but not for unstable conditions, especially at low wave frequencies [7]. Whereas, the Højstrup spectral model was developed only for unstable stratification and its effect on floating wind turbine (FWT) load and motion responses has been studied previously by Putri et al. [10]. The Pointed-Blunt model was established based on measurements from an offshore observation platform, FINO1, at fixed elevations of 40, 60, and 80 m for various atmospheric stratifications [9]. The Pointed-Blunt model is representative of MABL, but it is limited in terms of height, particularly for heights higher than 80 m.

Using the Pointed-Blunt model, the present paper simulates the floater motion responses of a spar wind turbine exposed to wind flows under varying atmospheric stratifications (i.e. stable, neutral, and unstable). The simulated responses are compared to the observed responses from Hywind Scotland to determine if the Pointed-Blunt spectral model is able to represent the non-neutral conditions in the MABL.

2. Methodology

The wind fields for different surface layer atmospheric stratifications used in this study were generated following Cheynet [11] for the Pointed-Blunt model. Then, aero-hydro-servo-elastic simulations were performed on the 5 MW OC3 spar wind turbine [12] using these wind fields. Although an OWT may be partly located above the surface layer, the Pointed-Blunt model was used herein for simplicity.

2.1. Observations from Hywind Scotland

Hywind Scotland Wind Farm comprises five wind turbines (WTs) arranged in two rows with a distance of nine rotor diameters between neighbouring WTs [1]. Only observations from the WT exposed to free wind flow are discussed in the present study to focus on the influence of atmospheric stability on the spar WT responses.

Some key properties of the Hywind Scotland's WT are given in Table 3. In Jacobsen and Godvik [1], the observed floater motions (roll, pitch, and yaw) were studied using 10 min time series from December 2017 to July 2018. Their dataset excluded observations when the wind speed at the hub height was less than $3\,\mathrm{m\,s^{-1}}$, when there was limited power production, and when the nacelle yaw was larger than 5°. Due to the limited instrumentation at the Hywind Scotland site, the atmospheric stability was determined by measuring the temperature difference between the air and the sea ($\Delta T = T_{air} - T_{sea}$) [1]. The atmosphere's stability was flagged as unstable when $\Delta T < -1.5°C$, neutral if $-1.5°C < \Delta T < 0.5°C$, and stable for $\Delta T > 0.5°C$.

2.2. Step 1: Wind field generation

The thermal stratification of the atmosphere is quantified by the non-dimensional stability parameter $\zeta = z/L$, where z is a reference height [m] and L is the Obukhov length [m], in the present study. L is proportional to the ratio between the cube of the friction velocity (u_*^3) and the virtual potential temperature flux [13]. An unstable atmosphere occurs when the turbulence is enhanced by buoyancy, while a stable atmosphere occurs when the turbulence is inhibited by buoyancy. In the present study, five stability classes are considered, ranging from $\zeta = -0.5$ to $\zeta = 0.5$ as given in Table 1. Wind field generation was performed using MATLAB [11], which requires three inputs: the mean wind speed, the one-point spectrum, and the co-coherence of turbulence, which is the real part of the root-coherence [14]. The wind time series were generated using the spectral representation method ([15, 16]). For each stability class, eight mean wind speeds ($\overline{u}_{hub}$) were considered (Table 2), so there are 40 cases in total. Each case was generated as a 30 min wind time series with a sampling rate of 9.1 Hz. To help reduce uncertainty, each

Table 1. Atmospheric stability classification.

Stability	ζ
Moderately unstable	$-0.5 \leq \zeta < -0.3$
Slightly unstable	$-0.3 \leq \zeta < -0.1$
Near-neutral	$-0.1 \leq \zeta < 0.1$
Slightly stable	$0.1 \leq \zeta < 0.3$
Moderately stable	$0.3 \leq \zeta < 05$

case was simulated using six different random seeds, where the median values were chosen as the averaging method.

The empirical formula for the Pointed-Blunt spectral model, which is valid for near-neutral and unstable stratifications [9]:

$$\frac{fS_i}{u_*^2} = \frac{a_1^i n}{(1 + b_1^i n)^{5/3}} + \frac{a_2^i n}{1 + b_2^i n^{5/3}} \tag{1}$$

for a stable atmosphere, the following applies [9]:

$$\frac{fS_i}{u_*^2} \approx c_1 n^{-2/3} + \frac{a_2^i n}{1 + b_2^i n^{5/3}} + a_3 n^{-2}. \tag{2}$$

where S_i, $i = u, v, w$ is the one-point spectrum of turbulence component. Coefficients a_1^i, a_2^i, a_3, b_1^i, b_2^i, and c_1 are a function of stability and for brevity, the values are not provided here, but are available in Cheynet et al. [9]. f is the frequency [Hz], $n = fz/\overline{u}_{hub}$ is the dimensionless frequency, and u_* is the friction velocity [$\mathrm{m\,s^{-1}}$].

The friction velocity is estimated following Section 2.3.6 in DNV-RP-C205 [17]:

$$\overline{u}_{hub} = \frac{u_*}{\kappa}\left(\ln\frac{z}{z_0} - \psi\right) \tag{3}$$

where $\overline{u}_{hub}$ is the mean wind speed at a reference height, in this case at the hub elevation. $\kappa \approx 0.4$ is the von Kármán constant, z_0 is the surface roughness, and ψ is a stability function [17]:

$$\psi = \begin{cases} -4.8\zeta & \zeta \geq 0 \\ 2\ln(1+x) + \ln(1+x^2) - 2\tan^{-1}(x) & \zeta < 0 \end{cases} \tag{4}$$

where $x = (1 - 19.3\zeta)^{1/4}$. The surface roughness z_0, is computed using the Charnock relation by assuming near-neutral stability for simplicity [18]:

$$z_0 = \frac{\alpha_c u_*^2}{g} \tag{5}$$

α_c is a constant, taken as 0.0185 [19] and $g = 9.81\,\mathrm{m\,s^{-1}}$ is the acceleration of gravity. Fig. 1 summarises the estimated friction velocity for each stability class and mean wind speed. The friction velocity increases almost linearly with the mean wind speed and as ζ decreases, as expected.

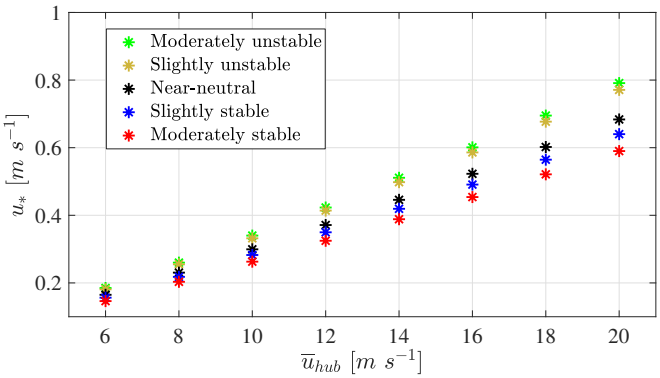

Figure 1. Estimated friction velocity for the considered atmospheric stability classes, as a function of mean wind speed at hub height.

The stability-dependant co-coherence was taken from the empirical formula [9], which was developed based on the Davenport coherence function [20]. The formulation is applicable only for vertical separations. In the absence of information on the lateral-separation co-coherence, it was then assumed that the lateral-separation co-coherence has the same magnitude as the vertical-separation co-coherence, that is

$$\gamma_i(d,f) \approx \exp\left\{-\left[\frac{d}{\overline{u}_{hub}}\sqrt{(c_1^i f)^2 + (c_1^i)^2}\right]\right\} \tag{6}$$

where d is the separation distance [m] either in the lateral or vertical direction, c_1^i and c_2^i are stability-dependant coefficients.

The dimensionless target spectra of the Pointed-Blunt model at near-hub height for $\overline{u}_{hub} = 12\,\mathrm{m\,s^{-1}}$ are presented in Fig. 2. The spectra are normalised with the dissipation of turbulence kinetic energy [13]:

$$\phi_\epsilon^{2/3} = \begin{cases} 1 + 0.5|\zeta|^{2/3}, & \zeta \le 0 \\ (1 + 5\zeta)^{2/3}, & \zeta \ge 0 \end{cases} \tag{7}$$

For comparison, the well-known empirical spectra for near-neutral stratification from Kansas measurement (Kaimal spectral model) [13] are shown as dashed lines. The atmospheric stability affects the turbulent component spectra, especially when $n < 0.4$. At this range, the spectral energies are higher under unstable conditions than under stable conditions, for all three velocity components.

Similarly, the stability-dependent co-coherence is plotted in Fig. 3 and was compared with the IEC exponential coherence [6]. Here, the separation distance d is taken as 60 m, which is applicable for either lateral or vertical separation, and $\overline{u}_{hub} = 12\,\mathrm{m\,s^{-1}}$. The magnitude of the co-coherences increases gradually from moderately stable to moderately unstable conditions, which is not included in the exponential coherence model [6]. The IEC exponential coherence provides significantly lower co-coherences for the cross-wind component at $kd < 0.2$ and vertical wind component for all kd, due to (1) the lower magnitudes of turbulence length scale for the v-component (113 m) and w-component (28 m) than the u-component (340 m) and (2) a constant decay coefficient of 12 for all three velocity components.

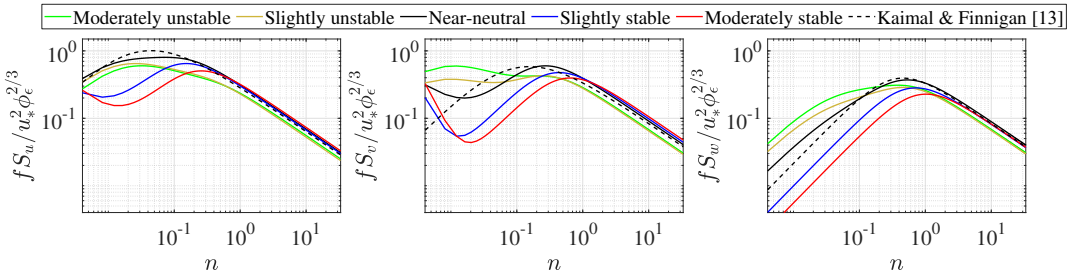

Figure 2. Empirical spectra of the along-wind (left), cross-wind (middle), and vertical (right) velocity components for all considered stability classes for $\overline{u}_{hub} = 12\,\mathrm{m\,s^{-1}}$. The velocity spectrum from Kaimal and Finnigan [13] for near-neutral stability is presented in dashed line as a benchmark.

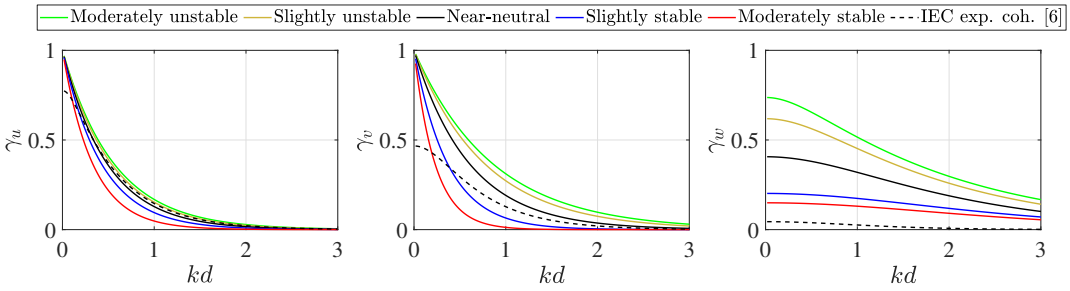

Figure 3. Theoretical co-coherence of the along-wind (left), cross-wind (middle), and vertical (right) velocity components for all considered stability classes for $\overline{u}_{hub} = 12\,\mathrm{m\,s^{-1}}$ and separation distance of $d = 60\,\mathrm{m}$. $k = 2\pi f/\overline{u}_{hub}$ is the wave number. The exponential coherence from IEC 61400-1 [6] for near-neutral stability is presented in the dashed line for comparison.

Table 2. Waves parameters for different mean wind speeds.

	Mean wind speed at hub height [$\mathrm{m\,s^{-1}}$]							
	6	8	10	12	14	16	18	20
H_s [m]	0.5	0.6	0.7	1.1	1.8	2.6	3.5	3.8
T_p [s]	3.5	3.9	3.7	5.2	6.8	8.0	6.5	9.7

2.3. Step 2: Aero-hydro-servo-elastic simulation

SIMA (Simulation Workbench for Marine Application) [21] is used as the aero-hydro-servo-elastic simulation tool. The main environmental loads for the aeroelastic simulations are turbulent wind and waves. The turbulent wind input is as described previously and the wave input is given in Table 2, where reference values were taken from Jacobsen and Godvik [1]. The same wave input is applied for all stability classes for each mean wind speed. Each case is run for 30 min, to match the duration of the wind time series.

The spar wind turbine is modelled following Jonkman [12] for the Phase IV of Offshore

Table 3. Spar wind turbines' key characteristics.

Parameter [unit]	Hywind Scotland	OC3
Rated power [MW]	6	5
Rotor diameter [m]	154	126
Hub height [m above sea level]	98	90
Rated wind speed [$\mathrm{m\,s^{-1}}$]	10	11.4
Water depth [m]	95-120	320
Floater draft [m]	78	120
Mooring [-]	3 lines with crowfoot	3 lines

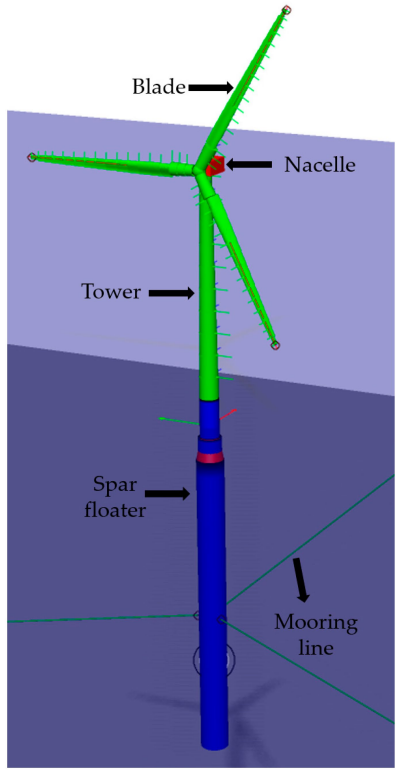

Figure 4. OC3 spar wind turbine modelled in SIMA.

Code Comparison Collaboration (OC3) project, which adopts the NREL's 5 MW turbine. Some important characteristics of the spar WT are provided in Table 3, side-by-side with the Hywind Scotland's spar WT properties as a comparison. Fig. 4 illustrates the OC3 spar WT model in SIMA. The Hywind Scotland WTs have a similar configuration but with a different blade-pitch controller and mooring system, and slightly different dimensions.

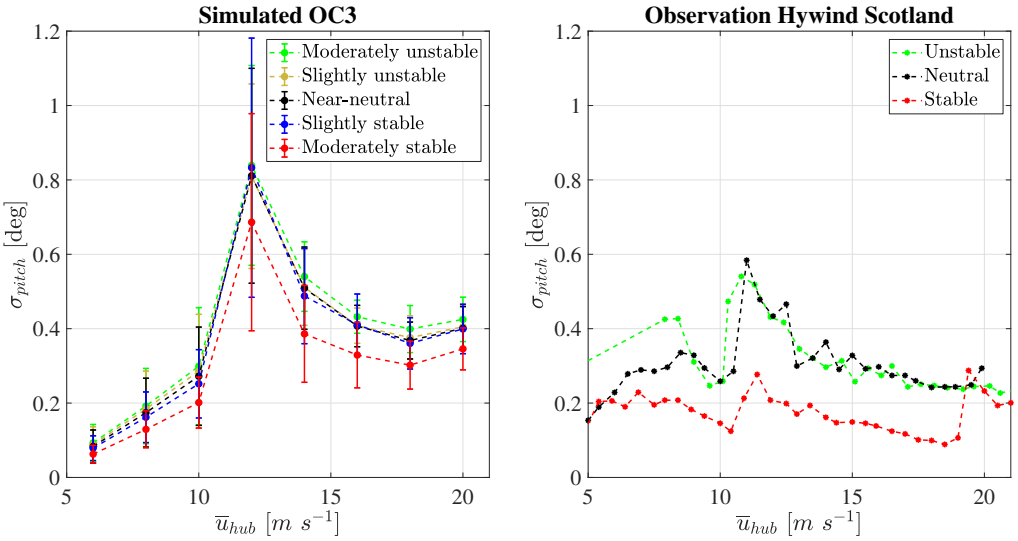

Figure 5. Platform pitch motion: simulation (left) vs observation (right). In the left panel, the circles are the median values from the six seeds, and the error bars indicate the minimum and maximum values from the six seeds.

3. Results and discussion

3.1. Floater motions

We focus herein on the pitch and yaw motions of the floater, which were particularly sensitive to the atmospheric stratification according to the Hywind Scotland observations [1]. The simulated platform pitch and yaw motions are given in the form of standard deviation from a 10 min time series response. Although the simulations were performed for a 30 min duration, only the last 10 min time series were analysed for two main purposes: (1) to avoid the initial transient period and (2) to use a similar averaging time to the one used by Jacobsen and Godvik [1] for Hywind Scotland.

Fig. 5 compares the simulated and the observed platform pitch standard deviations plotted against the mean wind speed for all considered stability classes. In the simulated results, the median values from the six seeds are shown in circles, where the error bars mark the minimum and maximum values from the six seeds at each mean wind speed. The Hywind Scotland observations are presented as the mean values (right panel of Fig. 5) at each mean wind speed bin with an increment of 0.5 m s^{-1}.

Overall, there is a good agreement between the simulations and the observations in Fig. 5. Yet, the magnitude of the platform pitch from the simulations at wind speeds lower than rated are higher than the observations, since there is an advanced blade-pitch controller applied in the Hywind Scotland WTs, while the OC3 model uses only a conventional controller [12]. The advanced blade-pitch controller [22] damps the excessive platform pitch motion of the full-scale spar WTs at Hywind Scotland for wind speeds rated and above. Both the simulated and the observed platform pitch increase with mean wind speed up to the rated wind speed (see Table 3), and then decrease gradually. When using a standard pitch controller for bottom fixed wind turbines for a floating wind turbine, the pitch frequency of the spar floater is nearly similar to the blade pitch frequency of the controller above rated wind speeds. This may account for the differences observed here. Additionally, the use of co-coherence in Eq. 6 may also contribute to

these differences, as the dependency of the decay coefficients on the ratio of vertical separation distance-to-height d_z/z in the MABL [23] is not included. According to Cheynet [23], the use of the Davenport coherence model [20] may lead to overestimation in the simulated wind turbine responses.

Concerning the atmospheric stratification, both the simulations and the observations show that stable conditions yield the lowest platform pitch response of a spar WT, compared to neutral and unstable conditions (Fig. 5). The simulated platform pitch increases from moderately stable to near-neutral and to moderately unstable conditions. Neutral and unstable conditions yield approximately similar magnitudes of platform pitch, both in the simulated and observed responses. Even so, from the simulation, the platform pitch motion under moderately unstable condition is slightly superior to the near-neutral condition for all wind speeds. The observations show that the platform pitch motion under unstable condition is slightly higher than for neutral condition, only at wind speeds lower than the rated.

Similarly, Fig. 6 shows the simulated and the observed platform yaw standard deviations plotted against the mean wind speed for all considered stability classes. In general, there is a similar trend for the platform yaw responses for both the simulations and the observations. The platforms yaw in greater magnitude with wind speed increment, as a higher wind speed induces a higher yaw moment on the rotor. Except for stable stratification, the observation shows mainly higher platform yaw response than the simulation. One of the causes may be due to the larger rotor size of the Hywind Scotland WT than the OC3 model which contributes to a larger yaw moment experienced by the platform. Also, the Hywind Scotland observations considered only periods when the active yaw damping control was disabled [1].

The simulated and the observed platform yaw motions show a similar dependency on the atmospheric stratification as shown in Fig. 6. The simulated platform yaw increases consistently from moderately stable to near-neutral and to moderately unstable conditions. The same is also noted from the Hywind Scotland observation, except that the platform yaw responses under neutral and unstable conditions are roughly of the same magnitude.

3.2. Discussion

Albeit there is a reasonable agreement between the simulated and the observed platform responses, a notable discrepancy in magnitude is especially seen when comparing stable and unstable conditions. The simulations show a systematic change of the platform responses with the atmospheric stability, as it shifts from moderately stable to moderately unstable. This behaviour follows the trend of the target turbulent wind spectra, particularly at dimensionless frequencies below 0.05 shown in Fig. 2. The natural frequencies of large floating wind turbines are typically below 0.2 Hz, which coincide with the observed higher spectral energy of the velocity components in unstable atmospheric conditions. On the other hand, there are larger discrepancies of platform motion responses for stable and unstable conditions from the Hywind Scotland observations. The estimation of atmospheric stability at the Hywind Scotland site was in fact quite crude due to the limited observation available i.e. by measuring the temperature difference between the air and the sea. This method is most likely unable to resolve atmospheric stability with a fine resolution. Even so, the observed full-scale measurements show a clear difference of platform motion responses between unstable and stable conditions that were successfully reproduced in the simulations. There is no rule as to which one is the best method to categorise atmospheric stability. Nonetheless, it is recommended to consider both the temperature and momentum fluxes to determine the degree of atmospheric stratification [13]. As a result, there is an implied uncertainty on how stable is actually 'stable stability class', and how unstable is actually 'unstable stability class' in the Hywind Scotland study.

The influence of co-coherence on the floater yaw response between the simulations and the observations at Hywind Scotland can not be fully resolved, since to the authors' knowledge, there

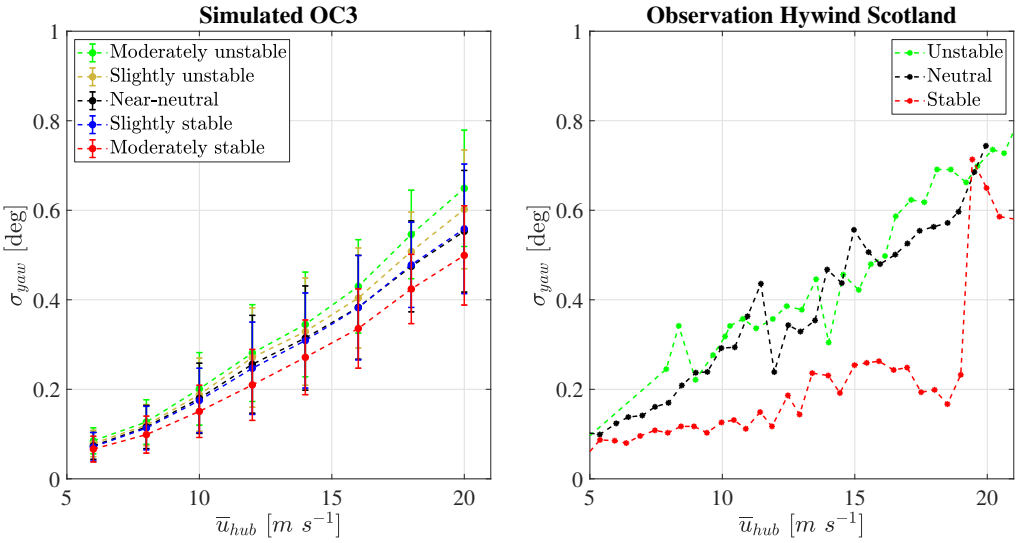

Figure 6. Platform yaw motion: simulation (left) vs observation (right). Simulation: the circles are the median values from the six seeds, and the error bars indicate the minimum and maximum values from the six seeds. Observation: the stars mark the mean values at each mean wind speed bin.

exist only limited studies that focus on the coherence for lateral separations at MABL, e.g. by Kristensen and Jensen [25]. The recent COTUR study [24] has attempted to measure co-coherence for lateral separation at different heights at MABL but has not been classified as a function of atmospheric stability. The floater yaw response of a spar WT has been shown to be susceptible to the spatial variation of turbulent wind, particularly in the lateral direction [26], where a lower magnitude of lateral-separation co-coherence may cause a higher platform yaw response. In the simulation, the target lateral-separation co-coherences are applied similarly to the vertical-separation co-coherences due to the absence of information on the lateral-separation co-coherence from FINO1 measurement. As highlighted by Solari and Piccardo [27] also Saranyasoontorn et al. [28], the behaviour of lateral-separation co-coherence differs from vertical-separation co-coherence for each velocity component. It is unclear whether the assumption of using the same values for lateral-separation and vertical-separation co-coherences is reasonable for floating WT's aeroelastic simulations. Assuming identical co-coherence decays for lateral and vertical separations is likely an oversimplification, which is partly reflected by the discrepancies between the simulated and the measured spar floater responses. Therefore, additional measurements of the co-coherence for lateral separations are needed in the MABL, to properly model the turbulent wind loading on the rotor of state-of-the-art OWTs.

4. Conclusion

This study compared the responses of a simulated spar wind turbine (WT) exposed to synthetic wind fields generated based on real measurements in the marine atmospheric boundary layer (MABL), and the actual observations of spar WT responses at Hywind Scotland Wind Farm. Although the simulated spar WT differs in terms of size, control system, and mooring system from the Hywind Scotland WT, we aim to focus on the comparison of the platform pitch and yaw motions with respect to various atmospheric stratifications. Five stability classes are defined in

the simulations, based on the non-dimensional stability parameter $\zeta = z/L$, while three stability classes are identified from the observation as measured by the temperature difference between the air and sea.

Aeroelastic simulations using the Pointed-Blunt spectral wind model were able to reproduce similar variations and trends in the platform pitch and yaw motion responses of a 5 MW spar WT as a function of atmospheric stability when compared to the full-scale observations of Hywind Scotland spar WT. Both the simulated and the observed responses show that a spar-type WT experiences larger platform pitch and yaw motions in unstable atmospheres. This demonstrates the importance of including atmospheric stratification in the fatigue design of large floating offshore WTs since the occurrence of non-neutral atmospheres is prominent at MABL.

The simulations show a systematic decrease in platform pitch and yaw magnitudes when the atmospheric stability moves from moderately unstable to moderately stable, as also noted from the Hywind Scotland observations. However, some discrepancies were found between the observed and the simulated motion responses for unstable and stable conditions. The different methods used to classify atmospheric stratification at the Hywind Scotland Wind Farm and in the simulations may partly explain this discrepancy. Additionally, the implementation of identical co-coherences for lateral and vertical separations may, to some extent, contribute to the noted discrepancy.

The platform pitch motion increases with the mean wind speed up to the rated speed and then decreases due to the negative damping effect, which was seen both in the simulation results and the observations. The observation suggests a smaller negative damping response than the simulation, because of the implementation of an advanced blade-pitch controller. Also, the simulations adopted a co-coherence model where the decay coefficients are independent on the measurement height or the separation distance, which may result in a larger negative damping effect due to an overestimation of the wind loading. Therefore, aeroelastic simulations of offshore wind turbines (OWTs) require accurate co-coherence modelling to properly estimate the wind loading, as emphasised in the present study.

References

[1] Jacobsen A and Godvik M Influence of wakes and atmospheric stability on the floater responses of the Hywind Scotland wind turbines 2021 *Wind Energy* **24(2)** 149–161
[2] Lee J A, Hacker J P, Delle Monache L, Kosović B, Clifton A, Vandenberghe F, and Rodrigo, J S Improving wind predictions in the marine atmospheric boundary layer through parameter estimation in a single-column model 2017 *Mon. Weather Rev.* **145(1)** 5–24
[3] Sathe A, Mann J, Barlas T, Bierbooms W A A M, and Van Bussel G J W Influence of atmospheric stability on wind turbine loads 2013 *Wind Energy* **16(7)** 1013–1032
[4] Holtslag M C, Bierbooms W A A M, and Van Bussel G J W Wind turbine fatigue loads as a function of atmospheric conditions offshore 2016 *Wind Energy* **19(10)** 1917–1932
[5] Mann J The spatial structure of neutral atmospheric surface-layer turbulence 1994 *J. fluid mech.* **273** 141–168
[6] IEC 61400-1 Wind Turbines Part 1: Design Requirements 2005
[7] Chougule A, Mann J, Kelly M, and Larsen, G C Simplification and validation of a spectral-tensor model for turbulence including atmospheric stability 2018 *Bound. Lay. Met* **167(3)** 371–397
[8] Højstrup J Velocity spectra in the unstable planetary boundary layer 1982 *J. of Atm. Sci.* **39(10)** 2239–2248
[9] Cheynet E, Jakobsen J B, and Reuder J Velocity spectra and coherence estimates in the marine atmospheric boundary layer 2018 *Bound. Lay. Met* **169(3)** 429–460
[10] Putri R M, Obhrai C, and Knight J M Offshore wind turbine loads and motions in unstable atmospheric conditions 2019 *J. Phys.: Conf. Ser.* **1356(1)** 012016
[11] Cheynet E Wind field simulation (the fast version) 2020 `https://zenodo.org/record/3774136`
[12] Jonkman J 2010 *Definition of the Floating System for Phase IV of OC3* (Golden: National Renewable Energy Lab.)
[13] Kaimal J C and Finnigan J J 1994 *Atmospheric boundary layer flows: their structure and measurement* (New York: Oxford University Press)
[14] Watson, B H H 1975 *A study of the statistical approach to wind loading* (Cape Town: University of Cape Town)

[15] Shinozuka M, and Jan, C M Digital simulation of random processes and its applications 1972 *J. sound and vibr.* **25(1)** 111–128
[16] Veers P S 1988 *Three-dimensional wind simulation* (Albuquerque: Sandia National Labs.)
[17] DNV RP-C205 Environmental conditions and environmental loads 2010
[18] Charnock H Wind stress on a water surface 1955 *Quar. J. of the Royal Met. Soc.* **81(350)** 639–640
[19] Wu J Wind-stress coefficients over sea surface near neutral conditions—A revisit 1980 *J. Phys. Oceanogr.* **10(5)** 727–740
[20] Davenport A G The Spectrum of Horizontal Gustiness near the Ground in High Winds 1961 *Q. J. R. Meteorol. Soc.* **87** 194–211
[21] SINTEF Simulation workbench for marine applications Accessed April 2022 `https://www.sintef.no/en/software/sima/`
[22] Skaare B Development of the Hywind Concept 2017 *Int. Conf. Offsh. Mech. and Arctic Eng.* **57779** V009T12A050
[23] Cheynet E Influence of the measurement height on the vertical coherence of natural wind 2019 *In Conf. the Italian Assoc. Wind Eng.* 207–221
[24] Cheynet E et al. The COTUR project: remote sensing of offshore turbulence for wind energy application 2021 *Atm. Measur. Techniq.* **14(9)** 6137–6157
[25] Kristensen, L and Jensen N O Lateral coherence in isotropic turbulence and in the natural wind 1979 *Bound. Lay. Met* **17(3)** 353—373
[26] Godvik M 2016 *Influence of wind coherence on the response of a floating wind turbine* In: Science Meets Industry
[27] Solari G and Piccardo G Probabilistic 3-D turbulence modeling for gust buffeting of structures 2001 *Prob. Eng. Mech.* **16(1)** 73–86
[28] Saranyasoontorn K, Manuel L, and Veers P S A comparison of standard coherence models for inflow turbulence with estimates from field measurements 2004 *J. Sol. Energy Eng.* **126(4)** 1069–1082

Bibliography

IEC, . Iec: Iec 61400-1: Wind turbines part 1 – design requirements. 2005.

United Nations, . Paris agreement. https://unfccc.int/sites/default/files/english_paris_agreement.pdf; 2015. Online; accessed 26-June-2022.

IRENA, . Renewable energy statistics. Tech. Rep.; 2021.

IEA, . Global energy review 2020. https://iea.blob.core.windows.net/assets/7e802f6a-0b30-4714-abb1-46f21a7a9530/Global_Energy_Review_2020.pdf; 2020. Online; accessed 30-June-2022.

IEA, . Wind electricity. https://www.iea.org/reports/wind-electricity; 2022. This work is licenced under the Creative Commons Attribution 4.0 International License. To view a copy of this licence, visit http://creativecommons.org/licenses/by/4.0/.

Jaganmohan, M.. Installed wind power capacity worldwide 2001-2021. https://www.statista.com/statistics/268363/installed-wind-power-capacity-worldwide/; 2022. Online; accessed 04-April-2022.

Fleming, S.. Wind farms now provide 14% of eu power – these countries are leading the way. https://www.weforum.org/agenda/2019/03/wind-farms-now-provide-14-of-eu-power-these/-countries-are-leading-the-way/; 2019. Online; published 06-March-2019.

Brunel, . The pros and cons of onshore & offshore wind. https://www.brunel.net/en/blog/renewable-energy/onshore-offshore-wind; 2021. Online; published 19-May-2021.

European Comission, . Offshore renewable energy. https://energy.ec.europa.eu/topics/renewable-energy/offshore-renewable-energy_en; 2022. Online; accessed 21-February-2023.

Europe, W.. Wind energy in europe: 2021 statistics and the outlook for 2022-2026. Tech. Rep.; Wind Europe; 2022. Published February 2022.

regjeringen.no, . Offshore renewable energy. https://www.regjeringen.no/en/aktuelt/ambitious-offshore-wind-power-initiative/id2912297/; 2022. Press release; published 11-May-2022.

EIA, . Levelized costs of new generation resources in the annual energy outlook 2022. https://www.eia.gov/outlooks/aeo/pdf/electricity_generation.pdf; 2022. Online; published March-2022.

Veers, P., Dykes, K., Lantz, E., Barth, S., Bottasso, C.L., Carlson, O., et al. Grand challenges in the science of wind energy. Science 2019;366(6464).

DONG Energy, . Burbo Bank Extension Offshore Wind Farm, Environmental Statement Volume 1 - Chapter 6: Project Description. Tech. Rep.; DONG Energy; 2013.

GE Renewable Energy, . GE Renewable Energy launches the uprated Haliade-X 13 MW wind turbine for the UK's Dogger Bank Wind Farm. https://www.ge.com/news/press-releases/ge-renewable-energy-launches-uprated-haliade-x/-13-mw-wind-turbine-uk-dogger-bank; 2020. Online; accessed 14-February-2023.

Paulsen, B.T., Bredmose, H., Bingham, H.B., Schløer, S.. Steep wave loads from irregular waves on an offshore wind turbine foundation: computation and experiment. In: International Conference on Offshore

Mechanics and Arctic Engineering; vol. 55430. American Society of Mechanical Engineers; 2013, p. V009T12A028.

Li, H., Bachynski, E.E.. Experimental and numerical investigation of nonlinear diffraction wave loads on a semi-submersible wind turbine. Renewable Energy 2021;171:709–727.

Bachynski, E.E., Eliassen, L.. The effects of coherent structures on the global response of floating offshore wind turbines. Wind Energy 2019;22(2):219–238.

Doubrawa, P., Churchfield, M.J., Godvik, M., Sirnivas, S.. Load response of a floating wind turbine to turbulent atmospheric flow. Applied Energy 2019;242:1588–1599.

Nybø, A., Nielsen, F.G., Reuder, J., Churchfield, M.J., Godvik, M.. Evaluation of different wind fields for the investigation of the dynamic response of offshore wind turbines. Wind Energy 2020;23(9):1810–1830.

Businger, J.A., Wyngaard, J.C., Izumi, Y., Bradley, E.F.. Flux-profile relationships in the atmospheric surface layer. Journal of the atmospheric Sciences 1971;28(2):181–189.

Kaimal, J.C., Wyngaard, J.C.J., Izumi, Y., Coté, O.R.. Spectral characteristics of surface-layer turbulence. Quarterly Journal of the Royal Meteorological Society 1972;98(417):563–589.

Davenport, A.G.. A statistical approach to the treatment of wind loading of tall masts and suspension bridges. PhD Dissertation, University of Bristle 1961a;.

Isyumov, N.. Alan g. davenport's mark on wind engineering. Journal of Wind Engineering and Industrial Aerodynamics 2012;104:12–24.

Putri, R.M., Obhrai, C., Jakobsen, J.B., Ong, M.C.. Numerical analysis of the effect of offshore turbulent wind inflow on the response of a spar wind turbine. Energies 2020a;13(10):2506.

Putri, R.M., Obhrai, C., Jakobsen, J.B.. Response sensitivity of a semisubmersible floating offshore wind turbine to different wind spectral models.

In: Journal of Physics: Conference Series; vol. 1618. IOP Publishing; 2020b, p. 022012.

Cheynet, E., Jakobsen, J.B., Reuder, J.. Velocity spectra and coherence estimates in the marine atmospheric boundary layer. Boundary-layer meteorology 2018;169(3):429–460.

Putri, R.M., Obhrai, C., Knight, J.. Offshore wind turbine loads and motions in unstable atmospheric conditions. In: Journal of Physics: Conference Series; vol. 1356. IOP Publishing; 2019, p. 012016.

Putri, R.M., Obhrai, C.. Wind-induced response of an offshore wind turbine under non-neutral conditions: A comparison with hywind scotland. In: Journal of Physics: Conference Series; vol. 2362. IOP Publishing; 2022, p. 012031.

Putri, R.M., Cheynet, E., Obhrai, C., Jakobsen, J.B.. Turbulence in a coastal environment: the case of vindeby. Wind Energy Science 2022;7(4):1693–1710.

Xu, K., Shao, Y., Gao, Z., Moan, T.. A study on fully nonlinear wave load effects on floating wind turbine. Journal of Fluids and Structures 2019;88:216–240.

Jonkman, J., Butterfield, S., Musial, W., Scott, G.. Definition of a 5-mw reference wind turbine for offshore system development. Tech. Rep.; National Renewable Energy Lab.(NREL), Golden, CO (United States); 2009.

Hall, M., Buckham, B., Crawford, C.. Evaluating the importance of mooring line model fidelity in floating offshore wind turbine simulations. Wind energy 2014;17(12):1835–1853.

Robertson, A., Jonkman, J., Masciola, M., Song, H., Goupee, A., Coulling, A., et al. Definition of the semisubmersible floating system for phase ii of oc4. Tech. Rep.; National Renewable Energy Lab.(NREL), Golden, CO (United States); 2014.

Stull, R.B.. An Introduction to Boundary Layer Meteorology. 1 ed.; Kluwer Academic Publishers; 1988.

Garratt, J.R.. The atmospheric boundary layer. Earth-Science Reviews 1994;37(1-2):89–134.

Kaimal, J.C., Finnigan, J.J.. Atmospheric Boundary Layer Flows: Their Structure and Measurement. Oxford University Press; 1994.

Zeng, X., Brunke, M.A., Zhou, M., Fairall, C., Bond, N.A., Lenschow, D.H.. Marine atmospheric boundary layer height over the eastern pacific: Data analysis and model evaluation. Journal of Climate 2004;17(21):4159–4170.

Ho, S.p., Peng, L., Anthes, R.A., Kuo, Y.H., Lin, H.C.. Marine boundary layer heights and their longitudinal, diurnal, and interseasonal variability in the southeastern pacific using cosmic, caliop, and radiosonde data. Journal of Climate 2015;28(7):2856–2872.

Tennekes, H., Lumley, J.L., Lumley, J.L., et al. A first course in turbulence. MIT press; 1972.

Holton, J.R.. An introduction to dynamic meteorology. American Journal of Physics 1973;41(5):752–754.

Wieringa, J.. Updating the davenport roughness classification. Journal of Wind Engineering and Industrial Aerodynamics 1992;41(1-3):357–368.

Charnock, H.. Wind stress on a water surface. Quarterly Journal of the Royal Meteorological Society 1955;81(350):639–640.

Wu, J.. Wind-stress coefficients over sea surface near neutral conditions—a revisit. Journal of Physical Oceanography 1980;10(5):727–740.

Smedman, A.S., Guo Larsén, X., Högström, U., Kahma, K.K., Pettersson, H.. Effect of sea state on the momentum exchange over the sea during neutral conditions. Journal of Geophysical Research: Oceans 2003;108(C11).

Monin, A.S., Obukhov, A.M.. Basic laws of turbulent mixing in the surface layer of the atmosphere. Contrib Geophys Inst Acad Sci USSR 1954;151(163):e187.

Högström, U.. Non-dimensional wind and temperature profiles in the atmospheric surface layer: A re-evaluation. In: Topics in Micrometeorology. A Festschrift for Arch Dyer. Springer; 1988, p. 55–78.

Businger, J.. A note on the businger-dyer profiles. In: Topics in Micrometeorology. A Festschrift for Arch Dyer. Springer; 1988, p. 145–151.

Thresher, R., Holley, W., Smith, C., Jafarey, N., Lin, S.. Modeling the response of wind turbines to atmospheric turbulence. Tech. Rep.; Oregon State Univ., Corvallis (USA). Dept. of Mechanical Engineering; 1981.

Mann, J.. The spatial structure of neutral atmospheric surface-layer turbulence. Journal of fluid mechanics 1994;273:141–168.

Cheynet, E.. Influence of the measurement height on the vertical coherence of natural wind. In: Conference of the Italian Association for Wind Engineering. Springer; 2018, p. 207–221.

Davenport, A.G.. The spectrum of horizontal gustiness near the ground in high winds. Quarterly Journal of the Royal Meteorological Society 1961b;87(372):194–211.

Haugen, D., Kaimal, J., Bradley, E.. An experimental study of reynolds stress and heat flux in the atmospheric surface layer. Quarterly Journal of the Royal Meteorological Society 1971;97(412):168–180.

Dobson, F.. Review of reference height for and averaging time of surface wind measurements at sea. World Meteorological Organization; 1981.

Kristensen, L., Jensen, N.. Lateral coherence in isotropic turbulence and in the natural wind. Boundary-Layer Meteorology 1979;17(3):353–373.

Neumann, T., Nolopp, K.. Three years operation of far offshore measurements at fino1. DEWI-Magazin 2007;.

Olesen, H., Larsen, S.E., Højstrup, J.. Modelling velocity spectra in the lower part of the planetary boundary layer. Boundary-Layer Meteorology 1984;29:285–312.

Högström, U., Hunt, J., Smedman, A.S.. Theory and measurements for turbulence spectra and variances in the atmospheric neutral surface layer. Boundary-Layer Meteorology 2002;103(1):101–124.

Drobinski, P., Carlotti, P., Newsom, R.K., Banta, R.M., Foster, R.C., Redelsperger, J.L.. The structure of the near-neutral atmospheric surface layer. Journal of the atmospheric sciences 2004;61(6):699–714.

Højstrup, J.. A simple model for the adjustment of velocity spectra in unstable conditions downstream of an abrupt change in roughness and heat flux. Boundary-Layer Meteorology 1981;21(3):341–356.

Peterson, E.W., Taylor, P.A., Højstrup, J., Otto Jensen, N., Kristensen, L., Petersen, E.L.. Risø 1978: Further investigations into the effects of local terrain irregularities on tower-measured wind profiles. Boundary-Layer Meteorology 1980;19:303–313.

Davenport, A.. The prediction of the response of structures to gusty wind. Safety of structures under dynamic loading 1977;1:257–284.

Smedman-Högström, A.S., Högström, U.. Spectral gap in surface-layer measurements. Journal of Atmospheric Sciences 1975;32(2):340–350.

Dyrbye, C., Hansen, S.O.. Wind loads on structures. 1997.

Sathe, A., Mann, J., Barlas, T., Bierbooms, W., van Bussel, G.. Influence of atmospheric stability on wind turbine loads. Wind Energy 2013;16(7):1013–1032.

Hansen, M.O.. Aerodynamics of wind turbines. Routledge; 2015.

Moriarty, P.J., Hansen, A.C.. Aerodyn theory manual. Tech. Rep.; National Renewable Energy Lab., Golden, CO (US); 2005.

Glauert, H.. Airplane propellers. Aerodynamic theory 1935;4:169–360.

Glauert, H.. A general theory of the autogyro. Tech. Rep.; Cranfield university; 1926. ARCR R&M No. 1111.

Pitt, D.M., Peters, D.A.. Theoretical prediction of dynamic-inflow derivatives. Vertica 1981;7(1).

Snel, H., Schepers, J.. Joint investigation of dynamic inflow effects and implementation of an engineering method. Tech. Rep.; Energy Research Centre of the Netherlands; 1995. ECN-C-94-107.

Bak, C., Madsen, H.A., Johansen, J.. Influence from blade-tower interaction on fatigue loads and dynamics (poster). In: 2001 European Wind Energy Conference and Exhibition (EWEC'01). WIP-Renewable Energies; 2001, p. 394–397.

Papi, F., Jonkman, J., Robertson, A., Bianchini, A.. Going beyond bem with bem: an insight into dynamic inflow effects on floating wind turbines. Wind Energy Science Discussions 2023;2023:1–29. URL: https://wes.copernicus.org/preprints/wes-2023-109/. doi:10.5194/wes-2023-109.

SINTEF, . Software: Sima. https://www.sintef.no/en/software/sima/; 2022. Online; accessed 08-June-2022.

Hasselmann, D.E., Dunckel, M., Ewing, J.. Directional wave spectra observed during jonswap 1973. Journal of physical oceanography 1980;10(8):1264–1280.

Jonkman, B.. Turbsim user's guide: Version 2.00. 00. National Renewable Energy Laboratory (NREL): Golden, CO, USA 2016;.

Larsen, T.J., Hansen, A.M.. How 2 HAWC2, the user's manual. Risø National Laboratory; 2019.

Cheynet, E.. Wind field simulation (the fast version). https://zenodo.org/record/3774136; 2020.

Jonkman, J.. Definition of the floating system for phase iv of oc3. Tech. Rep.; National Renewable Energy Lab.(NREL), Golden, CO (United States); 2010.

Krogsæter, O., Reuder, J.. Validation of boundary layer parameterization schemes in the weather research and forecasting (wrf) model under the aspect of offshore wind energy applications—part ii: boundary layer height and atmospheric stability. Wind Energy 2015;18(7):1291–1302.